Nucleation of Recrystallization studied by EBSP and 3DXRD

West, Stine

Publication date:
2009

Document Version
Publisher's PDF, also known as Version of record

UNIVERSITY OF COPENHAGEN
Risø DTU
National Laboratory
for Sustainable Energy
DTU

Risø-PhD-thesis

Nucleation of Recrystallization studied by EBSP and 3DXRD

Stine Stenfatt West

Risø-PhD-50(EN)

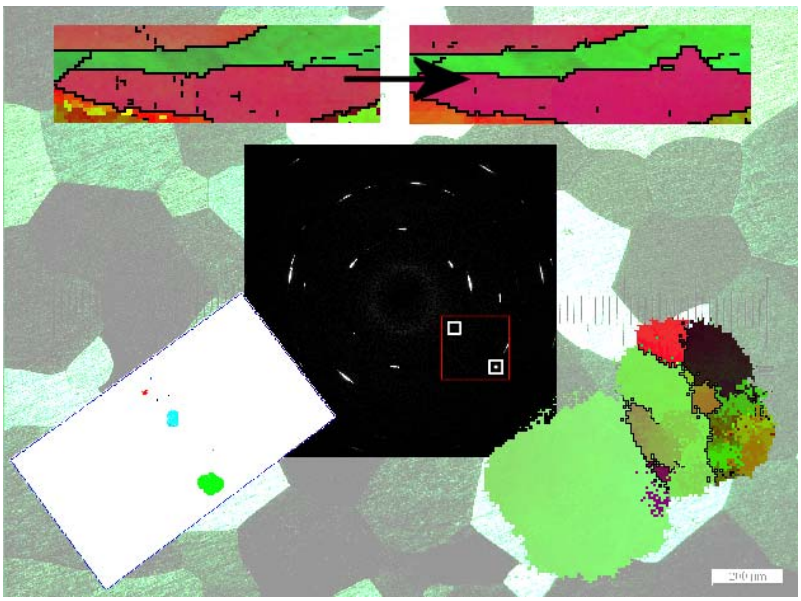

Risø National Laboratory for Sustainable Energy
Technical University of Denmark
Roskilde, Denmark
June 2009

DTU

Author: Stine Stenfatt West
Title: Nucleation of Recrystallization studied by EBSP and 3DXRD
Department: Materials Research Division

This thesis is submitted in partial fulfillment of the requirements for the Ph.D. degree at the University of Copenhagen

Risø-PhD-50(EN)
June 2009

Abstract:

When a deformed crystalline material is annealed, recrystallization will typically take place. In this process new perfect crystals nucleate and grow, consuming the deformation structure.
Traditionally, nucleation theories state that the crystal orientations of these new grains were already present in the deformed state, but several experiments have shown the emergence of what appears to be new orientations.
The purpose of the present project was to observe nucleation of recrystallization both on surfaces and in the bulk. Special focus was on the possible formation of nuclei with orientations not present in the deformed matrix before annealing.
To facilitate the nucleation studies, a well-annealed starting material was prepared from high-purity aluminum with a large average grain size and almost straight grain boundaries mostly forming triple junctions with angles close to 120°. The large grain size was necessary in order to ease determination of the nucleation sites and the analysis of orientation relationships between nuclei and parent grains.
A series of experiments was carried out using Electron Backscattered diffraction Patterns (EBSP). These were considered to provide a valuable background to support the results to be obtained by 3DXRD. Nuclei were observed both with parent orientations and new orientations not present before annealing. The rotation axes between the orientations of the nuclei and the orientations seen before annealing was correlated to the predicted deformation structure. A correlation was seen between this rotation axis and the normals to {111} slip planes of high activity, which were expected to form slip plane aligned dislocation boundaries. This axis is also the axis of misorientation associated with GNBs of twist character forming on {111} planes.
Experiments using the Three-Dimensional X-Ray Diffraction (3DXRD) microscope also successfully observed nucleation of recrystallization. The nuclei most easily found with the 3DXRD method are those with orientations different from the deformed structure and the method was thus ideal for this study. 6 nuclei of new orientations were found in the bulk of a sample after annealing. An orientation imaging map was reconstructed from the bulk of the sample before and after annealing. Such reconstructions have only been done before with completely recrystallized samples, so this was a unique opportunity to compare orientations observed locally in the bulk of a deformed sample before annealing with the orientations of the nuclei. The comparison was again based on the predicted deformation structure of the parent grains. The majority of the nuclei were seen to be rotated around the [100] axis, which was a possible misorientation axis associated with the predicted GNBs aligned with {010}.

ISBN 978-87-550-3760-1

Group's own reg. no.:
1605075-00

Sponsorship:
Danmarks Grundforskningsfond

Cover :
Background image: Optical micrograph of starting material.

Top: EBSP maps before and after nucleation of a parent oriented nucleus (C01). Touched up for illustrative purposes.

Middle: Background-corrected diffraction image taken after annealing showing diffraction spots from two nuclei.

Bottom left: Map of volumes of 6 bulk nuclei with new orientations projected along RD. From 3DXRD experiment.

Bottom right: Orientation imaging map of a layer in the partially-annealed sample. From 3DXRD experiment.

Pages:?
References:?

Information Service Department
Risø National Laboratory for Sustainable Energy
Technical University of Denmark
P.O.Box 49
DK-4000 Roskilde
Denmark
Telephone +45 46774004
bibl@risoe.dk
Fax +45 46774013
www.risoe.dtu.dk

Contents

1 Introduction **1**
- 1.1 General metallurgy . . . 2
  - 1.1.1 Recovery and recrystallization . . . 5
  - 1.1.2 Deformation theory . . . 5
- 1.2 Nucleation theories . . . 7
  - 1.2.1 Subgrain growth . . . 7
  - 1.2.2 SIBM . . . 8
  - 1.2.3 Twinning . . . 9
  - 1.2.4 Nucleation sites . . . 10
- 1.3 New orientations . . . 11
  - 1.3.1 Overview of theories . . . 11
- 1.4 Aim . . . 12

2 Experimental Techniques **15**
- 2.1 Optical microscopy . . . 16
- 2.2 EBSP . . . 16
- 2.3 3DXRD . . . 18
  - 2.3.1 Basic principles . . . 18
  - 2.3.2 Optics etc. . . . 20
  - 2.3.3 Detectors . . . 21
  - 2.3.4 Sample environment . . . 22
  - 2.3.5 Software . . . 24

3 Starting Material **27**
- 3.1 Rolling . . . 28
- 3.2 Furnaces . . . 29
- 3.3 Initial annealing treatments . . . 30
- 3.4 Deformation . . . 34
- 3.5 Annealing to nucleation . . . 36
- 3.6 Summary . . . 37

4 Nucleation Studied by EBSP **39**
4.1 Experimental . . . 39
4.1.1 Sample material and treatment . . . 39
4.1.2 EBSP characterization . . . 40
4.2 Results . . . 41
4.2.1 Parent oriented nuclei . . . 43
4.2.2 Nuclei with new orientations . . . 46
4.3 Slip plane analysis . . . 52
4.3.1 Possible rotation axes . . . 52
4.3.2 Dislocation boundary alignment . . . 53
4.3.3 Application to data . . . 55
4.4 Discussion . . . 55

5 3DXRD - The Experiment **59**
5.1 Experimental . . . 60
5.1.1 3DXRD setup . . . 60
5.1.2 3DXRD experimental procedure . . . 60
5.1.3 EBSP experimental procedure . . . 62
5.1.4 3DXRD feasibility study . . . 62
5.2 Near-field data . . . 64
5.3 Image processing . . . 64
5.4 Detection limit . . . 66
5.4.1 Diffraction background . . . 66
5.4.2 Experimental calculation of detection limit . . . 68
5.4.3 Discussion of detection limit . . . 69

6 3DXRD Experiment - Results **71**
6.1 Identification of nuclei . . . 71
6.1.1 Finding the undeformed crystallites . . . 72
6.1.2 Nuclei selection . . . 73
6.1.3 Nuclei volumes . . . 77
6.2 Descriptions of the gauge volume . . . 78
6.2.1 Orientation representations by {111} pole figures . . . 79
6.2.2 Orientation imaging maps . . . 83
6.3 Orientation comparison . . . 85
6.3.1 Slip plane analysis . . . 89
6.4 Discussion . . . 94

7 Conclusions **97**

8 Experimental outlook **99**

A EBSP maps **113**

B Preliminary 3DXRD Experiment **123**
B.1 3DXRD setup 124
B.2 Experimental procedure 124
B.2.1 Detection limit 125
B.2.2 Mapping before annealing 125
B.2.3 Annealing 126
B.2.4 Mapping after annealing 126
B.3 Results 127
B.3.1 Recrystallized grains 127
B.3.2 Orientations 127
B.3.3 EBSP maps 127
B.3.4 Volumes 130
B.3.5 Other nuclei 130
B.4 Experiences gained 130

C Authored publications **133**

Resumé

Når et deformeret krystallinsk materiale opvarmes vil der typisk finde rekrystallisation sted. Dette er en proces, hvor kimene til nye perfekte krystalkorn dannes og vokser.

Traditionalt siger teorierne for dannelsen af disse kim at deres krystalorientering allerede var til stede i det deformerede materiale, men adskillige eksperimenter har vist at der tilsyneladende også dannes nye orienteringer.

Formålet med dette projekt var at observere kimdannelsen af rekrystallisation både på overflader og indeni materialet. Fokus var især på muligheden for dannelse af kim med orienteringer, der ikke var til stede før opvarmningen.

Et udgangsmateriale blev forberedt af meget rent aluminium. Materialet havde en høj gennemsnitlig kornstørrelse og næsten lige korngrænser, der mødtes i triple-grænser med vinkler tæt på 120°. De store korn var nødvendige for lettere at kunne finde kimenes dannelses-steder og analysere orienteringsrelationerne mellem kim of forældrekorn.

En række eksperimenter blev gennemført med Electron Backscattered diffraction Patterns (EBSP). Der blev observeret kim både med orienteringer inden for spredningen af forældre-kornene og med nye orienteringer. Rotationsakserne mellem kimenes og forældrekornenes orientereinger blev korreleret med den forudsagte deformationsstruktur. Der blev fundet en sammenhæng mellem rotationsaksen og normalvektoren til {111}-slipplaner med høj aktivitet. Det var forudsagt, at der ville dannes dislokationsgrænser parallelt med disse planer. Normalen til disse planer var sammenfaldende med den tilhørende misorienteringsakse.

Vellykkede observationer af kimdannelse af rekrystallisation blev også opnået med Three-Dimensional X-Ray Diffraction (3DXRD)-mikroskopet. De kim, der nemmest observeres med 3DXRD-metoden har orienteringer forskellige fra den deformerede struktur, og metoden var derfor ideel til denne type studium. 6 kim med nye orienteringer blev fundet væk fra alle overflader i en prøve after opvarmning.

Et kort over orienteringerne som funktion af position blev rekonstrueret fra et tværsnit af prøven før og efter opvarmning. Denne type rekonstruktion har kun været foretaget med ikke-deformerede prøver tidligere, så dette var en enestående mulighed for at sammenligne de deformerede orienteringer med kimenes orienteringer. Sammenligningen blev igen udført baseret på den forudsagte deformationsstruktur i forældrekornene. Størstedelen af kimene var roteret om [100]-aksen, svarende til en mulig misorienteringsakse for de forudsagte dislokationsgrænser der fulgte {010}.

Preface

This thesis is submitted in partial fulfillment of the requirements for obtaining the Ph.D. degree at the University of Copenhagen in collaboration with Risø DTU, National Laboratory for Sustainable Energy. The project was carried out within the Center for Fundamental Research: Metal Structures in Four Dimensions (M4D) at Risø DTU. The supervisors were Robert Feidenhans'l at the University of Copenhagen and Dorte Juul Jensen, Grethe Winther, Henning Friis-Poulsen and Søren Schmidt at Risø DTU.

The study was conducted during the periods August 2004-December 2006 and August 2007-June 2009.

I would like to extend my thanks to a number of people; First of all to the technicians, Preben and Lars, for all their help in preparing samples and teaching me to use various equipment; Naoya Kamikawa for helping with EBSP maps for the 3DXRD feasibility study; Professor Brian Ralph for reading through this thesis and giving comments and suggestions; The Danish National Research Foundation for supporting M4D; ESRF for providing beamtime; Robert for making sure I handed in my half year reports and fulfilled all the other formal requirements; Dorte for always making me do my best; Grethe for all her help trying to help me understand the mysteries of slip; Henning for making the 3DXRD experiments run; Søren for mapping; all the people who spent long nights watching the experiments at ESRF; My office mate Ulrik and all the other M4D people for all the little things, and finally my husbond Mads for all his support throughout the years.

Chapter 1

Introduction and Background

Although metals have been used for thousands of years and it has been a well known fact that processing can change the properties of metals, only recent technological advances have allowed direct studies of the microstructure of materials. This has lead to a greater understanding of the mechanisms that for instance increase the strength of a metal when it is deformed by introducing dislocations into the perfect crystal lattice. Dislocations are imperfections in the crystal lattice, where the crystal planes do not match perfectly [1].

Many years of experience by trial and error has gained a large store of knowledge on the phenomenological behavior of metals. A better understanding of the microstructure and how it is formed will, however, allow for a more direct approach to obtaining materials with a specific set of desired properties.

Nucleation of recrystallization is a very important process in the formation of a microstructure of many metal products, as the orientations and positions of the nuclei play a major role in deciding the recrystallized microstructure. The frequency and sites of nucleation will determine the recrystallized grain size as well as the spread in grain sizes [2]. The orientations of nuclei will determine the recrystallized texture of the material. As many of the macroscopic properties depend on the microstructure, specific properties such as strength, ductility, resistance to fatigue or corrosion as well as formability can be cultivated by using deformation and heat treatments designed to give the desired pattern of nucleation [3].

Understanding the mechanisms governing nucleation forms a basis for realistic models to predict the behavior of metals during thermal processing. Where previous models have largely relied on assumptions about the position and orientation of nuclei, more data on the nature of nucleation is needed for more precise models.

To form a broad overview of the basic ideas of the field with an emphasis

on the theory needed for the present study, mostly textbook references have been used for this chapter with some key original references where it was deemed necessary. To mention all original references and go through all the details of the basic broad theory is outside the scope of this thesis. As nucleation with a focus on the formation of new orientations is the topic of this thesis, all relevant references within this topic will of course be considered where appropriate.

1.1 General metallurgy

This section will present a short introduction to the metallurgical background needed for the project.

Metallic atoms in pure metals or alloys will arrange themselves in a crystal lattice structure. The most common structures for metals are face-centered cubic (fcc), body-centered cubic (bcc) and close-packed hexagonal (cph) structures. Each structure has a unique pattern of repetition, and the smallest possible group of atoms which when repeated can recreate the crystal structure is called the unit cell [1].

The present work focuses on aluminum, which has an fcc lattice structure. The fcc lattice can be seen in figure 1.1.

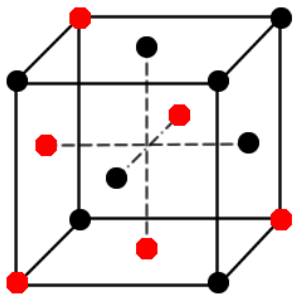

Figure 1.1: The fcc lattice. The atoms marked in red are part of the (111) crystal plane.

A crystal lattice may be considered to be intersected by different planes containing some of the atoms of the lattice [1]. Each crystal plane can be represented by three Miller indices h, k, l, where the plane is normal to the vector (h,k,l). As the crystal lattice repeats itself, there are actually many parallel hkl planes, which can be used for identifying the crystal orientation through Bragg diffraction (see chapter 2). An example of a crystal plane is

the (111) plane seen in figure 1.1. This is a close-packed plane and also has the smallest distance between subsequent planes.

The crystallographic orientation is often described using Euler angles (ϕ_1, Φ, ϕ_2), which define the three rotations necessary to transform the sample frame defined by rolling, normal and transverse directions (RD,ND,TD) (see section 3.1) into the crystallographic frame defined by the three crystallographic axes [001],[010] and [100] [4]. The rotation matrix defined by these angles is given as:

$$u = \begin{bmatrix} \cos\phi_1 \cos\phi_2 - \sin\phi_1 sin\phi_2 \cos\Phi & \sin\phi_1 \cos\phi_2 + \cos\phi_1 \sin\phi_2 \cos\Phi & \sin\phi_2 \sin\Phi \\ -\cos\phi_1 \sin\phi_2 - \sin\phi_1 \cos\phi_2 \cos\Phi & -\sin\phi_1 \sin\phi_2 + \cos\phi_1 \cos\phi_2 \cos\Phi & \cos\phi_2 \sin\Phi \\ \sin\phi_1 \sin\Phi & -\cos\phi_1 \sin\Phi & \cos\Phi \end{bmatrix}. \tag{1.1}$$

The transverse matrix $g = u^t$ which transforms the crystallographic system into the rolling system is also often used.

Metals and alloys will most commonly have a polycrystalline microstructure with grain sizes ranging from less than one to several thousands of micrometres. The individual grains may have atoms arranged in a perfect crystal lattice or contain internal misorientations depending on the processing history of the material. The misorientation between the crystal lattice in two points is defined as the smallest possible rotation (around an arbitrary axis) than will bring the two lattices to coincide. The original cast metal ingot will consist of almost strain-free crystal grains [3]. When such a metal is deformed, dislocations and other imperfections such as vacancies are introduced into the crystal structure. A dislocation is a defect in the crystal lattice in the form of an edge or screw dislocation [1]. The dislocations are shown in figure 1.2. These may occur individually or may be grouped as tilt, twist or mixed boundaries. While a perfect crystal may be deformed by introducing dislocations into the crystal lattice and allowing them to propagate, a crystal that already contains many dislocations will be more difficult to deform. This is due to the interactions between the dislocations, and thus the microstructure affects the macroscopic properties of the material. The dislocation density may be 10^6 times larger in a deformed material than in a well-annealed sample [5].

A large amount of internal strain in the form of dislocations means that energy is stored in the material. This energy can be released through annealing, where energy in the form of heat is introduced into the material allowing the further release of the stored energy in the processes of recovery and recrystallization. Figure 1.3 shows an entire process cycle from cast perfect crystals through deformation to recrystallization.

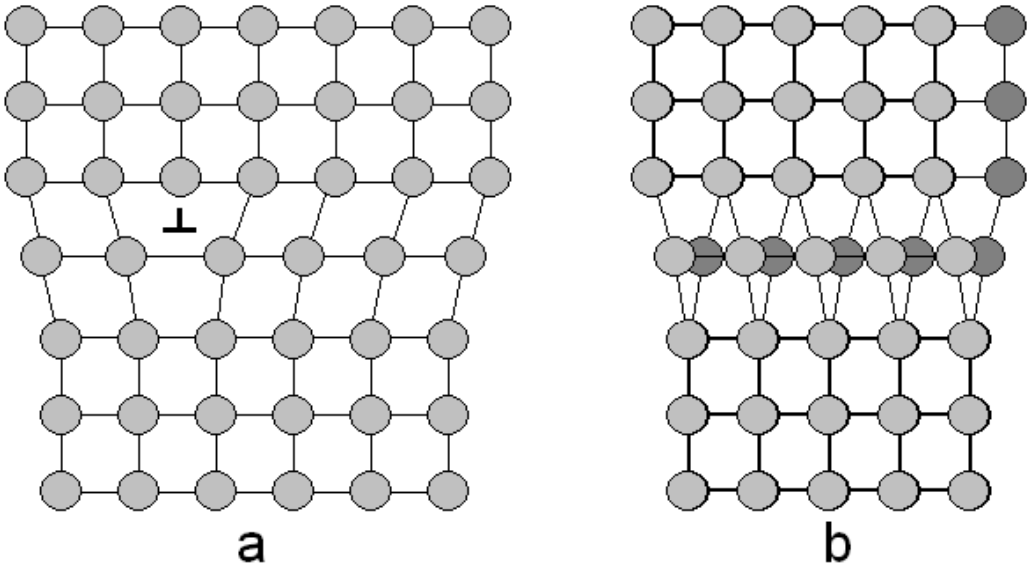

Figure 1.2: a) edge dislocation b) screw dislocation. The darker atoms are in a layer below the plane of the lighter atoms.

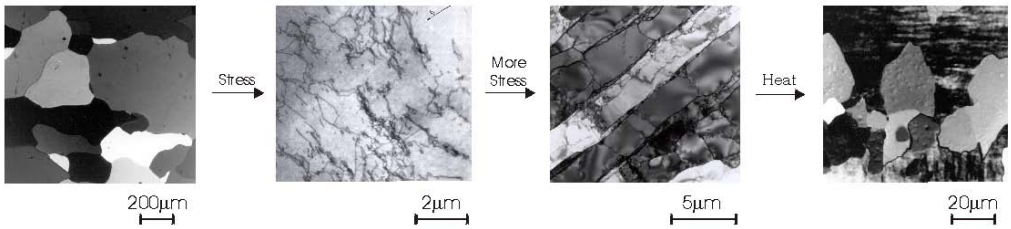

Figure 1.3: A typical process cycle.

1.1.1 Recovery and recrystallization

Recovery is a term covering the annealing processes happening before recrystallization. During recovery, some of the strain introduced into the crystal lattice is released, partially restoring the state prior to deformation. During this stage of the annealing, the grains will form subgrains of low internal misorientations, but no major orientation changes will take place [3, 6].

The annihilation of point defects such as vacancies will facilitate the movement of dislocations to allow them to group into boundaries between the subgrains.

Where recovery is considered to be a gradual process taking place everywhere in the material simultaneously, recrystallization is characterized by nucleation and growth of new strain-free grains in certain places in the material structure [3, 7]. These new grains eventually grow to consume the entire deformation structure. With further annealing, the much slower process of grain growth may cause some grains to consume others, increasing the average grain size.

1.1.2 Deformation theory

This section will introduce the slip mechanism, which facilitates the deformation of crystalline materials, as this is important for the understanding of some of the theories of new orientation formation mentioned later in this chapter (section 1.3).

In order to accommodate the macroscopic shape change taking place in a metal when it is deformed, the crystal lattice must reorganize. The two main methods of deformation in fcc metals are twinning (section 1.2.3) and slip [3].

Slip happens by entire crystal planes moving one lattice site at a time. The shear force required to make an entire crystal plane move simultaneously would have to overcome the theoretical shear strength of the material, which is much higher than what is seen in experiments [8]. Therefore, the motion of crystal planes must be explained by the slip of dislocations. This will usually happen on the most densely packed planes and in the most densely packed directions. E.g. for fcc crystals, the $\{111\}\langle 1\bar{1}0\rangle$ slip systems defined by the $\{111\}$ planes and the $\langle 1\bar{1}0\rangle$ directions is the most common slip system, although slip on other systems may also occur. Which of the set of planes and directions will be activated depends on the crystallographic orientation of the grain being deformed [9].

The force exerted on a crystal when it is loaded in compression or tension can be resolved into two components; the shear force F_s and the normal force

F_n [8]:

$$F_s = F\cos\phi \tag{1.2}$$
$$F_n = F\cos\psi \tag{1.3}$$
$$\phi + \psi = 90^\circ.$$

Here, ϕ is the minimum angle between the applied force and the slip plane, and ψ is the angle between the applied force and the slip plane normal. The shear stress is defined as [8]:

$$\tau = \frac{F_s}{A_{\text{shear}}} = \frac{F\cos\phi}{\frac{A}{\cos\psi}} = \frac{F}{A}\cos\phi\cos\psi = \sigma\cos\phi\cos\psi. \tag{1.4}$$

The proportionality factor of the shear stress $\cos\phi\cos\psi$ is called the Schmid factor [10]. The sum of ϕ and ψ will always be 90°, so it can be seen that the shear stress is at a maximum for a slip plane at 45° to the direction of loading.

A commonly used model for the deformation of polycrystalline samples is the Taylor model [11], which uses so-called full constraints. This means that it is assumed that all grains undergo the same overall shape change as the entire specimen. This results in slip on 5 independent slip systems. The model may qualitatively explain many features of the deformation texture, but many local deviations from this idealized model are also seen.

The deformed material consists of many cells separated by low-angle boundaries as well as high-angle boundaries. Cells are also sometimes referred to as subgrains [3], while Kuhlmann-Wilsdorf and Nielsen [12] define subgrains as cells which have such a high internal misorientation that different slip systems operate in different subgrains. The terms will be used interchangeably in the following, but specified where appropriate.

The separation between what is called low- and high-angle boundaries is normally 10-15° misorientation [13]. The spacing and angles of the boundaries depend on the processing history of the material. In a metal of high stacking fault energy such as aluminum that has been rolled to low or intermediate strains(defined as <50% reduction [9]), the deformed structure inside will typically consist of cells separated by two types of boundaries. The first type is extended planar dislocation boundaries, also called geometrically necessary boundaries (GNBs), as they accommodate different slip systems on each side of the boundary. GNBs will typically form long parallel cell blocks, and inside each cell block, the individuel cells will be separated by more randomly oriented boundaries termed incidental dislocation boundaries (IDBs) because they are formed by mutual trapping of glide dislocations [14].

During recovery, it is energetically favorable to increase the size of the cells to decrease the total area of low-angle grain boundaries. Generally, the larger cells will grow at the expense of the smaller cells, which are consumed. This coarsening of the cells may happen in different ways.

1.2 Nucleation theories

In order for a small volume of a single orientation to be a nucleus capable of growing into the surrounding deformed structure, it must exceed a certain size, called the critical embryo size [3]. Also, the nucleus must have a high-angle grain boundary to the deformed structure in order to drive the growth. An embryo is thus only called a nucleus when it starts to grow. Generally, the driving force for recrystallization, given by [3]:

$$P_d = \alpha \rho G b^2 \tag{1.5}$$

should be larger than the opposing force from the curvature of the boundary:

$$P_c = \frac{2\gamma_b}{R}. \tag{1.6}$$

Here, α is a constant, ρ is the dislocation density, G is the shear modulus, b is the Burgers vector of the dislocations, γ_b is the specific energy of the boundary and R is the radius of the nucleus. For realistic numbers, this means that the critical embryo size is of the order of $R = R_c = 1\mu$m [3]. This corresponds to billions of atoms and is thus not likely to arise from thermal fluctuations within the material [13].

Therefore, the most well-accepted nucleation theories state that the orientations seen in recrystallized nuclei must have been present in the deformed structure. The only exception to this is twinning (see section 1.2.3). There are several mechanisms for forming a nucleus from multiple subgrains smaller than the critical size. These will be described below.

1.2.1 Subgrain growth - coalescence and coarsening

As the following is based mainly on the text book by Humphreys and Hatherley [3], the term subgrain will be used as in the book, i.e. a distinction will not be made between cells and subgrains.

In subgrain coalescence, which happens by boundary migration, several low-angle grain boundaries may merge into a single grain boundary of higher angle [15, 16]. This is a continuous process, and generally larger subgrain

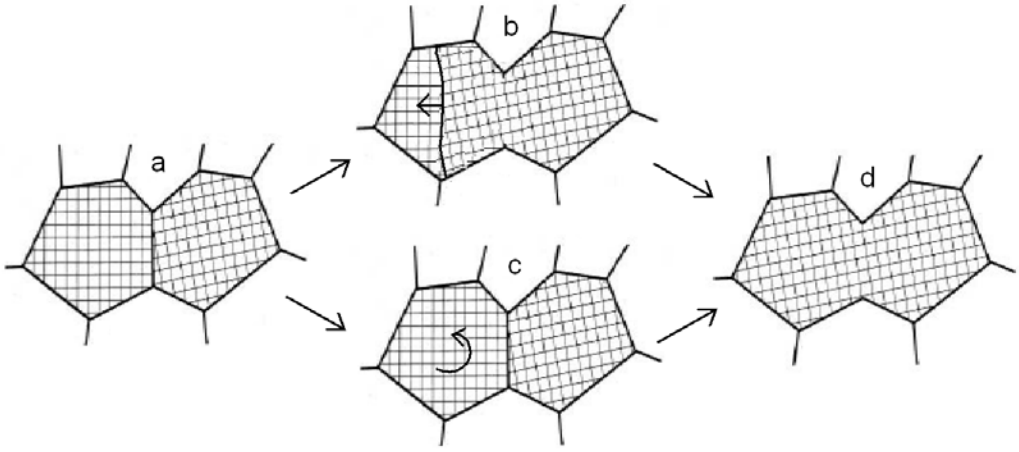

Figure 1.4: Subgrain coalescence by migration of low-angle boundary (b) and coarsening by rotation of subgrain (c). Adapted from [3].

sizes as well as higher angles of the subgrain boundaries are seen after recovery has proceeded for some time [3]. Figure 1.4 b) shows a low-angle boundary migrating through a subgrain to merge with the boundary on the other side. The end result is a larger subgrain of uniform orientation.

Another way for the subgrain size to increase is by the rotation of adjacent subgrains to obtain a similar orientation and eventually merge [17]. The rotation of each subgrain is affected by the orientations of all the neighboring grains, so this may not always be energetically favorable. However, at sufficiently high temperatures, it has been observed to occur [3]. Figure 1.4 c) shows how a subgrain rotates by a small angle to obtain the same orientation as a neighboring subgrain. Again, the final result is a larger subgrain.

Although a subgrain may in this way exceed the critical embryo size, it will only start to grow as a nucleus if it also has a high angle grain boundary to a neighboring grain or subgrain into which it may start to grow.

1.2.2 Strain-induced boundary migration

Strain-induced boundary migration or SIBM involves the formation of a bulge on a high-angle grain boundary which then proceeds to grow with an orientation similar to one grain into the other grain. It was first observed in 1950 [18] and is well established to occur in many metals, mainly for low strains [3, 19].

The process is illustrated in figure 1.5. The driving force is a difference

in stored energy between the two deformed grains $E_1 > E_2$, driving the nucleus to grow into the grain of highest stored energy. This difference may be local and vary along the boundary so that nuclei may grow into both of the deformed grains at different locations along the boundary.

The embryo may form by the mechanisms described in section 1.2.1, and the vicinity of the high-angle grain boundary provides the opportunity for growth [20]. The nucleus will have an orientation similar to the parent grain and may either retain some of the misorientations of the deformed structure (figure 1.5 b)) or be dislocation-free (figure 1.5 c)).

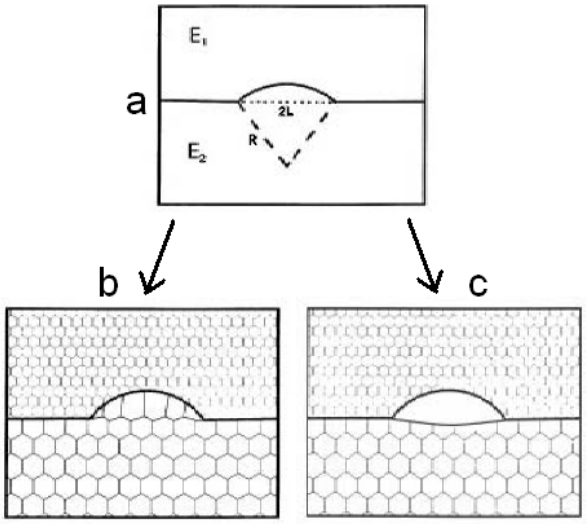

Figure 1.5: Strain-induced boundary migration. The initial embryo is a subgrain in the grain of lowest energy E_2. The nucleus in (b) is dragging the dislocation structure of the deformed grain, where the nucleus in (c) is a single crystal. Adapted from [3].

1.2.3 Twinning

Although twinning is not a nucleation theory, it is a mechanism for forming new orientations and is thus considered relevant for the present study [21]. Twinning is the process of forming twin-related crystal structures. A twin relation is a highly symmetrical relationship between two crystals. In an fcc structure, the coincidence site lattice (CSL), which consists of all lattice points common to both crystals [3], consists of a third of all atoms in the crystals for a twin relationship. Twinning is related to stacking faults, which

may occur in fcc metals if consecutive 111 planes are stacked wrongly. An fcc crystal consists of close-packed 111 planes stacked as ABCABCABC .... A stacking fault consists of either removing or adding a layer so that the layer sequence becomes ABCBCABC or ABCBABCABC [22]. But if the stacking order is reversed, the crystal structure is also changed, and a coherent twin boundary is created. Twin boundaries which do not coincide with a {111} plane are called incoherent twin boundaries and have a much higher boundary energy than the special coherent twin boundaries, although the energy will still be lower than that of a completely random grain boundary [23]. The twin relationship corresponds to a rotation of the crystal lattice by 60° around a $\langle 111 \rangle$ axis.

The twin boundary may either be formed during deformation or during growth. The readiness of a metal to form twins depends in the stacking fault energy γ_{SFE}. Where a metal with a low stacking fault energy such as brass will form many twins, a high stacking fault energy metal such as aluminium will form only a few.

1.2.4 Nucleation sites

The sites where nucleation is most likely to occur are considered to be the parts of the microstructure which have the highest local deformation, because the driving force for recrystallization (equation 1.5) is largest in areas with a high dislocation density. These sites are e.g.[3, 13, 24–27]:

- Grain boundaries (planes) between two grains. The interaction between the different grains may lead to a higher local deformation close to the boundary, and the pre-existing high-angle boundary may also facilitate strain-induced boundary migration (section 1.2.2)

- Triple junction (lines) where three grains meet have an even higher interaction than grain boundaries.

- Grain corners (points) where four grains meet are the end points of the triple junctions and again even more affected by neighboring grains.

- Transition bands where the grain has split into regions of different orientations during the deformation process. The high local deformation in these bands is ideal for nucleation.

- Shear bands, which are thin bands oriented at about 35°to the rolling plane. In these bands, the material is highly strained, providing good conditions for the nucleation process.

- Near second phase particles. Zones of high local deformation are common around less deformable second-phase particles, so subgrains of an orientation quite different from the surrounding grain may occur.

1.3 Formation of new orientations

In several cases, orientations that were not present in nor had a twin relation to the deformed state have been observed [27–46]. This section will give a short overview of the different theories that have been proposed to explain the formation of new orientations during recrystallization.

1.3.1 Overview of theories

As mentioned above, several different authors have observed new orientations formed during recrystallization. Understanding the underlying mechanisms of nucleation is vitally important for making realistic models of recrystallization. Modelling work has suggested the possibility of subgrains rotating toward boundary configurations of lower energy [47, 48], while direct *in-situ* observation of single subgrains is difficult. To explain these new orientations, several different theories have been suggested; some suggest that subgrains may rotate through reordering of the deformation-induced dislocation structure, while a mechanism that generates new orientations through dissociation of boundaries has also been suggested. The relevant theories are outlined below.

Inoko an coworkers [29–32, 35, 36] have made extensive studies of particularly single crystals and seen $\langle 111 \rangle$ rotations in fcc metals and $\langle 110 \rangle$ rotations in bcc metals, corresponding to the most close-packed planes. They suggest a mechanism where the nucleus is considered as a cylinder which may rotate around its axis by dislocation slip, forming edge dislocations around the sides and screw dislocations on the and faces. The new orientation are then obtained from the activation of at least two slip systems.

In the studies by Paul and coworkers [27, 28, 37–41] of single- and bicrystals, $\langle 111 \rangle$ rotations are also seen. However, they also observe rotations around other axes such as $\langle 112 \rangle$. In both cases, the rotation angles were in the range 25°-40° The model suggested to explain the rotations seen involves the thermally activated movement of dislocations on $\{111\}$ planes and predicts rotations about the normals to the slip planes of highest Schmid factor. Different activations of the slip systems are then predicted to lead to different rotation axes; $\langle 111 \rangle$-rotations are related to movement on one slip plane of two sets of dislocations containing screw components, forming a twist

boundary [27]. ⟨112⟩-rotations are related to a strong activity on a single {111}⟨110⟩-type slip system [38]. Finally, the mechanism of ⟨100⟩-rotations is caused by collective dislocation motion over two different {111} planes [40].

As the rotation mechanisms mentioned here rely on the reordering of the dislocation structure, it is important to understand the exact nature of this deformation-induced structure. As described above, the rotations are explained by motion of dislocations on slip planes, so the formation of slip plane aligned boundaries is important to accommodate the rotations. Huang and Winther [9, 49] describe the alignment of GNBs depending on the initial orientation to the direction of deformation. This will be described in more detail in section 4.3, where the theory will be applied to EBSP data from the present study.

Sabin et al. [42, 43] observed new orientations with ⟨111⟩ rotations of angles 10°-50° in a rolled specimen and tested the theories of Inoko and Paul. The best correspondence was found with the highest Schmid factor model of Paul et al.. The nuclei originated primarily at triple junctions, both on and below the surface.

A study of columnar grains by Wu and Juul Jensen [45, 46] found many nuclei of new orientations. A ⟨111⟩ rotation mechanism could explain some of the nuclei orientations, and some were suggested to be best explained by the dissociation of boundaries into several boundaries of higher symmetry.

1.4 Aim

The aim of this project is to study nucleation of recrystallization with a special focus on the possible formation of nuclei with new orientations. Although new orientations have been observed on numerous occasions as described above, the mechanisms by which they form are still poorly understood. In order to facilitate the development of new models for the understanding of nucleation, more data is needed on where the nuclei appear and what the orientation relationship between nucleus and deformed structure is.

This will be done using the two complementary methods of Electron Backscattered diffraction Patterns(EBSP) and Three-Dimensional X-Ray Diffraction (3DXRD), which are described in further detail in chapter 2.

The thesis is structured as follows:

Chapter 2 gives an introduction to the different experimental techniques used to complete the study described in the following chapters.

In chapter 3, a description of the work done during the course of this Ph.D.-study begins. The preparation of the desired starting material for the nucleation studies is described. It was essential to have a good initial struc-

ture with a reasonable grain size and boundaries of nearly minimal energy to have clearly-defined triple junctions in the material.

Chapter 4 describes the two-dimensional experiments which were performed at Risø DTU using the EBSP facilities in several scanning electron microscopes. A large number of samples and extent of total surface area were characterized in order to find the rather rare nuclei. A possible connection between slip plane aligned GNBs and the rotation axis of the nuclei seen to have new orientations is described.

A 3DXRD experiment was carried out. The experimental details are described in chapter 5 and the results are presented in chapter 6. A large gauge volume was mapped before and after annealing to nucleation, and the orientations and positions of 50 nuclei were found. Of these, 6 were away from any of the surfaces and constituted true bulk nucleation. These were studied further, their volumes found and the orientations in a layer of the deformed structure were compared with the nuclei present in this layer. An orientation imaging map of a cross-section in the sample was reconstructed from a layer before and another layer after annealing. An analysis of the slip systems was carried out in a similar manner as was done for the EBSP results. The data seemed to support one of two possible hypotheses concerning the rotation axis of the new orientations.

Chapters 7 and 8 provide conclusions on the project and suggestions for improvements.

Chapter 2

Experimental Techniques

The techniques used in this project were mainly EBSP and 3DXRD. These were chosen because they complement each other nicely, allowing a more thorough study of the problems posed in section 1.4. Some of the initial preparation of materials also used optical microscopy as a fast and reliable method of obtaining grain sizes and shapes.

Compared to optical microscopy, EBSP has the added advantage of giving the crystallographic orientation combined with a higher spatial resolution, although the method is slower and more elaborate. Over X-ray diffraction, EBSP has the main advantage of a much less complicated and time-consuming setup and data analysis, although the data acquisition time of 3DXRD might be somewhat faster. However, like optical microscopy, it is a surface method and as such it also suffers from some severe limitations. If the same areas are studied before and after nucleation, only nucleation occurring close to or on a free surface can be studied. This may not be representative of the behavior of the material in the bulk. Also, it can never be ruled out that any seemingly new orientations actually originate from small volumes below the surface which were not probed by the EBSP scan. If bulk measurements are to be taken, the sample must be polished to the desired depth after nucleation to observe the nuclei, and it is then impossible to determine what was present at the nucleation site before the nucleus appeared. This has been referred to as the problem of "lost evidence" [50].

3DXRD requires intense high-energy X-rays, which are available at some synchrotron facilities. The ID11 beamline at the European Synchrotron Radiation Facility ESRF has a dedicated setup for this purpose. The high penetration power of the hard X-rays makes it possible to study bulk samples in a non-destructive way. This allows for *in-situ* studies of the microstructural evolution, and can give information about position, morphology, phase, crystallographic orientation and strain [51].

Both of the methods of EBSP and 3DXRD are valuable tools in obtaining data for improving the existing models for microstructural behaviour.

2.1 Optical microscopy

For optical microscopy, the samples were prepared by mechanical polishing and etching. Using consecutive finer polishing down to 3 μm gave a surface sufficiently smooth to observe the undeformed grains. The sample surface was etched in an anodizing solution of hydrofluoric acid for the microscopy.

The optical microscope used for acquiring the images shown in chapter 3 is a Leitz Aristomet microscope coupled with a Leica camera and Leica IM500 image acquisition software. A polarizer can be inserted into the microscope to obtain orientation contrast between different grains in an etched sample when polarized light is used.

2.2 EBSP

It has been known since the 1950's that when electrons are scattered elastically from a crystalline sample, a diffraction pattern called a Kikuchi pattern forms [52]. Such a pattern can be seen in figure 2.1. But only in the 1970's did people start using this for a determination of the local orientations in a scanning electron microscope (SEM) [53]. Initially this was done by examining images on photographic plates, but in the 1980's, real-time imaging on a computer screen became available [54]. Still, each pattern had to be examined manually and the lines found in order to determine the crystallographic orientation [55]. In the 1990's, the use of the Hough transform and a masking system allowed fully automatic indexing [56] which has made EBSP systems an integral part of many modern SEMs.

EBSP relies on backscattering of electrons, which makes it a surface method. In order to obtain the maximum number of backscattered electrons, the sample should preferably be tilted at a high angle, usually around 70° [58]. Only the top ∼10 nm are probed [59]. When the electrons hit the material, they will be scattered diffusely in all directions. A few of these will have a wavelength λ that fulfills the Bragg condition [60]:

$$n\lambda = 2d\sin\theta \tag{2.1}$$

and be elastically scattered from the crystal planes of spacing d with a scattering angle 2θ. Only those electrons which are not scattered further after this interaction with the crystal lattice contribute to the pattern. These

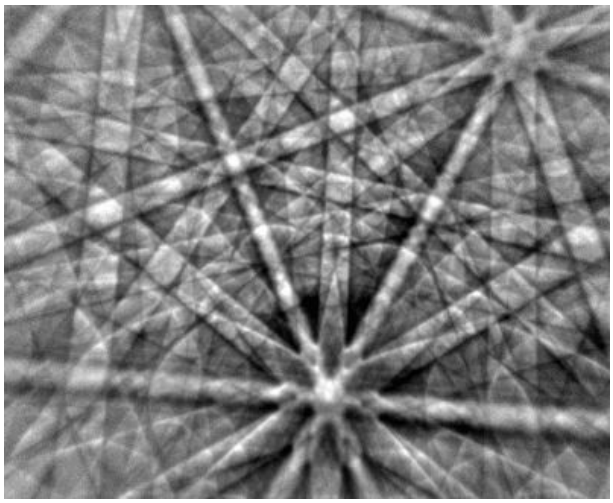

Figure 2.1: Kikuchi pattern from copper [57]. Each double line corresponds to a diffracting crystal plane.

elastically scattered electrons will form two cones with a shallow angle to the crystal plane - one above the plane and one below, as the diffusely scattered electrons meeting the Bragg condition may come from either above or below the plane. This gives a characteristic double line on a two-dimensional detector, as seen in figure 2.1. From this pattern of double lines, the crystal orientation can be calculated, and for multi-phase materials also the phase.

Using a FEGSEM, the resolution of the EBSP method may be as good as 15 nm [60].

For the present study, two scanning electron microscopes were used; a JEOL JSM-840 SEM with software by Niels Christian Krieger Lassen [61] and a Zeiss Supra FEGSEM with commercial HKL Channel 5 software [62]. While the JEOL microscope allows only stage scanning where the sample is physically moved in the electron beam, the Zeiss microscope is configured for both stage and beam scanning. Generally, beam scanning is much faster than stage scanning, however the orientations obtained by this method will be systematically off near the edges of large scanned areas.

The samples were mechanically polished in a way similar to that described for optical microscopy (section 2.1), but were not etched. To remove any strain caused by the mechanical polishing, the samples were electrochemically polished. This was done by immersing the sample in a solution of perchloric acid (A2 from Struers) cooled to a temperature of 2°-5° C with a potential difference of 13V between the sample and the aluminum cathode for about 45 seconds depending on the sample size. This caused a very thin oxidation

layer to form on the surface of the sample and peel off.

2.3 3DXRD

The 3DXRD microscope is situated at the dedicated materials science beamline ID-11 at the European Synchrotron Radiation Facility ESRF in Grenoble, France and is developed in a collaborative effort between the ESRF and Risø DTU. The first studies were conducted in the late 1990's [63, 64], and the success of the method helped facilitate the formation of the "Metal Structures in 4D" fundamental research center under which the present study was made. Subsequent investigations have studied such phenomena as grain rotation during deformation [65], recovery [66], recrystallization kinetics [67, 68], strain evolution [69], nucleation of recrystallization [34] as well as the reconstruction of 3D maps of grains and their boundaries [70, 71] and movies of grain growth [72, 73].

The 3DXRD methodology is based on the use of high-energy X-rays from a synchrotron source (typically of the order of 40-100 keV) for diffraction studies of bulk samples, typically polycrystalline materials such as metals, alloys and ceramics. The use of undulators gives a very high flux, which is necessary for studies of local phenomena in a material. The high energy of the X-rays give a high penetration power, which allows studies of mm to cm sized samples, while also giving quite a small diffraction angle (see equation 2.1). The small angle means that two-dimensional detectors may be used. Using detectors at different distances gives both spatial and crystallographic information.

2.3.1 Basic principles

The principle of the method is similar to EBSP as described in section 2.2 in that it also exploits the fact that the crystal planes in the grains give rise to Bragg diffraction (equation 2.1). However, where EBSP uses backscattered electrons, the hard X-ray setup is based on a transmission geometry. It is necessary for this method that the incoming beam is monochromatic, and the resulting diffraction image will then have spots at positions with an angle of 2θ to the incoming beam. For a point beam hitting a single- or polycrystal, this would result in diffraction spots appearing on rings at specific distances from the direct beam position on the detector, where the relative distances between the rings would be given by the structure of the crystal lattice. These rings are called Debye-Scherrer rings [74]. The distance between cubic

crystal planes of Miller indices (see section 1.1) hkl are given by [74]:

$$d_{hkl} = \frac{a}{\sqrt{h^2 + k^2 + l^2}}. \tag{2.2}$$

The planes that give rise to diffraction in an fcc lattice will be those whose Miller indices are all odd or all even, ie. {111}, {200}, {220}, {311}, {222} etc. Using this with the Bragg equation 2.1 gives the scattering angles as:

$$\theta_{\mathrm{hkl}} = \sin^{-1}\left(\frac{\lambda\sqrt{h^2 + k^2 + l^2}}{2a}\right) \tag{2.3}$$

It can be seen that although the absolute angles will depend on the lattice spacing a, the relative sizes of the angles will always be the same for all fcc metals. A powder diffraction pattern from gold, which has the fcc structure, can be seen in figure 2.2(a). The {311} and {222} are very close as expected from equation 2.3.

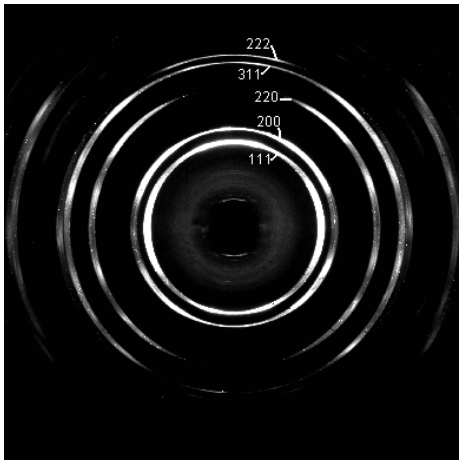

(a) Debye-Scherrer rings from a gold foil of random texture. The foil was used for calibration of the diffracting volume as described in section 6.1.3. The first five rings are marked with their Miller indices.

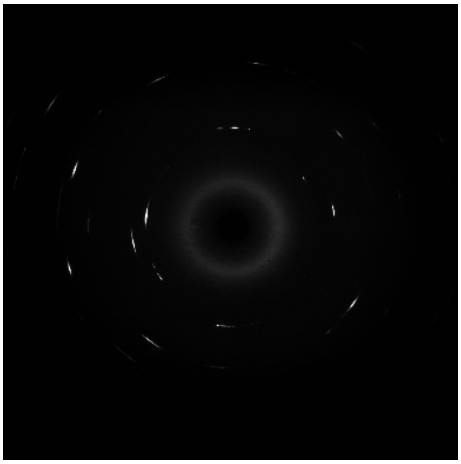

(b) A diffraction pattern from a deformed polycrystalline aluminium sample. The diffraction spots fall on rings similar to the powder rings and are somewhat broadened along the rings due to internal misorientations, but only parts of each ring has diffraction spots corresponding to only specific orientations being present in the sample.

Figure 2.2: Examples of diffraction patterns from a powder nearly filling out the orientation space and a deformed polycrystal with only some orientations.

However, the finite size of the beam and the sample-to-detector distance will cause the positions of the diffraction spots to diverge from perfect rings.

This can be used to find the positions of individual grains within the sample by triangulation from several diffraction images.

Another method for obtaining spatial information is by tracking [71], where identical scans are performed at several detector distances. The displacement of each diffraction spot on the detector allows a line to be drawn back to a position inside the sample corresponding to the diffracting volume element.

To see all grains and obtain enough information about each individual grain in a crystalline sample, the sample can be rotated around a vertical axis and images recorded at several different rotation angles ω. This means that several different diffraction spots from each individual grain are recorded. The ω-range necessary for orientation indexing depends on the number of Debye-Scherrer rings which are visible and have discernible diffraction spots on the detector. The total number of diffraction spots a grain will give on a single ring if rotated 360° is equal to twice the multiplicity, as each scattering vector comes into a diffracting condition twice. E.g. there will be 16 {111} reflections corresponding to (111), $(\overline{1}11)$, $(11\overline{1})$, $(\overline{1}1\overline{1})$, $(1\overline{1}1)$, $(\overline{1}11)$, $(1\overline{1}1)$ and $(\overline{1}1\overline{1})$.

2.3.2 Optics etc.

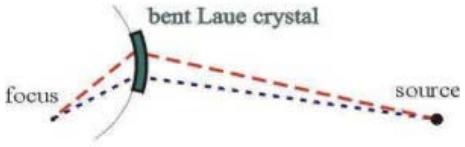

Figure 2.3: Bent Laue crystal focusing geometry [75].

The beamline ID-11 consists of three hutches; an optics hutch directly after the front end and two experimental hutches. The second experimental hutch was installed in 2007 at a larger distance (about 100 m [76]) from the ring to allow increased focusing of the beam to achieve sub-micrometre resolution. This section describes what happens to the X-ray beam in order to obtain the desired properties before it enters the experimental hutches.

The X-ray beam is generated in the synchrotron ring by use of undulators. An undulator consists of a series of powerful magnets placed along the electron beam in the synchrotron ring. The magnets cause the electrons to follow a sinusoidal path, emitting X-rays due to their acceleration. The

period of the sinusoidal curve can be tuned by the distance between the magnets, and the undulator is constructed so that the radiation emitted by the electrons in one oscillation is in phase with the radiation emitted in the next oscillation, giving an increased intensity as well as a quasi-monochromatic beam [74].

For focusing and monochromatizing of X-rays, some special optical elements are necessary. For the experiments described here, a bent Laue crystal was used for focusing the beam in one direction [75]. The Laue crystal is placed so that the X-ray beam passes through the crystal. The crystal is a perfect Si single crystal, and the lattice planes inside the crystal are used to monochromatize the beam. The bending of the crystal allows the X-ray beam to be focused in one direction. The Laue crystal geometry is shown in figure 2.3.

Apart from the focusing, several slit systems are also available for beam definition and conditioning.

2.3.3 Detectors

Several detectors are available in the experimental hutches, from diodes for measuring a single point to the two-dimensional detectors used for recording diffraction images [80]. The 3DXRD method makes extensive use of two-dimensional detectors at different distances from the sample to obtain three-dimensional information. This may either be done by tracking [71, 81, 82], where the same mapping is done several times with the detector at different distances, or by using several different detectors simultaneously.

The Quantix detector with a pixel size of $4.3 \times 4.3\mu$m and the Sensicam detector with a pixel size of $1.3 \times 1.3\mu$m are with their relatively small pixel sizes commonly used at small distances from the sample (of the order of 1 cm). This type of detector is referred to as a near-field detector, and is also the type of detector used for tracking.

Another type of detector with a much larger pixel size are the Frelon2K and Frelon4M detectors. With pixel sizes of $48 \times 49\mu$m and $50 \times 50\mu$m respectively, they are usually placed at a much larger distance from the sample (tens of centimetres). This type of detector is known as a far-field detector and gives much clearer information about the crystal orientations in the sample, while the near-field detector is better suited for obtaining spatial information.

The efficiency of the detectors is very different, which means that if several detectors are used simultaneously, the best detector may have to be attenuated or a reduced resolution on the poorest detector must be accepted. For the experiment described in chapters 5 and 6, the Frelon2K and the Quantix

detectors were used. In order not to increase the time taken to collect data beyond reason, the most efficient detector, which was the Frelon, was not attenuated. This resulted in much poorer resolution on the Quantix detector, but was deemed necessary.

The dynamic range of the detectors is also very important. When working on nucleation, very small volumes need to be detected. It is therefore important to be able to detect diffraction spots of a very low intensity on the detector while at the same time the very large diffraction spots from the large deformed grains do not saturate and damage the detector. Where the Quantix detector e.g. has a dynamic range of 2^{12}, the Frelon detectors have a dynamic range of 2^{16}, allowing them in theory to detect diffraction spots that are 16 times weaker in a given sample if both detectors were exposed until saturation. Effectively, however, it will not be possible to detect diffraction spots from extremely small elements, as there will be a background noise level on the detectors due to diffuse scattering from the air, the furnace etc.. In the data analysis, a threshold of a minimum number of counts per pixel is therefore usually applied.

2.3.4 Sample environment

The sample tower allows translations in x, y and z as well as tilting and rotation, all with an accuracy of 1 μm [83]. Furthermore, the sample environment can be controlled using a cryostat, a tensile machine and several furnaces. An example of a setup is shown in figure 2.4.

For the studies described in chapters 5 and 6 and appendix B, the furnace shown in figure 2.5 was mounted on the sample tower and the sample was placed inside the furnace for the duration of the experiments. The furnace consists of a heated copper rod where the sample is mounted in a groove at the top. The sample and heating element are enclosed in a quartz tube which gives only a minimal diffuse scattering of the X-ray beam. Inside the tube, argon can be continuously pumped in to give a slightly higher pressure than the surrounding atmosphere. This is to prevent any oxidation of the sample surface during the heating. A thermocouple touching the sample allows for temperature control. When the furnace has been calibrated with the test sample, the temperature can be reproduced within a few degrees and remains stable within a few tenths of a degree throughout the heating time. After heating, the sample is allowed to cool inside the furnace in order to reduce the need for recalibration. For the experiment, the heating rate was about 30 K/minute and the initial cooling rate was 25 K/minute.

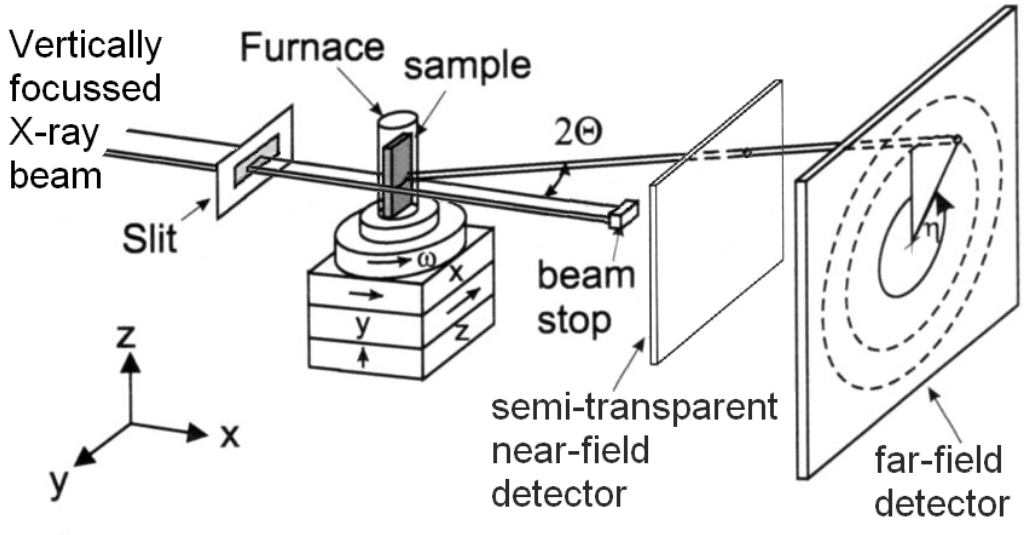

Figure 2.4: The setup used for the 3DXRD-experiment in chapters 5 and 6.

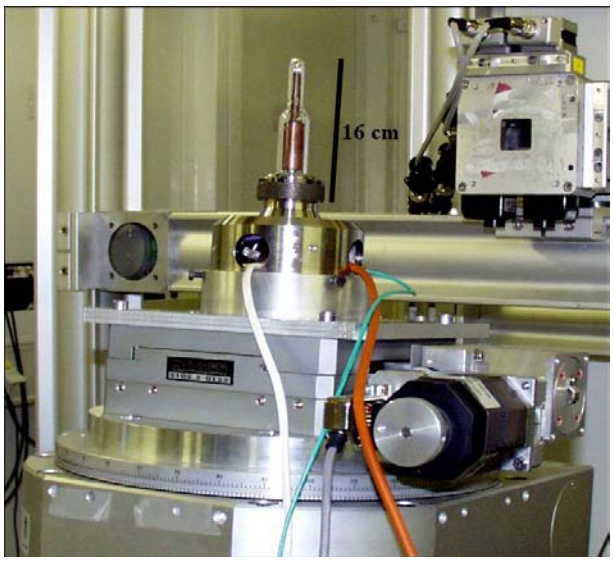

Figure 2.5: The furnace mounted on the sample stage in the X-ray hutch. The sample is situated at the top of the copper rod inside the quartz tube.

2.3.5 Software

The data resulting from a 3DXRD experiment consists of a number of diffraction images. In order to extract the desired information from these, extensive data analysis is required.

For the 3DXRD microscope, a collection of software under the name Fable has been created by various people at Risø and ESRF [84]. The software can be downloaded from the Fable webpage [85], where new applications are continuously being added. The package contains applications for viewing and analyzing diffraction images, peak searching, mapping grains and their orientations, simulating data and many other possibilities.

Some of the main programs used in the data analysis of the experiment described in chapters 5 and 6 are described below.

Grainspotter and ImageD11

For finding the orientations of individual grains, previously the program called GRAINDEX has been used extensively in 3DXRD experimental analysis [81, 86]. This program may index several hundred separate grains in a polycrystal, but the relatively long running time (of the order of half an hour) has prompted the development of another orientation indexing program called GrainSpotter [87].

The input for this program is a set of G-vectors corresponding to the scattering vectors of each diffraction spot found in the detector image. The method for finding these G-vectors is as follows:

Initially, the diffraction spots can be harvested using the Fable GUI program ImageD11, which allows peaksearching (i.e. finding all individual diffraction spots) above a given threshold. The output will contain all peaks with intensities higher than the given threshold, and may be further filtered by many parameters such as the standard deviation of a fitted Gaussian, which may be helpful if only the spots from undeformed grains are wanted. This can help isolate the recrystallized nuclei, as can be seen in chapter 6. ImageD11 may also be used to calibrate such global parameters as detector distance and tilt. With these parameters in place, the position of the peaks in reciprocal space are found, giving the G-vectors corresponding to the diffraction spots.

GrainSpotter uses a pattern recognition algorithm to compare the sets of given G-vectors with a list of theoretical G-vectors. The discrete set of rotations that bring the theoretical scattering vectors into a subset of the measured G-vectors gives the crystallographic orientation of each of the diffracting grains in the material.

Grainspotter has also been extended to include a facility to obtain the center-of-mass position of a grain. When the sample is rotated, the position of the grain will also change, unless the center-of-mass of the grain coincides exactly with the rotation axis. This will give rise to a deviation in the spot position on the detector from the ideal position given by the best fit orientation. The further away from the sample the detector is, the smaller this deviation will be relative to the distances the Debye-Scherrer rings. On the near-field detector, these deviations are relatively large so that the Debye-Scherrer rings cannot be readily identified. On the far-field detector images, they are small compared to the size of the rings, but still measurable. This allows a triangulation of the center-of-mass position of the nucleus inside the sample, even from the far-field data.

GrainSweeper

For reconstruction of entire 3D volumes, the GrainSweeper program is available [88]. This was originally developed for the reconstruction of undeformed material, but has also proved capable of handling deformed structures. The resolution of the grain maps reconstructed by this method is given by the detector.

The program uses a so-called forward reconstruction algorithm. As input, it directly uses the diffraction images of the ω scan, which are subtracted by their median to remove background noise. The images are then deconvoluted with a point spread function using the Richardson-Lucy algorithm in order to remove blurring happening in the detector.

A grid corresponding to positions inside the sample is defined, and for each point, the orientation distribution function (ODF) is calculated in orientation space. This gives a distribution of possible orientations, and the orientation with the highest completeness is assigned to the point.

The output is similar to the maps given by EBSP (see section 2.2). However, the method of reconstruction is very different, as the EBSP map is reconstructed point by point, where the 3DXRD microscope examines the entire cross-section of the sample at the same time.

Chapter 3

Selection and Development of the Starting Material

The material chosen for the present studies of nucleation of recrystallization was high-purity aluminum. This was deemed to be a good model material where the effects of grains and their orientations and boundaries could be studied. The high purity minimized the chance of having second-phase particles as well as the effects of alloying elements. Aluminum was chosen due to its relative high stacking-fault energy, which would minimize the formation of twins, as the focus of the study was new orientations formed by mechanisms *other* than twinning.

As nucleation was expected to occur primarily at triple junctions in this type of material [89], the triple junction geometry was very important. The triple junctions should have the low-energy configuration of three grains meeting at 120° angles. The importance of the grain size lay in the interaction between neighboring triple junctions both during the deformation and annealing. If triple junctions were too close, a grain nucleating at one triple junction might quickly grow to consume neighboring triple junctions, rendering the analysis of nucleation sites impossible. On the other hand, grains should not be so large that the number of triple junctions in a given volume was too small. The ideal grain size was deemed to be of the order of a few hundred micrometres. Finally, the distribution of sizes should not be to wide in order to have comparable data between samples. This turned out to be quite difficult, as some grains tended to grow very much larger than the rest. This so-called abnormal grain growth may be due to texture effects, i.e. if most grains had orientations close to each other, grains of a different orientation would have an advantage during the process of grain growth.

The different methods used in the preparation of the material to obtain the desired structure are explained in the following two sections, and finally

the actual treatments that were done are described and listed.

3.1 Rolling

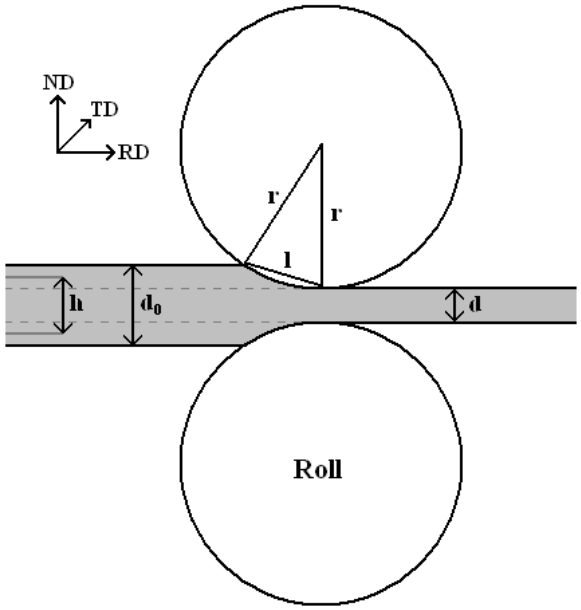

Figure 3.1: Rolling geometry.

The geometry of rolling is often characterized by the l/h ratio, where l is the contact length between roll and sample, and h is the material thickness. There are different ways of defining l/h. Here, the contact length will be approximated by a straight line, and the material thickness is taken as the average of the thickness before and after the rolling draught. (These lengths are illustrated in figure 3.1). The l/h ratio is then given as:

$$\frac{l}{h} = \frac{2\sqrt{r(d_0 - d)}}{d_d + d}, \tag{3.1}$$

where d_0 and d are the material thickness before and after the rolling, respectively, and r is the radius of the roll. Mishin et al. [90] define small-draught rolling as having $l/h < 0.5$ and large-draught rolling as having $l/h > 5$. To obtain a homogeneous deformation, the rolling draughts should be of intermediate size, i.e. $0.5 < l/h < 5$ [91].

A measure of the reduction in thickness of the material is the true or logarithmic strain. The true strain for compression is defined as [8]:

$$\epsilon_{\text{true}} = \ln \frac{d_0}{d}. \tag{3.2}$$

The coordinate system defined for a material deformed in rolling is given by the following three axes: **RD** is the rolling direction, i.e. the direction of the material motion through the rolls. **ND** is the normal direction, i.e. the direction from the sample toward the center of the roll (the system is symmetric, so ND can be toward the center of any of the two rolls). **TD** is the transverse direction given by TD=ND×RD. This coordinate system is marked in figure 3.1.

For the present experiments, a rolling mill of radius 170 mm was used, and the material was rolled at room temperature without quenching. Petroleum was used for lubrication.

3.2 Furnaces

Several different furnaces were used for the annealing treatments during the experiments.

The air furnaces allowed temperatures up to 1000°C or 1200°C. These furnaces could be pre-heated to the desired temperature before insertion of the sample and held stable within a few degrees. The sample was placed in a small porcelain crucible or directly inside the furnace. Due to some uncertainty on the actual temperature at the sample location within the furnace chamber, this type of furnace was best suited for annealing treatments of quite a long duration where the requirements on the precision of the temperature were not too great. Along with the fact that the surface of the sample was in direct contact with air causing oxidation, this meant that the air furnaces were primarily used for the initial annealing treatments of large pieces of material for further processing. For this type of treatment, quenching was not used in order to minimize the amount of strain remaining in the material.

A tin bath was used to anneal smaller samples to induce nucleation. The tin bath had a well-controlled temperature and switched between annealing and room temperature almost instantly, as the sample quickly reached temperature when submerged into the liquid tin, and was quenched in water afterwards. The sample was wrapped in aluminum foil when submerged in the tin bath to avoid contamination of the sample.

Another furnace used was described in section 2.3.4. This furnace was primarily used because it allowed *in-situ* examination in the 3DXRD microscope, and will be referred to as the 3DXRD furnace. As the sample needed

to be heated and cooled between room temperature and the annealing temperature along with the furnace, it was observed that much shorter annealing times were often needed to obtain nucleation compared with the times used with the tin bath.

3.3 Initial annealing treatments

The initial material received had an unknown processing history that provided a highly-deformed and partially recrystallized microstructure. In order to remove as much of the strain as possible, the material was initially annealed at 630°C for 24 hours in an air furnace to ensure complete recrystallization. This corresponds to $0.97T_m$, i.e. very close to the melting temperature of aluminum (660°C). The resulting material had grain sizes of up to several centimetres.

This material was then rolled to a logarithmic strain of 2, i.e. the reduction in thickness was 86.5%. This relatively large reduction ensured that there was plenty of energy to initiate recrystallization stored in the material. A fairly uniform distribution of this stored energy was obtained through rolling with intermediate draughts of l/h about 1.7 in 15 passes.

The second annealing treatment was crucial in obtaining the desired grain size in combination with straight boundaries and low-energy triple junctions. A series of temperatures and annealing times were systematically tried to observe the effects of tuning these parameters. This second annealing treatment was also done in an air furnace, as the annealing time was again long because the samples needed to be completely recrystallized. The long annealing times also meant that not only recrystallization but also grain growth took place in the material. Samples were cut from the material after the different treatments and observed by optical microscopy, as the important parameters at this stage were grain size, grain morphology and size distribution.

Table 3.1 lists the different temperatures tried. The lowest temperature of 150°C failed to create boundaries of minimal energy, even at long annealing times. Figure 3.2 shows a sample after 24 hours of annealing at 150°C. Some of the boundaries appear crystallographic like e.g. coherent twin boundaries, i.e. the reason why they are completely straight is that they coincide with crystallographic planes. Optical microscopy does not allow determination of which crystallographic planes this may be. Other boundaries however, appear very jagged, and the grains do not meet in neat triple junctions.

The temperatures of 300°C, 320°C and 350°C were also tested. Figure 3.3 shows a sample annealed at 300°C. The boundaries and triple junctions are much more satisfactory at this temperature. A very inhomogeneous size

T_1 /°C	t_1 / h	ϵ_{true}	T_2 /°C	t_2 / h
600	4			
	7			
	16			
630	24	2	150	7
				24
			300	6
				18
				24
			320	2.5
				4
				6
				16
			350	2.5
				6
				16
				20
				24

Table 3.1: Different annealing temperatures and times used to obtain the desired structure from the as-delivered material. The material was annealed at the temperature T_1 for the time given by t_1. The material that had been annealed at 630° C for 24 hours was then rolled to strain 2 and several annealing temperatures and times (T_2, t_2) were tested.

Figure 3.2: Material annealed at 150°C for 24 hours.

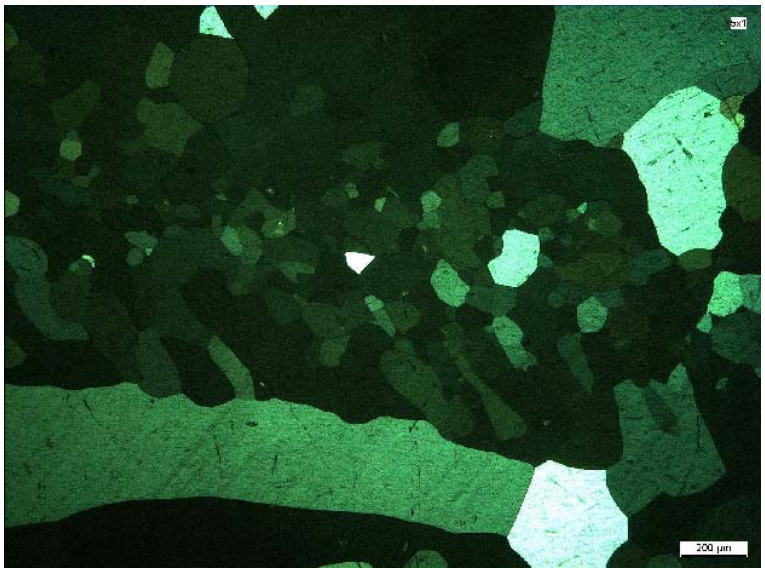

Figure 3.3: Material annealed at 300°C for 24 hours.

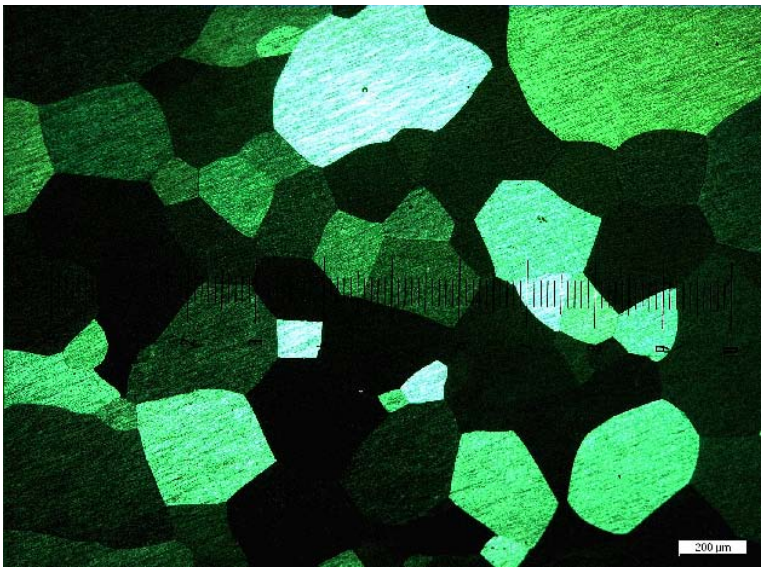

(a) Close to ideal grain size distribution.

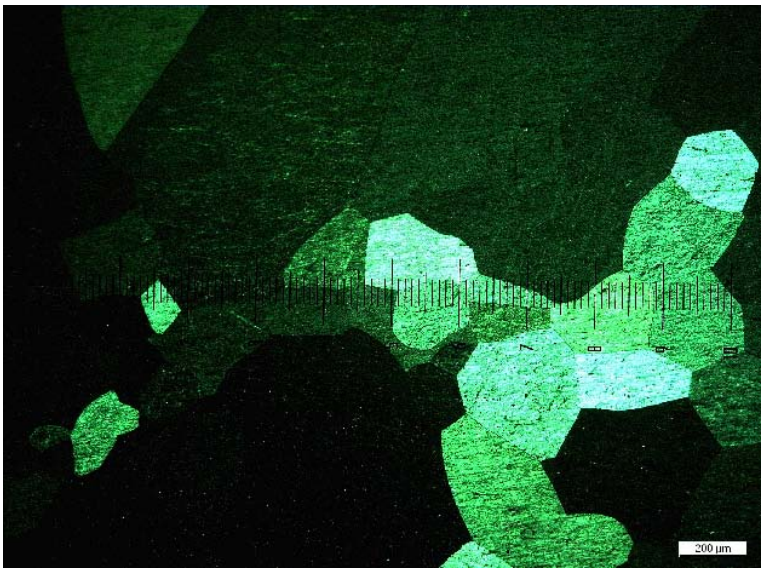

(b) Less ideal grain size distribution.

Figure 3.4: Two different samples from the same material annealed at 350°C for 24 hours. Although the desired grain sizes can be obtained in some parts of the material, abnormally large grains still occur in other parts of the material.

distribution is seen, as a few grains have grown very large. As the crystallographic orientations of the grains were not found, it cannot be concluded whether this was due to texture, influence from the surface of the material or other effects. The distribution of grain sizes is thus bimodal, with some grains of 50-100μm and others of the order of millimetres. A higher annealing temperature gave a larger grain size, as can be seen in figure 3.4. Although some millimetre-sized grains still appeared, the other grains had the desired size of a few hundred micrometres. The relative deviation of the large grains from the desired size was considered within acceptable limits for this annealing treatment. The average grain size was close to 500 μm with sizes ranging from 100 to 1000 μm.

No significant difference in grain sizes was seen between annealing times 16, 20 and 24 hours at 350°C, but the largest annealing time was chosen to minimize the boundary energy. The material showed a satisfactory morphology of boundaries and triple junctions. Grain boundaries were curved but not jagged, and most of the triple junctions showed close to 120° angles. As boundaries and angles are not necessarily viewed edge-on, it is expected that some angles should deviate from the ideal configuration. The distribution of angles was measured at a number of triple junctions in several samples cut from this material. The distribution can be seen in figure 3.5. 86% of the angles lie in the interval [90°,150°] before deformation. After 30% deformation, this fraction is 74%. An estimate based on the worst-case scenario of all angles above 120° being compressed in a direction to make them larger and all angles below 120° being compressed in a direction to make them smaller shows that the fraction should be at least 50%. As the triple junctions are actually oriented at random angles to the direction of compression, the fraction found seems reasonable.

3.4 Deformation

After a satisfactory starting material had been produced, the nucleation studies could begin. However, the ideal conditions for nucleation still had to be determined. To initiate nucleation, the material should be deformed in order to store energy for recrystallization in the material structure. This deformation should not be too great as the original grains and boundaries should still be discernible. This was in order to have a well-defined orientation within each deformed grain, but with some internal orientation spread due to the deformation. As grain boundaries and triple junctions are preferential nucleation sites [24], nucleation was expected to occur primarily at these sites, allowing a comparison of the orientation relationship between the deformed

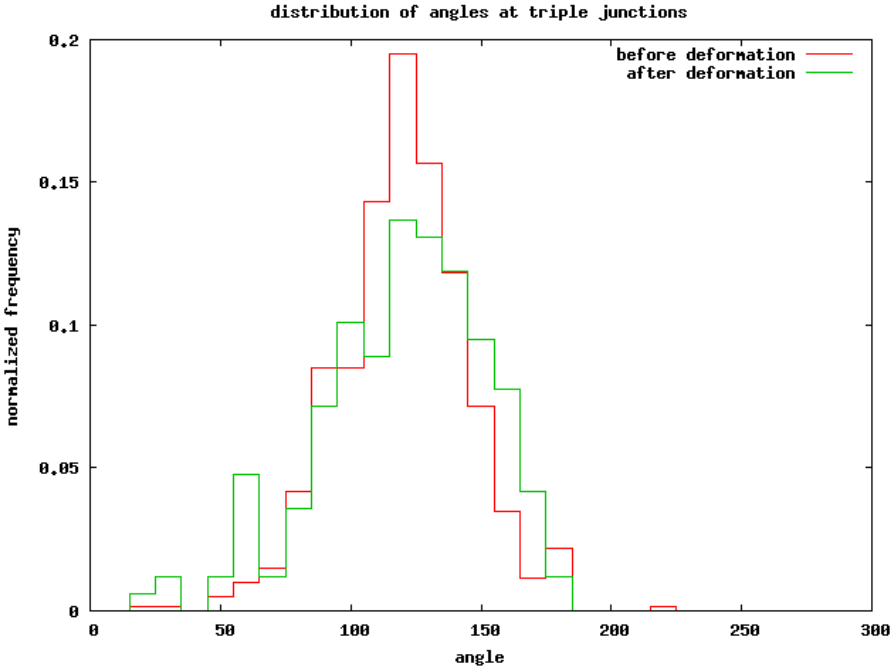

Figure 3.5: Distribution of angles at 200 triple junctions in the undeformed starting material ($T_1 = 630, t_1 = 24, \epsilon = 2, T_2 = 350, t_2 = 24$) and at 56 triple junctions after 30% deformation of the same material.

structure and a nucleus.

To ensure a homogeneous distribution of stored energy in the material, rolling with draughts around 2 were used again. The material was deformed to 20% or 30% reduction in thickness, corresponding to $\epsilon_{\text{true}} = 0.22$ and $\epsilon_{\text{true}} = 0.36$. It was then annealed at different temperatures and observed by optical microscopy or EBSP. The 30% deformed material was chosen for further experiments as having the best possibility of forming nuclei of new orientations due to the higher stored energy. The original grain structure was still clearly visible although internal deformation was apparent. As the material was to be used for both EBSP and 3DXRD experiments, deformations above 30% were not practical, as this would render reconstruction of the 3DXRD data difficult if not impossible.

3.5 Annealing to nucleation

After the material had been deformed, a series of different temperatures and times had to be tested in order to determine a suitable treatment. The goal was to find a temperature and time which would give many nuclei without letting them grow so large that their points of origin could not be determined.

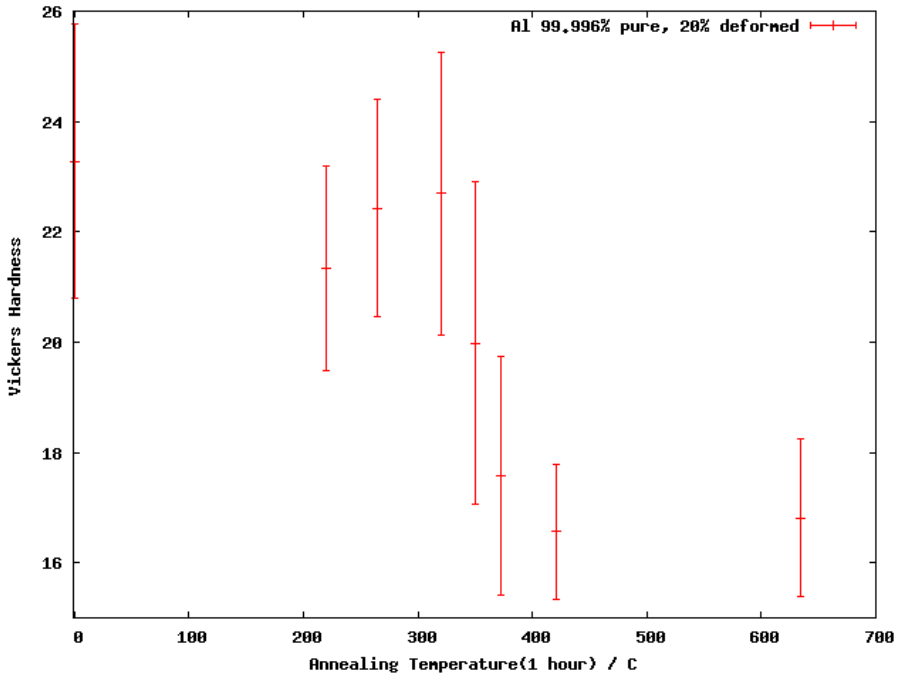

Figure 3.6: Vickers hardness tests of samples annealed for 1 hour at a given temperature. The hardness remains more or less constant up to 320°C and then drops. For the low temperature, only recovery has taken place, but for temperatures above the recrystallization temperature, which is seen to be somewhere between 320°C and 350°C, at least partial recrystallization has taken place.

As the annealing times used were relatively short, the tin bath was used for the initial tests to find the appropriate temperature, and finally the 3DXRD-furnace was used to optimize the annealing time. Hardness indent tests on the 20% deformed material with temperatures between 220°C and 630°C showed the recrystallization temperature to be around 350°C, as can be seen in figure 3.6. 10 different indents were made for each annealing treatment using a load of 50 g. The standard deviations are plotted as error bars on the figure. For the more highly deformed 30% material, the recrystalliza-

tion temperature was expected to be somewhat lower due to higher stored energy. Tests were therefore done with annealing at temperatures 300°C, 310°C, 315°C and 320°C for times between 20 and 45 minutes. The optimal annealing treatment was concluded to be 320°C for 30 minutes, although large variations in nucleus population were seen between samples when several different samples were exposed to this treatment due to the relatively low number of grains in each sample. An example of nucleation can be seen in figure 3.7.

The 3DXRD furnace was used for both the EBSP and 3DXRD experiments to have comparable data. Samples were annealed at 315°C, 320°C and 325°C in this furnace to determine if there was any difference in annealing behavior from that seen in the tin bath. No detectable difference in the nucleation rate as a function of temperature was seen compared to the significant variations between individual samples. However, the ideal annealing time in the 3DXRD-furnace was shorter because the sample was also placed inside the furnace while it was heating up and cooling down.

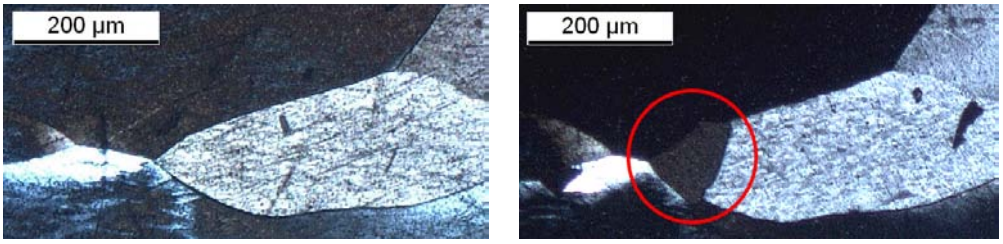

(a) Before annealing. (b) After annealing.

Figure 3.7: Nucleation seen by optical microscopy in a sample deformed 30% and annealed for 30 minutes at 320°C. The sample was etched for the first micrograph, then lightly polished before annealing in the tin bath, then etched again for the second micrograph.

3.6 Summary

Table 3.2 lists the final treatment leading to a satisfactory material for nucleation studies. The average grain size was 500μm and the boundaries and triple junctions were in a low-energy configuration.

The last three columns in the table show the treatments used to obtain nucleation. Rolling to 30% reduction gave grains that were still easily recognizable and a suitable nucleation could be induced for both ex-situ EBSP experiments and *in-situ* 3DXRD experiments in the 3DXRD furnace.

T_1 /°C	t_1 / h	ϵ_{true}	T_2 /°C	t_2 / h	$\epsilon_{\text{true, nucl}}$	T_{nucl} / h	t_{nucl} / minutes
630	24	2	350	24	0.36	315-325	10-20

Table 3.2: Final treatment. The nucleation time and temperature (t_{nucl} and T_{nucl}) refer to annealing in the 3DXRD furnace.

Chapter 4

Nucleation Studied by Electron Backscattered Diffraction Patterns

The EBSP method was described in section 2.2.

This chapter describes the series of EBSP experiments performed on high-purity aluminum samples to study nucleation of recrystallization [92]. The surfaces of the samples were studied before and after nucleation had occurred. No polishing was done after annealing to nucleation, so nucleation occurring at or close to the free surface was studied. These experiments were carried out to provide a background for the 3DXRD experiments described in chapters 5 and 6.

4.1 Experimental

4.1.1 Sample material and treatment

The material used for these experiments was the result of the preparations described in chapter 3. It consisted of 99.996 % pure aluminum with an average grain size of 500 μm that had been deformed by cold rolling to a reduction in thickness of 30 %.

From the deformed material several samples were cut with a surface in the ND-TD plane. This surface was first mechanically polished and then electrochemically polished in a solution of perchloric acid to remove any surface strain from the mechanical polishing (see section 2.2 for more detail).

The annealing took place in the furnace described in section 2.3.4 at temperatures between 315° C and 320° C for times of 10-15 minutes. The

treatments are listed in table 4.1.

Sample	T / °C	t / minutes
A	320	15
B	320	15
C	315	15
D	315	15
E	315	12
F	320	10
G	320	15

Table 4.1: The annealing time and temperature for the seven samples labelled A-G.

4.1.2 EBSP characterization

The characterizations were done in one of two different microscopes; a JEOL JSM-840 SEM using the in-house orientation indexing software Cromatic by Niels Christian Krieger Lassen [61] and a Zeiss Supra FEGSEM using commercial HKL software [62]. In the JEOL microscope, a step size of 10 μm was generally used due to the rather slow scan time (a scan of $\sim 0.5\times3$mm took of the order of 24 hours), while the scans done in the Zeiss microscope used step sizes of 2-5 μm (even with the smaller step size, a similar area could be covered in only a few hours). It was deemed more important to cover a large area than to have a high spatial resolution in order to see as many nucleation events as possible. Also, the whole sample area and not just triple junction areas was characterized, although nucleation was expected to occur mainly at triple junctions and grain boundaries. This would allow a more complete description of the nucleation sites, including any connection between a nucleation site and orientation. In total, more than 15 mm^2 were characterized. The complete EBSP maps can be seen in appendix A, where the annealing treatments are also listed.

As described in section 2.2, the crystallographic orientation was found by a fit to a Kikuchi pattern (see figure 2.1). To obtain the highest accuracy, 8 lines were normally fitted. Due to imperfections in the surface preparation or the depth of focus of the microscope, it was sometimes only possible to fit a smaller number of lines. Two overlapping patterns obtained by focusing directly at a grain boundary might also lead to only a few lines being fitted. This increased the risk of obtaining an incorrect fit to the orientation. To retain the maximum amount of correct data while removing any erroneously

indexed points, a double criterion was set up; all points which had only four Kikuchi lines or less *and* had four high-angle boundaries to the surrounding points (where high-angle boundaries were defined as having a misorientation of more than 10°) were excluded from the data set. This criterium worked well as the initial grain size was much larger than the step size of the scan, and the deformation of 30% was insufficient to be likely to induce local deformations large enough to produce four high-angle boundaries around an area of the order of the step size.

Some artifacts were visible in the EBSP maps due to the coloration scheme used for the orientation maps based on the Euler angles. If one of the Euler angles was close to zero, the color of two neighboring points which were close in orientation might have widely different colors. However, the use of white and black lines for low- and high-angle boundaries allows this type of artifact to be distinguished from boundaries between grains of different orientations.

As the samples were remounted in the microscope after the annealing treatment, a slight misalignment could sometimes be seen between the orientations before and after annealing. This misalignment could be corrected for in the comparison of the orientations, but sometimes gave an altered color due to the effect mentioned above. Where appropriate, these artifacts will be mentioned in the figure descriptions.

4.2 Results

A total of 29 nuclei were seen in the 7 samples. The nucleation was very inhomogeneous - some samples had many nuclei while others had only one or a few. This was due to the large grain sizes of the samples, making the samples themselves inhomogeneous in the distribution of grain orientations and boundaries. The nuclei were seen both at grain boundaries, triple junctions and a few in grain interiors.

The samples were named A to G as in table 4.1 and the nuclei were given names based on the sample they appeared in and a number. Nuclei C02, C03, D01, D03, D04 have been left out of the analysis, as there was at least one pixel present in the deformed state with an orientation similar to the orientation of the nucleus, although this orientation was different from the orientation of the large deformed grains. Whether these pixels were merely erroneously indexed, or some nucleation had already taken place during the deformation or due to mechanical stress during the polishing is unknown. Other nuclei extending outside the examined area were also observed, but were excluded from the analysis, as the point of origin may have been in the

area that was not characterized.

The orientations of the nuclei were compared with the orientations at the nucleation site in the deformed sample. The nucleation site area was defined as the area which the nuclei came to occupy after the annealing plus an extension of about 20 μm. The extra area was included to ensure complete coverage of the nucleus area regardless of any misalignment between the two characterizations. Figure 4.1 illustrates two areas that were compared.

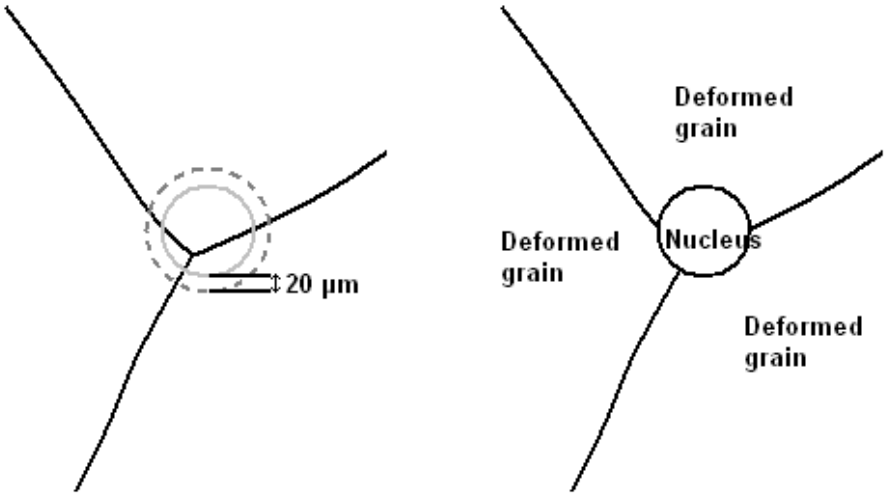

(a) Nucleation site before annealing. The area used for comparison with the nucleus orientation is marked by a dashed line. This will be referred to as the "nucleation area".

(b) Nucleation site after annealing with nucleus.

Figure 4.1: The areas of the two characterizations were compared. The orientation of the nucleus after annealing is compared with all orientations in the area later occupied by the nucleus plus an extension of 20 μm.

The remaining 24 nuclei fell into one of three types:

I Nuclei with an orientation within 10° of the orientation spread of one of the deformed grains. These are referred to as parent-oriented nuclei, and 14 nuclei were of this type.

II Nuclei with an orientation not present at the nucleation site before annealing and not first order twinned to any orientation present there. The 8 nuclei that fall into this category were all at least 11° misoriented to the closest orientation found in the nucleus area before annealing with an average misorientation of 29°. They showed a variety

of relationships to the initial orientations at the site. Some of these nuclei were adjacent to each other and exhibited a $60°\langle 111\rangle$ relationship, i.e. they were twins. This indicates that that they were so-called recrystallization twins, i.e. the twinning had most likely taken place after the nucleation [39]. As it was not possible to determine which of these nuclei appeared first, all 8 nuclei are included in the analysis of orientation relationships between parents and nuclei to be described in section 4.3.

III Nuclei with a first order twin relationship to one of the deformed grains. There were 2 nuclei of this type. Twinning is usually considered to be a relatively rare event in aluminum due to the high stacking fault energy, but the mechanism of twinning is well accepted and thus the annealing twins will not be considered in the following slip system analysis which aims to add to the understanding of the formation of new orientations other than twins.

Previous studies [43, 46] have divided nuclei into two or three types in a similar manner, depending on whether twins were observed or not.

Tables 4.2, 4.3 and 4.4 show an overview of the 24 nuclei. They have been divided into the three types I-III described above. It is seen that 15 nuclei appeared at triple junctions, 6 at grain boundaries and 3 in grain interiors. However, the nuclei in grain interiors all shared a boundary with another nucleus touching a grain boundary or triple junction. Due to the three-dimensional nature of the grain boundaries, there could easily have been a boundary running close to the surface at a shallow angle which gave rise to the nucleus. Of all triple junctions in the 7 samples, about 20% had nuclei after the annealing. Vandermeer and Gordon [89] found nucleation at 6% of triple junctions and Sabin et al. [43] found nucleation at more than half of the triple junctions examined. In both cases, the material used was high-purity aluminum which had been deformed 40%. It is believed that the frequency of nucleation may be very sensitive to such factors as grain size and shape, annealing time, texture, triple junction geometry or deformation history.

4.2.1 Parent oriented nuclei

Figure 4.2 shows an example of a nucleus with parent orientation (nucleus C01). This appears to be a nice example of strain-induced boundary migration (SIBM, see section 1.2.2 and compare with figure 1.5 on page 9). The nucleus appeared at a grain boundary and had the crystallographic orientation of one of the parent grains, growing into the other grain. The figure

Nucleus	(ϕ_1, Φ, ϕ_2)	Site	Internal LABs
A01	348 75 352	Triple junction	yes
B03	4 77 350	Grain boundary	no
C01	329 97 31	Grain boundary	no
C08	22 94 333	Grain boundary	no
D05	17 89 16	Triple junction	yes
D09	18 71 18	Triple junction	yes
D10	40 69 16	Triple junction	yes
E01	16 92 324	Triple junction	no
E02	346 94 349	Triple junction	no
F01	227 8 31	Triple junction	yes
F02	215 9 55	Triple junction	yes
F03	200 13 63	Triple junction	yes
G01	309 13 57	Triple junction	no
G02	167 5 11	Triple junction	no

Table 4.2: Type I: Parent-oriented nuclei. "LABs" refers to whether there is an appreciable amount of low-angle grain boundaries ($< 10°$) within the nuclei.

Nucleus	(ϕ_1, Φ, ϕ_2)	Site	Internal LABs
B01	15 84 349	Grain interior	no
B02	353 71 26	Grain interior	no
C05	344 70 357	Grain boundary	no
C06	32 122 3	Grain boundary	no
C07	340 43 359	Grain interior	no
D02	18 53 25	Triple junction	no
D06	319 60 351	Triple junction	no
D07	356 92 19	Triple junction	no

Table 4.3: Type II: Nuclei with new orientations.

Nucleus	(ϕ_1, Φ, ϕ_2)	Site	Internal LABs
C04	20 91 338	Grain boundary	yes
D08	331 79 343	Triple junction	no

Table 4.4: Type III: Nuclei with a twin relationship to parent grains.

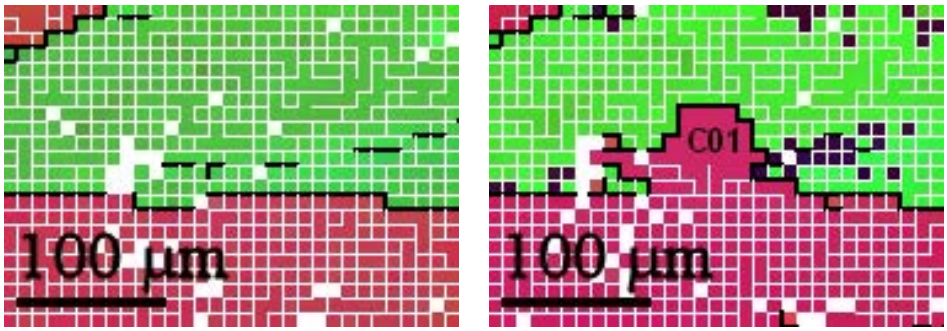

(a) Before annealing.

(b) After annealing at 315° for 15 minutes.

Figure 4.2: Nucleus C01, which is an example of SIBM. White lines represent a misorientation >1° but <10°, while black lines correspond to a misorientation >10°. White points are badly indexed points that have been excluded from the data set based on the double criterion described in section 4.1.2. The darker points in the upper grain are due to the coloring scheme used for coloring the grains according to Euler angles. They are within a few degrees of the green neighboring points as seen by the white lines surrounding them.

shows how the nucleus maintained a low-angle boundary to the grain in the lower half of the image while having a high-angle boundary in the direction of growth. Low-angle boundaries (LABs) are in this case defined as boundaries of misorientation $< 10°$ but $> 1°$ and are drawn as white lines in all the following figures. In the deformed grains, almost all pixels are separated by low-angle boundaries. The deformation microstructure of this type of sample is expected to have misorientations of the order of 1° across cell boundaries and 5° across the extended planar boundaries called GNBs [93]. As the cell size is a few μm, a step size of 10μm means that two neighboring pixels in the deformed matrix will most likely have more than a 1° orientation difference. This makes the recrystallized grains stand out clearly from the deformation structure by having no or only few internal low-angle boundaries. High-angle boundaries (HABs) are defined as boundaries of misorientation $> 10°$ and are drawn as black lines in the EBSP map figures.

Two other examples of parent-oriented nuclei (B03 and D05) can be seen in figures 4.3 and 4.7, where they have appeared in conjunction with other nuclei of new orientations.

The nuclei in table 4.2 have also been categorized by whether they have internal low-angle boundaries (LABs), within the nuclei. Half of the parent-oriented nuclei showed some internal boundaries, while the nuclei with new

orientations in table 4.3 had no appreciable internal misorientations. This corresponds well with the findings of Sabin et al. [43], who also found that about half of the nuclei with low-angle boundaries to the deformed grains retained interior misorientations, while the nuclei which exhibited new orientations did not have this feature. As described in section 1.2.2, this may be due to the dragging of the dislocation structure in the growth of SIBM nuclei.

All the nuclei with parent orientations appeared at triple junctions or grain boundaries. This is reasonable, as nucleation inside a single grain would not give sufficient driving force for the growth of a nucleus with an orientation close to that of the surrounding structure. As is the case for all nuclei, parent oriented nuclei will have the best conditions for growth in the direction of a high-angle boundary, i.e. into a grain of a different orientation.

4.2.2 Nuclei with new orientations

Figures 4.3, 4.4, 4.5, 4.6 and 4.7 show EBSP maps of all of the 8 nuclei of Type II, which have appeared at 5 separate locations. As many nucleation sites had more than one nucleus, nuclei with parent orientations are also apparent in some of these figures.

Figures 4.8, 4.9, 4.10, 4.11 and 4.12 show {111} pole figures of the orientations of the same nuclei as seen in the maps. The first pole figure shows the orientations within the nucleation area of the un-annealed sample. The nucleation area is shown by a dashed line in figure 4.1(a). The second pole figure shows the orientations of the nuclei overlaid on the data from the first figure. This reveals which nuclei have an orientation within the spread of a deformed grain as well as which nuclei have ⟨111⟩ poles in common with any of the parent grains.

The 8 nuclei considered in this section all have relatively high misorientation angles to the deformed grains surrounding them, and their orientations were not observed in the EBSP scans prior to annealing. The critical embryo size, i.e. the minimum size for a nucleus to start growing is of the order of 1μm, as was described in section 1.2, and the step size of the scans ranges from 2 to 10μm. This means that the orientation could have been present in a small area on the surface and still not have been observed. However, a previous study with a smaller step size has shown similar results, finding both parent and new orientations [43]. But even with a smaller step size it cannot be ruled out that the orientation may have been present in a yet smaller volume or a volume below the surface, as EBSP only observes a very shallow depth below the surface.

Generally, only nuclei which were contained fully within the characterized

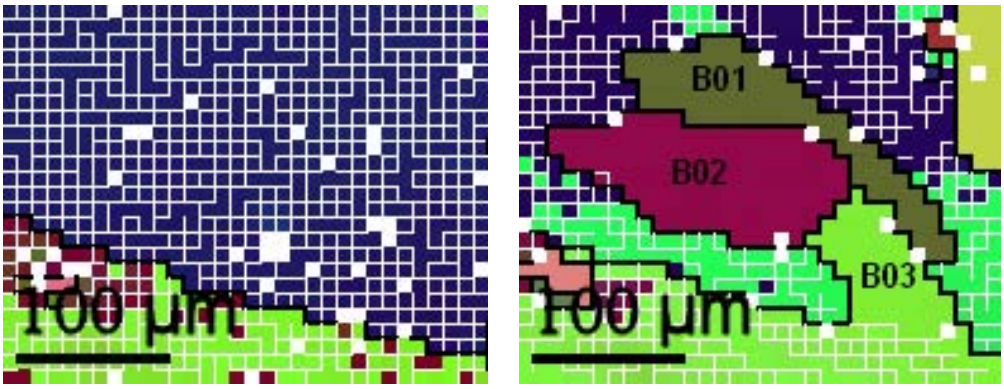

(a) Before annealing. (b) After annealing at 320° for 15 minutes.

Figure 4.3: Nuclei B01, B02 and B03. Nuclei B01 and B02 have new orientations while B03 has an orientation within the spread of a parent grain. The green nucleus to the top right was excluded from the analysis, as it extended outside the area examined.

(a) Before annealing. (b) After annealing at 315° for 15 minutes.

Figure 4.4: Nuclei C05 and C06. These two nuclei have an internal twin relationship. The green nucleus in the bottom of the image has been excluded as it extends outside the area examined. The coloring of the deformed grain to the left has shifted from green to violet between the two characterizations due to a small tilting of the sample. The orientation difference between these is actually only a few degrees.

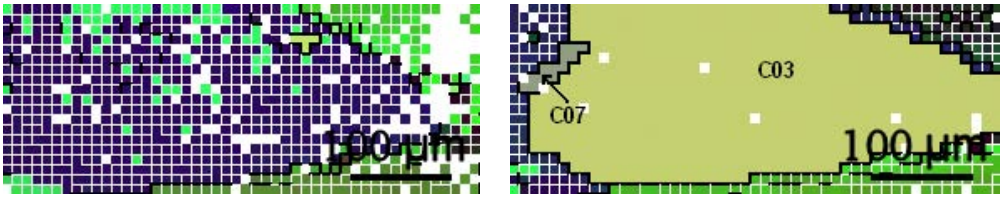

(a) Before annealing. (b) After annealing at 315° for 15 minutes.

Figure 4.5: Nucleus C07. The large nucleus touching C07 is C03, which has been excluded because the orientation was present before annealing in a few pixels.

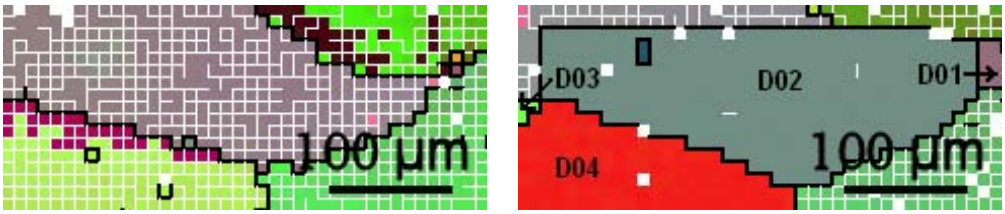

(a) Before annealing. (b) After annealing at 315° for 15 minutes.

Figure 4.6: Nucleus D02. The other nuclei seen in the image have all been excluded because the orientations were present before annealing in a single pixel. The two dark blue pixels inside D02 are most likely misindexed, as they both have only 3 fitted Kikuchi lines. But because they do not each have 4 high-angle boundaries, they do not fall for the criterion for being discarded.

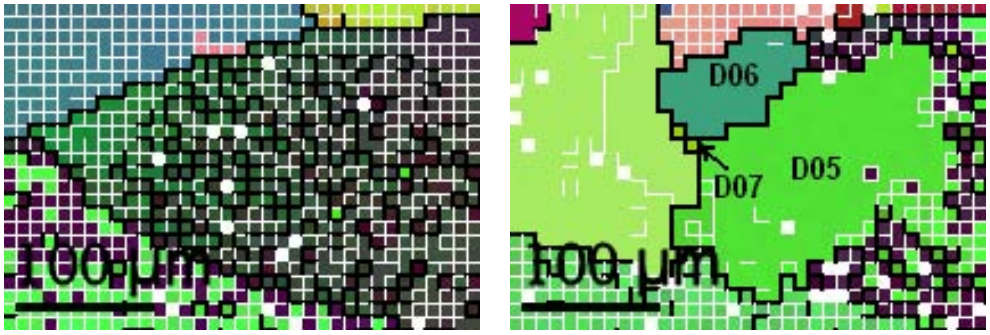

(a) Before annealing. (b) After annealing at 315° for 15 minutes.

Figure 4.7: Nuclei D05, D06 and D07. The nucleus to the left has been excluded because it extends outside the area characterized. The coloring of the two deformed grains in the top of the image have shifted from blue to pink and from light green to red between the two characterizations due to a small tilting of the sample. The orientation difference between these is actually only a few degrees.

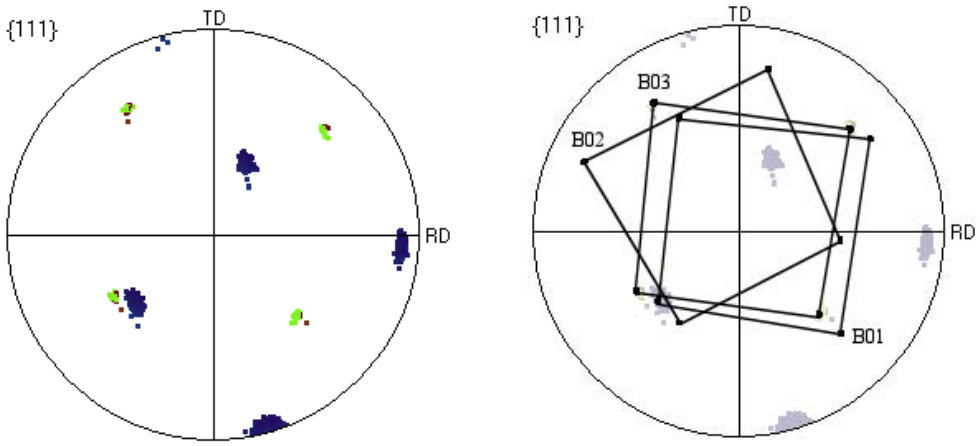

(a) The orientations present in figure 4.3(a)in the area of the nuclei seen after annealing plus an extension of 20 μm.

(b) The orientations of the nuclei B01, B02 and B03 overlaid on the orientations from (a).

Figure 4.8: {111} pole figures of deformed matrix and nuclei B01, B02 and B03.

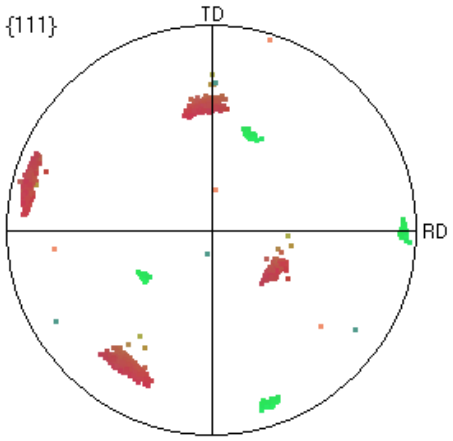

(a) The orientations present in figure 4.4(a) in the area of the nuclei seen after annealing plus an extension of 20 μm.

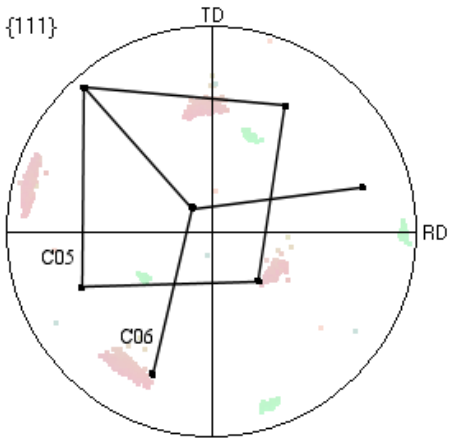

(b) The orientations of the nuclei C05 and C06 overlaid on the orientations from (a).

Figure 4.9: {111} pole figures of deformed matrix and nuclei B01, B02 and B03.

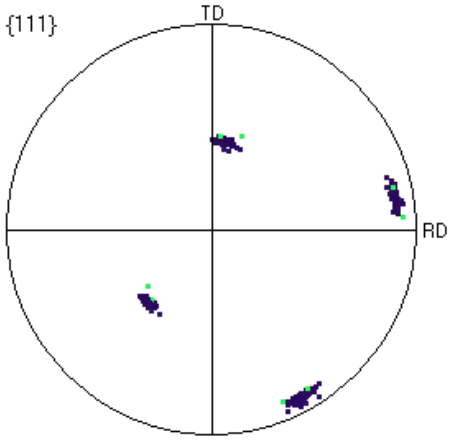

(a) The orientations present in figure 4.5(a) in the area of the nucleus seen after annealing plus an extension of 20 μm.

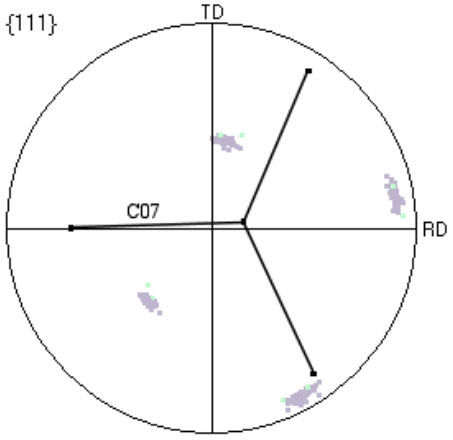

(b) The orientations of the nucleus C07 overlaid on the orientations from (a).

Figure 4.10: {111} pole figures of deformed matrix and nuclei B01, B02 and B03.

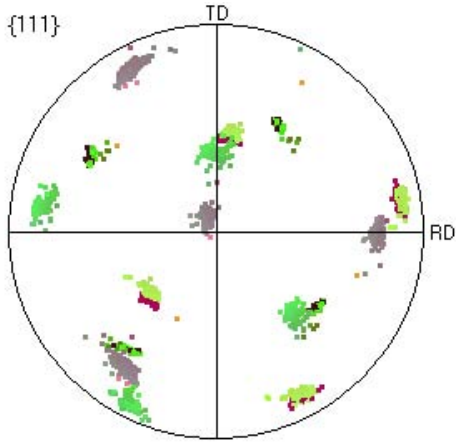

(a) The orientations present in figure 4.6(a) in the area of the nucleus seen after annealing plus an extension of 20 μm.

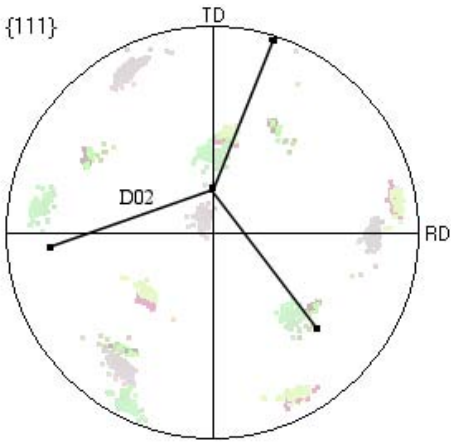

(b) The orientations of the nucleus D02 overlaid on the orientations from (a).

Figure 4.11: {111} pole figures of deformed matrix and nucleus D02.

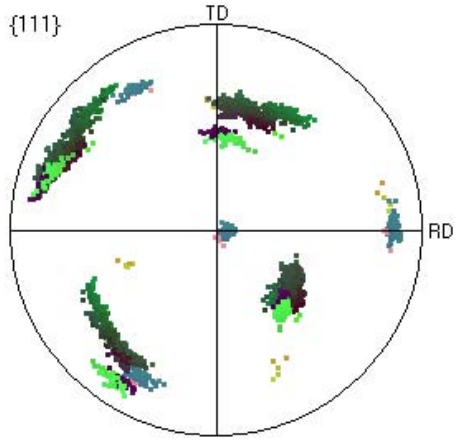

(a) The orientations present in figure 4.7(a) in the area of the nuclei seen after annealing plus an extension of 20 μm.

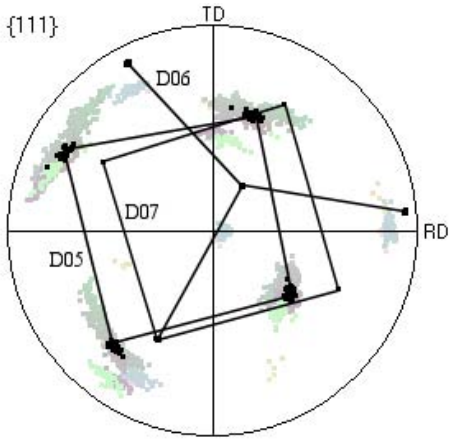

(b) The orientations of three nuclei D05, D06 and D07 overlaid on the orientations from (a).

Figure 4.12: {111} pole figures of deformed matrix and nuclei D05, D06 and D07.

areas were considered. However, although nucleus C06 extended outside this area, it has been included in the study to aid in the understanding of nucleus C05 to which it was twinned. No other nuclei extending outside the characterized area showed a similar twin relation with the nuclei analyzed here.

The relationship between the nuclei of new orientation and the orientations present in the deformed grains seen at the nucleation site before annealing was analyzed to determine if a correlation could be found. This included an analysis of the active slip planes and predictions about the orientations of GNBs and is described in the following.

4.3 Slip plane analysis

Previous studies [38, 43, 46] have shown that new orientations arising during annealing may exhibit a relationship to the deformed structure corresponding to a rotation around a crystallographic axis. The possible mechanisms suggested in the literature were outlined in section 1.3.1.

The mechanism behind the rotations is not understood, but it is likely that it relates to the reordering of the deformation-induced dislocation structure. The following analysis has used the predictions of Winther and Huang [9, 49] about the alignment of GNBs to establish if a correlation between the deformation microstructure aligned with active slip planes and the formation of nuclei with new orientations could be seen. This also goes along the lines of Paul and Driver, who observed rotations around one of the crystallographic directions $\langle 111 \rangle$, $\langle 211 \rangle$ or $\langle 100 \rangle$ and found relations to slip activity [38].

The nuclei found in this study were therefore analyzed to determine if any of these rotation relationships might apply to them. For completeness, possible rotations around $\langle 110 \rangle$ were also examined, as this was also predicted to be a possible plane for GNB alignment by Winther and Huang.

The analysis falls into two parts; first, all rotations which were within 10° of one of the crystallographic axes were found and listed, and then these axes were analyzed to determine if they fit the predictions from slip plane analysis.

4.3.1 Possible rotation axes

The 8 nuclei which appeared with new orientations were all compared to the deformed structure. This was done by comparing the orientations of the nuclei with the orientations present in the deformed structure within the nucleation area. Of all $\langle 111 \rangle$-, $\langle 211 \rangle$-, $\langle 110 \rangle$- and $\langle 100 \rangle$-axes, the ones which

Nucleus	Misorientation axis to deformed state	Misorientation angle	Orientation in deformed state (ϕ_1, Φ, ϕ_2)
B01	[1 1 -1]	36°	27 111 329
B02	[1 2 -1]	44°	26 113 327
	[1 1 -1]	46	30 113 335
C05	[1 -1 2]	31°	334 85 25
	[1 -1 1]	29°	330 87 18
	[1 -1 0]	45°	30 106 328
C06	[1 1 -1]	43°	335 93 33
	[1 2 -1]	44°	337 77 33
	[1 1 -2]	46°	330 91 23
C07	[1 -1 1]	50°	30 102 340
	[2 -1 1]	46°	31 105 331
D02	[1 0 0]	23°	28 74 21
	[-2 1 1]	41°	11 89 7
	[-1 1 1]	44°	335 60 345
D06	[-1 0 1]	20°	320 46 4
	[1 1 2]	52°	16 93 13
	[1 -1 1]	47°	9 108 353
D07	[0 1 0]	27°	22 83 18
	[1 1 -2]	34°	13 105 353
	[-1 0 1]	55°	317 48 3
	[1 1 -1]	27°	13 104 4

Table 4.5: Possible misorientation axes and the orientation at the point in the deformed matrix with the best fit. All axes with a deviation of less than 10° are listed.

showed a possible rotation with less than a 10° deviation from the axis were collected. These can be can be seen in table 4.5 along with the orientation in the point from the un-annealed sample with the smallest deviation from the rotation axis. All types of axes were observed, and for some nuclei there were many rotations possible.

4.3.2 Dislocation boundary alignment

Although many possible rotation axes were observed, only some of these were predicted by analysis of the slip planes. Therefore, the orientation relationships observed between the deformed structure and nuclei of new

orientations were correlated to the crystallographic alignment of dislocation boundaries. This method has been used before to successfully correlate the new orientations observed in nuclei with rotations about the normals to active slip planes [43]. The dislocation boundaries were not observed directly, but newly-established relations [9, 49] allow prediction of this alignment based on the initial orientation of the grains through calculations of the active slip planes [94, 95]. It was assumed that the slip plane activity could be predicted by either the Taylor model or from the Schmid factors which were described in section 1.1.2.

The two main mechanisms for forming GNBs closely aligned to {111} slip planes are single slip and coplanar slip [49]. In single slip where one slip system is activated, boundaries close to the {111} slip planes will form. The boundary alignment will deviate from the ideal slip plane by rotation around the ⟨211⟩ axis perpendicular to the active slip direction. When two slip systems operating in the same slip plane dominate equally, the slip is called coplanar. This will also produce GNBs close to {111}, but the deviation will be around a ⟨110⟩ axis which is the sum of the two ⟨211⟩ axes perpendicular to the active slip directions. The ⟨211⟩ or ⟨110⟩ axis of the deviation of the GNB plane from {111} will be referred to as the "deviation axis".

Another slip class forming boundaries aligned with crystallographic planes is codirectional slip, where slip is activated in the same direction on two different slip systems. The GNB planes will be a linear combination of the two active slip planes weighted with their activities. This means that if the two systems are equally activated, the GNBs will align with either a {110} or a {100} plane depending on the sign of the slip systems [49]. If the systems are not equally activated, boundaries on {211} planes can form.

Other slip system combinations may give rise to other boundary alignments [49]. But these will not be considered here as they are not very common in rolled aluminum and do not apply to any of the grains in the present data set.

In summary, the four possible rotation axes ⟨111⟩, ⟨211⟩, ⟨100⟩ and ⟨110⟩ are chosen because the planes {111}, {211} {100} and {110} are possible GNB planes, and there is a possible deviation from the {111} plane around a ⟨211⟩ or a ⟨110⟩ axis.

An inherent part of any dislocation boundary is the fact that it accommodates a crystallographic misorientation. Observations indicate that the misorientation across a GNB aligned with {111} are of twist character rather than tilt character [93], which corresponds well with the suggestion that new orientations formed by rotation around ⟨111⟩ axes are caused by the movement of screw dislocations [27] as described in section 1.3.1.

4.3.3 Application to data

The possible rotation axes found in the present data were examined to see if they corresponded to the specific axes predicted by the above theory. Table 4.6 shows the subset of the possible rotation axes which agreed with the predictions from slip plane analysis.

Six of the eight nuclei showed a rotation in a {111} plane with a high activity on either one or two slip systems. This means that these rotations occurred around the normal to the expected GNB planes. One of these (B02) also had the possibility of being rotated around the ⟨211⟩ deviation axis, which would fit with the predictions of such rotations occurring in the case of one dominant slip system. In all cases where agreement was found, the match between predicted GNB plane normal and rotation axis was with the specific variant of the ⟨111⟩ axis. Two nuclei did not show any agreement although several possible axes were present.

Both of the two nuclei which could not be explained by slip plane analysis had a boundary to a nucleus with which they were twin related which was predicted to have arisen from {111}-aligned GNBs. This agrees with the scenario of one nucleus forming by a ⟨111⟩ rotation and the other nucleus forming by subsequent twinning from this nucleus.

This appears to reveal a general trend, as all 6 of the nuclei which could not be attributed to twinning were likely to have formed by a rotation around the normal to the slip planes with which the dislocation structure in the deformed material was expected to align.

4.4 Discussion

The experiments described here allowed direct comparison of the orientations before and after annealing to nucleation. As the study utilized a surface method, effects of the free surface could not be discounted.

As was expected from the literature [3, 89], the major part of nucleation occurred at triple junctions, although nucleation at other sites (i.e. grain boundaries and grain interiors) was also seen. Some of these nuclei may however have originated at triple junctions below the surface.

Type II nuclei

The Type II nuclei all had a relatively large misorientation to the parent grains and an orientation that was not observed in the map of the deformed sample (see page 42). As the minimum misorientations were on average 29° to the point in the deformed map with the closest orientations, it is not likely

Nucleus	Misorientation axis / angle to deformed state	Prediction from Schmid factors	Prediction from Taylor model
B01	[1 1 -1] / 36°	GNBs aligned with **(11-1)** & (1-11)	-
B02	[1 1 -1] / 46° [1 2 -1] / 44°	GNBs aligned with **(11-1)**; deviation axis: **[12-1]**	-
C05*	-	-	-
C06*	[1 1 -1] /43°	GNBs aligned with **(11-1)**	GNBs aligned with **(11-1)** & (1-11)
C07	[1 -1 1] / 50°	GNBs aligned with **(1-11)**	GNBs aligned with **(1-11)** & (11-1)
D02	[-1 1 1] / 44°	GNBs aligned with **(-111)**	GNBs aligned with **(-111)** & (131)
D06*	[1 -1 1] / 47°	GNBs aligned with **(1-11)** & (-111)	GNBs aligned with **(1-11)** & (-111)
D07*	-	-	-

Table 4.6: Slip system and GNB analysis. Of the possible rotation axes listed in table 4.5, those that show agreement with one or more of the possible slip system models (Taylor model or Schmid factor) for prediction of the GNBs are listed. The nuclei marked with asterisks in sample C and D are first order twin related to each other. The specific planes and axes listed are either the plane or the deviation axis of the plane with which the GNBs are expected to align. All 8 nuclei of new orientations are listed, and in cases where no correspondence with slip plane predictions is found, a "-" is shown in the table.

that a cell of the nucleus orientation may have arisen during deformation. The deformed structure of 30% rolled aluminum has been observed to have a structure consisting of GNBs and cell boundaries. Liu et al [93] observed the misorientations across GNBs to be of the order og 5° and alternating in sign between neighboring boundaries. The cell size was a few micrometres and the IDBs (see section 1.1.2) had misorientations of about 1°. The material of the present study was not observed to have large orientation gradients over the grains in the plane examined, and previous studies [43] indicate that such gradients are also not likely to exist in a direction perpendicular to the surface. Another possibility of explaining the new orientations could be that they had arisen during the mechanical preparation of the surface by local deformations. However, scratches would be expected to give rise to a more random selection of orientations than what was observed here.

Of the 8 Type II nuclei, 6 could be explained by a $\langle 111 \rangle$ rotation of 36-50° around the normal of a slip plane aligned GNB. This rotation corresponds well with the orientations expected to give the highest growth rate of the nuclei [96, 97]. The remaining 2 nuclei were explained by a subsequent twinning from the $\langle 111 \rangle$-rotated nuclei. What the exact nature of the $\langle 111 \rangle$-rotation was, may be discussed. One possibility is a rotation in the plane of the GNB. However, these GNBs often have twist character [93], meaning that the misorientation across the GNB was in the form of a rotation around the slip plane normal. This indicates the possibility that it is not the presence of the GNB itself in the slip plane but rather the high density of dislocations with a burgers vector in the slip plane that facilitates this rotation. This distinction cannot be made for GNBs of twist character, but only for boundaries of tilt character.

Frequency of slip plane aligned GNBs

Both the triple junctions giving rise to parent-oriented nuclei and some of the triple junctions not giving any nucleation in the annealing time were also examined. In both of these cases, about half of the triple junctions had a grain present which was expected to give rise to a GNB aligned with $\{111\}$ through high activity of one or two slip systems in the plane. Although not conclusive, this seems to indicate that a high concentration of dislocations in the $\{111\}$ plane promotes the formation of nuclei of new orientations by a rotation in the plane. However, the presence of dislocation boundaries aligned with the slip plane does not guarantee the formation of such new orientations. If the sample was annealed further, more of these triple junctions might give rise to nuclei. But as the nuclei grow quite rapidly, the triple junctions could also be consumed by nuclei originating elsewhere before this could happen.

The fact that in general only half of the triple junctions had {111} aligned GNBs, while all the nuclei of new orientations originated in a grain with such boundaries shows that these GNBs are not so common that one may always find a match for any grain.

Boundary effects

The deformation mode and thus also the slip systems activated was expected to be affected by the presence of triple junctions. In the present study, the weak deformation of 30% was not expected to induce major differences in deformation mode close to boundaries and triple junctions, but these sites would generally have a higher stored energy favorable for nucleation. Observations have shown that a higher stored energy and a different morphology of the dislocation structure are often observed close to triple junctions [98, 99], although the maximum misorientation is likely to be some distance away. As was seen in table 4.3, only a few of the nuclei observed to have new orientations actually appeared at triple junctions, and several appeared in grain interiors. Although the statistics do not allow a final conclusion, this may indicate that new orientations are more prone to appear some distance away from triple junctions.

Chapter 5

3DXRD - The Experiment

This chapter describes an experiment performed using the three-dimensional X-ray diffraction (3DXRD) microscope on a sample similar to those used in the EBSP experiments described in chapter 4. The aim of the experiment was to observe nuclei in the bulk with a special focus on new orientations, and correlate these orientations to the orientations present at the nucleation site before nucleation.

The 3DXRD method was described in section 2.3. The method is ideal for finding nuclei of new orientations because these will give rise to small point-like diffraction spots situated away from the extended diffraction spots caused by the orientation spread of the deformed parent grains. On the other hand, nuclei appearing with orientations within the orientation spread of the parent grains are likely to be overlooked, as their diffraction spots will overlap with the diffraction spots from the parents.

This experiment supplemented the EBSP experiments by probing the bulk of the material and mapping the same volume inside the sample before and after annealing to nucleation. Where the surface experiments could not conclusively say that new orientations seen had not originated from below the surface, the 3DXRD experiment mapped the entire cross section of the sample and thus eliminated this problem.

The sequence of the experiment was as follows:

- A sample was prepared from the 30% deformed starting material with a rectangular cross-section and the largest faces in the RD-ND plane.
- The largest faces were characterized by EBSP.
- The sample was mounted in the furnace and the gauge volume was mapped by 3DXRD. The mapping consisted of 97 layers with a layer spacing of 7 μm.

- The sample was annealed for 2 minutes at 320° C.
- The same gauge volume was mapped again by 3DXRD.
- The surfaces were characterized again by EBSP.

5.1 Experimental

5.1.1 3DXRD setup

The setup used for the 3DXRD experiment was described in section 2.3 and can be seen in figure 2.4. The furnace was situated in the beam during the entire experiment with the quartz tube in place. The Frelon4M and Quantix detectors were used simultaneously and will be referred to as far-field and near-field detector respectively in the following.

The sample was prepared from the material described in chapter 3 and had a cross section of 1000×600 μm^2. The largest faces were mechanically and electrochemically polished, while the smaller faces had been spark cut before electropolishing. Figure 5.1 shows the sample dimensions.

The X-ray beam had an energy of 46.84 keV. After initial calibrations, the beam configuration was constant for the entire experiment. The beam was focused vertically to a height of 7 μm using a bent Laue crystal. Some tails on the beam were unavoidable. Horizontally, the beam was unfocussed and slit to a width of 1500 μm. This means that the beam was wide enough to illuminate the entire cross section of the sample at any rotation angle.

5.1.2 3DXRD experimental procedure

For the 3DXRD experiment, the sample was mounted in the furnace with RD in the z direction. The sample was not aligned with the x and y axes, and the orientation was found after the experiment to be TD at a 37° angle to x. This was taken into account in the data analysis by a rotation matrix bringing measured orientations into the rolling coordinate system.

Each layer in the gauge volume was probed by taking 360 images with 1 second exposure for different ω rotations of the sample. The images were taken in 0.25° steps over two separate ω ranges of [-22.5°; 22.5°] and [67.5°; 112.5°] to ensure that sufficient diffraction spots were recorded to make a good determination of the crystallographic orientations. As these intervals were perpendicular to each other, they would also give optimal conditions for fitting the positions of the nuclei. The layers were spaced by 7 μm in the RD direction (see figure 5.1), giving a continuous coverage of the entire gauge

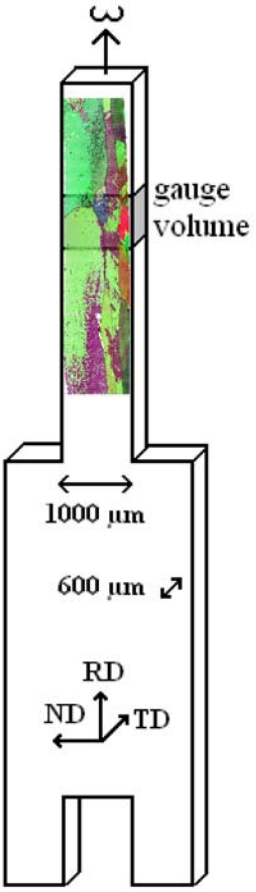

Figure 5.1: X-ray sample geometry. The EBSP map of one of the surfaces is shown. The lower part of the sample is for mounting in the furnace.

volume. 97 consecutive layers were mapped, starting from layer 0 in the top and proceeding in the $-z$ ($-$RD) direction, giving a height of close to 700 μm. After every 6th layer, the sample stage was returned to a reference position and a small scan was performed in order to detect any drift of the sample position during the scan. The drift during the experiment was estimated to be of the order of one layer and was taken into account in the data analysis. The whole mapping took about 54 hours.

For the annealing, the temperature in the furnace was increased from room temperature to 320° C over a 10 minute period and then held stable at this temperature for two minutes. After this, the furnace and sample were allowed to cool with an initial cooling rate of about 25 K/minute. After the annealing, a short scan revealed that nucleation had taken place, and therefore the same gauge volume as before annealing was mapped again to be able to make a direct comparison of the microstructure before and after nucleation of recrystallization.

5.1.3 EBSP experimental procedure

The two largest surfaces of the sample were scanned by EBSP before and after the experiment. The scans were performed with a Zeiss Supra FEGSEM with a step size of 5-10 μm.

The EBSP mappings were done at Risø before and after the X-ray experiment.

5.1.4 3DXRD feasibility study

Another experiment was performed before this one to test the feasibility of this type of nucleation study. This previous experiment, which is described in appendix B, was performed in July 2006. The former beamline setup at ID-11 was therefore used. The experiment described in this chapter was performed in April 2008 using the present setup with a longer distance between optics and experimental hutches (see section 2.3.2). The feasibility study determined the orientations of two nuclei which had grown quite large, and diffraction spots indicated that more were likely to be present. It was concluded that a smaller step size in the rotation would improve the orientation indexing of the nuclei, and that a complete mapping of the same volume before and after was preferable. In the feasibility study, much effort was put into finding triple junction regions before annealing and making selected volume maps around them. A complete map might take a slightly longer time, but would make the comparison of data before and after annealing much more straight-forward and reliable.

These improvements along with others due to general upgrades of hardware and software were implemented in the experiment described in the following.

The major differences between the main experiment and the feasibility study were:

- A wider beam was used. As the entire cross section of the sample should be in the beam during the mapping, a wider beam meant that a larger sample thickness could be used. This strengthened the case for measurements taken inside the sample being true of the bulk.
- A larger number of layers were also covered, resulting in a significantly larger gauge volume.
- The same volume was mapped before and after annealing, allowing a direct image-by-image comparison to observe changes in the microstructure such as new orientations appearing.
- A smaller ω step in the rotation allowed a more precise indexing of the orientations of nuclei which typically have a low mosaicity.
- In the feasibility study, pixels on the far-field detector were binned so that the intensity in 2×2 pixels were counted as one pixel. This reduced the noise level, giving a lower detection limit but also degraded the spatial resolution. In the present experiment, no binning was used, as the spatial information in the far-field detector data was also needed.
- The furnace quartz tube was kept in place during the entire experiment. This gave more diffuse scattering but allowed precise measurements of the same volumes before and after annealing without risking sample misalignment. The gauge volume position was found again after the annealing using the top of the sample as a reference.
- Both experiments used both the near-field and far-field detectors, but in the experiment described in this chapter, the two detectors were used simultaneously. Although the far-field detector gave precise information on the crystallographic orientations, the spatial resolution of this detector was significantly smaller than that of the near-field detector, meaning that the two detectors supplemented each other nicely. Having two detectors at the same time not only saved time but also gave the added advantage of having precisely comparable data from the two detectors, as no problems of drift or misalignment were present when the two detectors recorded their images at exactly the same time.

5.2 Near-field data

The efficiency of the 3DXRD near-field detector was about an order of magnitude less than the efficiency of the far-field detector. The lower efficiency of the near-field detector meant that the signal-to-noise ratio for the near-field detector was significantly worse, giving only clear diffraction spots from the largest grains, as illustrated in figure 5.2(d). The exposure time was set to 1 second per image in order to obtain the highest possible amount of information on the far-field detector within the experimental time. However, this meant that many of the smaller diffraction spots seen on the-far-field detector were not detected by the near-field detector. Using attenuation of the far-field detector might have improved this situation, but would have required a much longer exposure time per image.

So while the near-field detector had a higher spatial resolution due to the smaller pixel size, many smaller volumes were missing from the data obtained on this detector. The nuclei observed were thus all found from the far-field detector data. It was decided to abandon the data analysis from the near-field detector, as the far-field data had a sufficient spatial resolution and a significantly higher completeness.

5.3 Image processing

The 3DXRD images recorded on the CCDs are subject to various types of noise. This includes scattering from the optical setup and other elements, but also internal electronic noise in the CCD.

A standard way of background correction involves the subtraction of two images; a background image and a dark-field image. The background image is recorded without the sample present while the dark-field image is an image recorded without X-ray exposure. Both of these are recorded using the same exposure time as the diffraction images. The dark-field image removes the internal electronic noise and is subtracted from both diffraction image and background image before the background is subtracted from the diffraction image.

However, in the present case, the furnace tube gave rise to amorphous scattering during the experiment. This scattering was highly dependent on the presence and angular rotation of the sample, so a background image recorded without the sample would not have given a sufficient correction [100]. A median method was therefore used. This was done by calculating the median of all 360 diffraction images in each layer and subtracting this from the images. The median image was produced by assigning the median

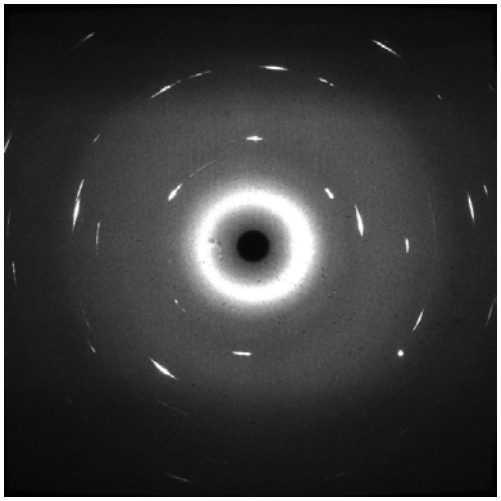

(a) Raw far-field detector image.

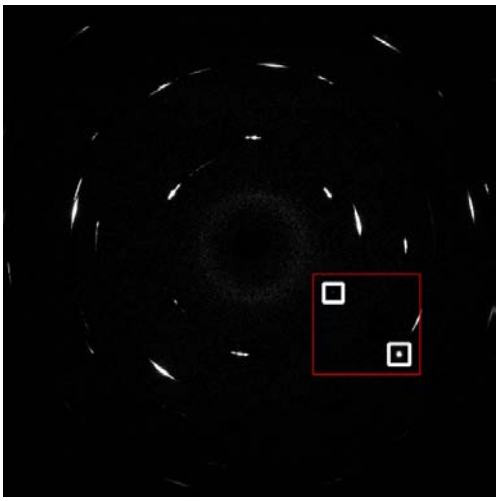

(b) Far-field detector image with the median image subtracted and corrected for spatial distortion.

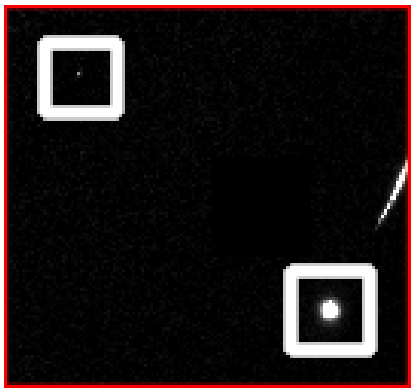

(c) Enlargement of the area marked in red in (b).

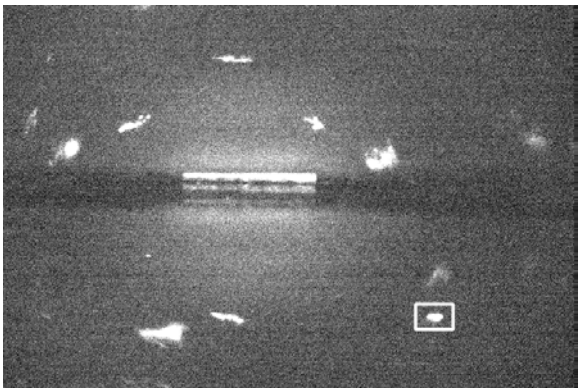

(d) Raw near-field detector image recorded simultaneously with the far-field detector images.

Figure 5.2: 3DXRD detector images showing both deformed and recrystallized material. Two diffraction spots from two different crystallites are marked in the far-field detector images. Only the largest of these spots is visible in the near-field detector image. The shape of the diffraction spots on the far-field detector represents only the orientations present, giving circular spots for recrystallized nuclei. On the the near-field detector, the shape of the diffracting crystal also affects the shape of the diffraction spots.

value at a given pixel position to this pixel. Calculating a new median image for each layer accounted for any changes in synchrotron current affecting the intensity of the X-ray beam. Using a median image also meant that no dark-field image needed to be subtracted.

Another correction necessary was the application of a spline function, which accounts for fact that the optical elements in the detector are not perfect, e.g. the flourescent screen may not be perfectly flat. This correction was done using the program Fit2D [101]. Figure 5.2 show a far-field image before and after median subtraction and spline correction. Ideally, images should also be corrected for the flat field given by different sensitivity in each pixel in the CCD. However, the correction factor was close to 1, giving a negligible error. Hence no flat-field correction was applied.

5.4 Detection limit

As the aim of this experiment was to discover nuclei of new orientations while they were still quite small, it was important to know the size of the smallest possible volume element that could be detected. This will be called the detection limit and was found by scanning a gold foil with a random texture and a thickness of 100 μm over a rotation ω from -45° to 45° in 91 steps of 1 second and recording images using the same setup on the same two detectors as used for the main experiment. This foil will be referred to as the powder sample. As the far-field detector had the highest efficiency, the detection limit discussed in the following will refer to this detector.

To find the detection limit, the integrated intensity, $\mathfrak{I}$, from this known gauge volume can be compared with the intensity of the smallest detectable spot on the detector as described in the following. The integrated intensity is equal to the total energy striking the detector. Although the measured intensity is only a fraction of this given by the efficiency of the detector and the attenuation, a comparison of the magnitude of the two intensities will be unaffected by the efficiency. This requires that no pixels on the detector reach saturation, as the total intensity measured will then be lower than expected from the total intensity diffracted.

5.4.1 Diffraction background

X-ray diffraction theory states that the total energy diffracted from a single crystal when it is rotated at a velocity $d\omega$ through a single Bragg reflection

is given by [102]:

$$\mathfrak{I}_{\text{crystal}} = \frac{1}{d\omega} \cdot I_0 \Big(\frac{e^2}{m_e c^2}\Big)^2 \cdot \frac{\lambda^3 V_c |F_{hkl,c}|^2}{v_c^2} \cdot P \cdot L. \tag{5.1}$$

I_0 is the total intensity of the incoming beam and the constant $(\frac{e^2}{m_e c^2})^2$ is called the Thomson scattering length. λ is the wavelength of the incoming X-rays, V_c is the volume of the crystal, $F_{khl,c}$ is the structure factor of a reflection with Miller indices (h, k, l) and v_c is the volume of the unit cell in the material. The final two factors, P and L are the polarization factor and the Lorentz factor, which depend on the diffraction angles. For the monochomatized synchrotron X-ray setup used here, L=$1/[\sin(2\theta_c)|\sin(\eta_c)|]$ [81], where the angles θ and η are defined in figure 2.4, and the subscript c refers to the material of the crystal. The polarization factor is close to 1 for high-energy X-rays and will not affect the calculation of the volume significantly, so it will be set to 1 for simplicity.

For a powder sample of random texture, the total scattered energy in an entire Debye-Scherrer ring can be obtained through integration over all angles and is given by [102, 103]:

$$\mathfrak{I}_{\text{powder}} = t \cdot I_0 \Big(\frac{e^2}{m_e c^2}\Big)^2 \cdot \frac{\lambda^3 V_p |F_{hkl,p}|^2 m_{hkl}}{4 v_p^2} \cdot \frac{P}{\sin(\theta_p)}. \tag{5.2}$$

Again, the polarization factor will be set to 1, and t is the exposure time. Note that the multiplicity m_{hkl} of the hkl reflection has been included in the expression as the total intensity is the sum of all reflections on the ring. As a different material (gold) was used for the calibration, the structure factors, unit cell volume and diffraction angle will be different in the calculation of the intensity of the powder sample, and the subscript p will be used for these.

Taking the ratio between $\mathfrak{I}_{\text{crystal}}$ and $\mathfrak{I}_{\text{powder}}$ allows us to isolate the volume of the crystal and eliminate the incoming intensity I_0:

$$\frac{\mathfrak{I}_{\text{crystal}}}{\mathfrak{I}_{\text{powder}}} = \frac{1}{d\omega t} \frac{V_c}{V_p} \frac{|F_{hkl,c}|^2}{|F_{hkl,p}|^2} \Big(\frac{v_p}{v_c}\Big)^2 \frac{1}{m_{hkl}} \frac{4\sin(\theta_p)}{\sin(2\theta_c)|sin(\eta_c)|}. \tag{5.3}$$

In an experiment, the measured diffracted intensity will be reduced due to attenuation in the sample and foil, called self-attenuation. The intensities therefore have to be divided by the attenuation factor given by $e^{(-\frac{\mu}{\rho}x)}$, where x is the material thickness and $\frac{\mu}{\rho}$ is called the mass attenuation coefficient and is tabulated for various materials. The mass attenuation coefficient depends on the wavelength of the X-rays as well as the material. Let $\mathfrak{I}_{\text{c,m}}$ and $\mathfrak{I}_{\text{p,m}}$

represent the measured intensities from a crystal and powder respectively. The volume of the crystal will then by given by:

$$V_c = \frac{\mathfrak{I}_{\mathrm{c,m}}}{\mathfrak{I}_{\mathrm{p,m}}} \frac{e^{((-\frac{\mu}{\rho})_p x_p)}}{e^{((-\frac{\mu}{\rho})_c x_c)}} \cdot td\omega V_p \cdot \frac{|F_{hkl,p}|^2}{|F_{hkl,c}|^2} \left(\frac{a_c}{a_p}\right)^6 m_{hkl} \cdot \frac{\sin(2\theta_c)|\sin(\eta_c)|}{4\sin(\theta_p)}, \quad (5.4)$$

where the unit cell volume $v = a^3$ has been inserted. The numbers input into this equation are listed in table 5.1 and will be explained in the following.

5.4.2 Experimental calculation of detection limit

The detection limit is defined as the volume of the smallest possible single crystal giving rise to a detectable diffraction spot. The smallest detectable diffraction spot was estimated to have an integrated intensity of 200 counts on a background-corrected far-field image. Setting $\mathfrak{I}_{\mathrm{crystal}}$ to this value then gives the smallest detectable volume.

The total measured energy from diffraction of the gold foil in the three inner Debye-Scherrer rings was found from the average of 91 images. This average image is seen in figure 2.2(a) on page 19. The average intensity in a ring just inside and just outside the diffraction ring was used as a background and subtracted to obtain the actual intensity. Three identical scans were performed with different thicknesses of attenuating aluminum plate in front of the beam. The percentage of the intensity penetrating the attenuation layers was found using a 1-dimensional detector (diode) to be 11, 19 and 33% respectively for the three scans. For the sample mapping, the attenuating layers were removed completely. As a few diffraction peaks were saturated on the detector in the powder scan, the total measured intensity of the powder rings was found for all three levels of attenuation and corrected for this attenuation to obtain comparable numbers. Only minor differences were found in the corrected intensities, indicating that the volume of material giving rise to saturated diffraction spots was negligible. The intensities listed in table 5.1 are the measured intensities for the scan with 11% penetration multiplied by the correction factor 1/0.11 to give the expected measured intensity without attenuation.

The attenuation coefficients used to calculate the self-attenuation were found using the application XOP (X-ray Oriented Programs), which is available at the ESRF homepage [104].

The values of θ were calculated from the X-ray wavelength $\lambda = 0.2647$Å using equation 2.3. The value of $|\sin(\eta)|$ giving the smallest diffracted intensity, i.e. 90° was inserted, as this gives the "worst-case" detection limit.

hkl	111	200	220
$\mathfrak{I}_{\mathrm{Al,m}}$ / counts	200	200	200
$\mathfrak{I}_{\mathrm{Au,m}}$ / 10^6 counts	68.5	29.3	21.6
$(\frac{\mu}{\rho})_{\mathrm{Au}}$	$1.6661{\cdot}10^{-2}$	$1.6661{\cdot}10^{-2}$	$1.6661{\cdot}10^{-2}$
$(\frac{\mu}{\rho})_{\mathrm{Al}}$	$1.12015{\cdot}10^{-4}$	$1.12015{\cdot}10^{-4}$	$1.12015{\cdot}10^{-4}$
t / s	1	1	1
$d\omega$ / s^{-1}	$0.25 \cdot \frac{2\pi}{360}$	$0.25 \cdot \frac{2\pi}{360}$	$0.25 \cdot \frac{2\pi}{360}$
V_p / $\mu\mathrm{m}^3$	$100 \cdot 1500 \cdot 7$	$100 \cdot 1500 \cdot 7$	$100 \cdot 1500 \cdot 7$
$\lvert F_{hkl,Au}\rvert^2$	47062	41715	28028
$\lvert F_{hkl,Al}\rvert^2$	942	819	526
$a_s = a_{Al}$ / Å	4.05	4.05	4.05
$a_p = a_{Au}$ / Å	4.07	4.07	4.07
m	8	6	12
θ_s / °	3.245	3.747	5.303
θ_p / °	3.229	3.729	5.277
ECD / μm	1.0	1.2	1.7

Table 5.1: Values input into equation 5.4. The resulting detection limit is given by the equivalent circle diameter ECD.

The unit cell size a was very similar for the two metals; 4.05Å for aluminum and 4.07Å for gold, also giving similar angles of diffraction from equation 2.3. The structure factors were found using the module `xfab.structure` written by H. O. Sørensen and available through Fable [85].

The equivalent circle diameter or ECD of a sphere with this smallest detectable volume is found by:

$$ECD = 2 \cdot \left(\frac{3}{4\pi} V_c\right)^{1/3} \tag{5.5}$$

As can be seen in the bottom line of table 5.1, the detection limit was found to be of the order of 1-2 μm, increasing with increasing diffraction angle θ, as would be expected because the intensity of diffraction spots decreases with θ. This is of the same order of magnitude as the critical embryo size for nucleation. Note that the detection limit used here is the diameter, not the radius.

5.4.3 Discussion of detection limit

This was the optimal detection limit available for the present setup, ω step size and material. The very large deformed grains in the material caused

diffraction spots close to or above the saturation threshold of the Frelon detector. This detector had the highest efficiency and dynamic range (see section 2.3.3) of the two detectors used. Although a longer exposure time would have given more detail in the near-field data, the detection limit could never be better using this detector due to the smaller dynamic range. Also, a longer exposure time would have meant that a smaller volume could be mapped within the available beamtime, decreasing the chance of observing nucleation events, which are rare. The large size difference between the deformed grains and the smallest nuclei combined with the dynamic range of the detector was the limiting factor concerning the detection limit.

A smaller step size in the ω rotations could have given a better detection limit by avoiding saturation of the detectors from the deformed grains. Focusing the beam to a narrower height in z would also circumvent the saturation problem. However, both of these changes would require a much longer time to continuously cover the same volume, meaning that effectively a smaller volume could be mapped. Another possibility for improving the detection limit is binning of the pixels e.g. 2×2 as mentioned in section 5.1.2. This reduces the noise level and was used in the feasibility study described in appendix B, but was avoided in the present experiment as it also reduces the spatial resolution considerably.

Chapter 6

3DXRD Experiment - Results

In this chapter, the results from the experiment described in chapter 5 will be presented and analyzed within the context of slip-based models.

First, the data analysis process required to find the recrystallized nuclei will be detailed along with the resulting nuclei found.

Then, a description of the entire gauge volume in the deformed as well as the partially recrystallized states will be presented. A map was reconstructed of a partially recrystallized layer and an un-annealed layer, giving the positions and orientations of volume elements. The orientations will first be presented, validated and compared with surface results by using pole figures. Then the spatial maps will be presented.

An analysis correlating the orientations of the nuclei to the orientations in the deformed material is carried out in a manner similar to what was done for the surface experiments in chapter 4.

6.1 Identification of nuclei

The images recorded before and after annealing were examined to discover the appearance of new diffraction spots in order to identify possible nuclei of new orientations.

In contrast to the large deformed grains in the sample, recrystallized nuclei will have a very specific signature on the detector. The far-field detector is most ideally suited for making this distinction, as the large sample-detector distance ensures that the diffraction spots all fall on narrow Debye-Scherrer rings. Each ring corresponds to a set of diffracting planes d in the crystal fulfilling the Bragg condition (equation 2.1). The azimuthal angle η (see figure 2.4) of the diffraction spot on the ring depends on the orientation of the diffracting grains. A large internal orientation spread in a deformed grain

means that the Bragg condition will be fulfilled for many neighboring η as well as many neighboring rotations of the sample (ω). Because of this, the diffraction spots of the deformed structure will usually spread over a large angle of the rings as well as appear in many consecutive images. The diffraction spots caused by the nuclei, however, will appear only in one or two consecutive images and will be spot-like and circular in shape on the far-field detector.

6.1.1 Finding the undeformed crystallites

The recrystallized nuclei of new orientations which were the focus of this study were formed during annealing. However, small perfect crystallites with orientations different from the large deformed grains could also be present before annealing, as was seen in the EBSP study in chapter 4. To differentiate these from the nuclei of interest, the term crystallites will be used in the following to cover all small undeformed crystals, while nuclei will only be used for those appearing after annealing. In the EBSP study, crystallites of new orientations may have arisen due to deformations of the surface during the polishing. The sample used for the 3DXRD study described here was mechanically polished on two surfaces, and a few undeformed crystallites were found on these surfaces. The remaining two surfaces were prepared by spark cutting to avoid deformation during the processing. This was seen not to be an improvement, as even more crystallites were observed on particularly one of these surfaces, possibly arising from heating of the sample during the spark cutting process. The method by which all undeformed crystallites of orientations different from the deformed grains were found is described below.

The set of corrected images was processed using the peaksearch algorithm described in section 2.3.5 with a threshold of 150 counts, as the noise level was of this order. All spots with a spread on the detector less than 2.5σ in y and z and less than 1.2σ in ω were selected in order to separate the diffraction spots from the undeformed crystallites from the diffraction caused by the deformed material. Here σ is the standard deviation of a fitted Gaussian. Although the diffraction spots from perfect crystallites were expected to have a spread close to 1 in y and z as well as in ω, the somewhat larger values in these cases were selected to include as many spots as possible, even if they were not completely spot-like, either due to intensity overflow, grain shape or minor spot overlaps. To minimize the noise, spots comprising 5 pixels or less were excluded. The resulting spots were input into the polycrystalline indexing software GrainSpotter described in section 2.3.5, which identifies orientations of the grains and their positions based on the position of their diffraction spots.

The diffraction spots from the resulting grains were examined manually to exclude false positives, which could for instance be spots from recovery of the deformed structure, which would typically appear as clusters of several spots close together and still connected to spots from deformed grains. This method might exclude some nuclei with an orientation close to the orientations of the deformed grains, but as the focus of this study was to find new orientations, this was not considered a problem. Finally, the orientations of the same crystallites found in consecutive layers were matched to determine their extent in z and to count the number of different crystallites. A total of 50 undeformed crystallites with orientations different from that of the deformed structure were found by this method. A 3D map of their positions is rendered in figure 6.1. The uncertainty on the positions is ideally about 10 μm, but saturation of some of the diffraction spots might give larger uncertainties.

6.1.2 Nuclei selection

As described above, the GrainSpotter software found both the crystallographic orientation and the center-of-mass position of each of the 50 undeformed crystallites. As can be seen in figure 6.1, most of these appear to be located at particularly one of the two smallest surfaces of the sample. These two surfaces were spark cut, while the other two faces were mechanically polished. All faces had been electrochemically polished in the end. As data of the exact same volume had also been acquired before the annealing, the images were compared to find out if any of the diffraction spots were present before the annealing. Several of the crystallites showed diffraction spots present before annealing, although these were usually smaller and present in fewer layers, indicating that the crystallites had grown during the annealing. The diffraction spots of the crystallites before annealing were also very sharp with almost no spread on the detector or on neighboring images. This means that these were technically nuclei but were already present in the deformed material. 27 of the 35 crystallites that were present before the annealing were situated on one of the spark cut surfaces. The remaining 8 were either on or close to the mechanically polished surfaces or the other of the spark cut surfaces. The positions plotted in figure 6.1 are the center-of-mass positions after annealing, where the crystallites may have grown into the sample. Therefore, the positions do not necessarily fall directly on the surface. Positions falling outside the sample are caused by uncertainty on the center-of-mass calculation, mostly due to saturation of some of the diffraction spots. It appears that the spark cutting process initiated nucleation on at least one of the spark cut surfaces even before the annealing started. These

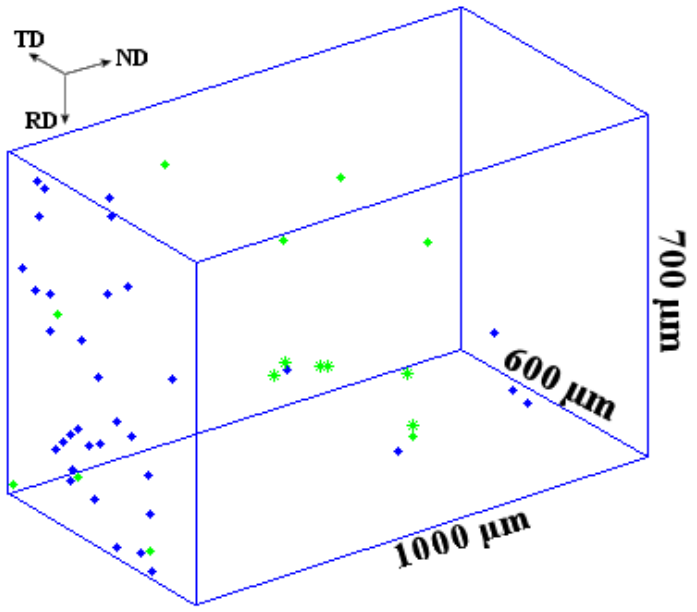

(a) Side view.

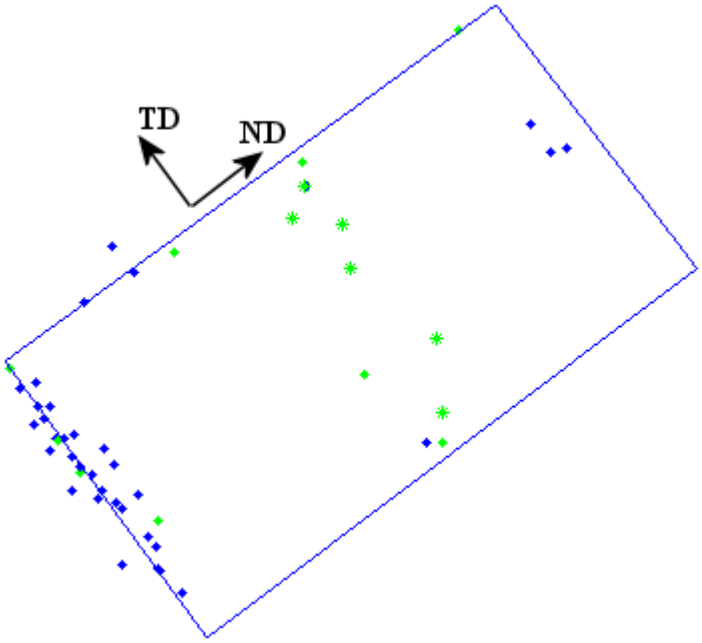

(b) Top view.

Figure 6.1: Center-of-mass positions of the 50 undeformed crystallites found with orientations different from the deformed grains. Blue crystallites were present also before annealing, while green nuclei appeared only after the heat treatment. The 6 nuclei which were both new and more than 30 μm away from the surfaces are marked as stars, while the rest are marked as diamonds. The outline of the gauge volume is marked with blue lines.

crystallites were therefore not useful for the analysis, and were disregarded. To discount all surface effects, all crystallites within 30 μm of both spark cut and mechanically polished surfaces were removed from the data set, along with any crystallites extending outside the characterized gauge volume. The nuclei appearing close to the surface after annealing were also valid and could be subjected to the same analysis as was done with the EBSP experiment in chapter 4, but the focus of this experiment was bulk nucleation, so they were not analyzed further.

The remaining 6 nuclei with new orientations had all nucleated away from any surfaces. The diffraction images before annealing were examined closely to ensure that no material existed before annealing with the orientation of these nuclei to ensure that these were indeed nuclei of new orientations. They were all compared with the nuclei seen on the surface by EBSP, and they were neither identical to these nor twin related to them. Table 6.1 lists these nuclei and the layers in which they were observed. It was observed that for the two largest nuclei, the diffraction spots were present with a low intensity in several layers both above and below what appeared to be the main body of the nucleus. This was due to low-intensity tails on the beam in the z direction.

Nucleus	Layers	L_z / μm	L_{xy} / μm
1	16-18	21	13
2	20-30 (15-32)	77	56
3	17	≤ 7	6
4	19-20	14	10
5	22-30 (19-31)	63	41
6	31	≤ 7	7

Table 6.1: The 6 nuclei of new orientations which were not nucleated at surfaces nor extended outside the examined volume. Their approximate extent in z, L_z is estimated from the number of layers in which they were observed. The two largest nuclei actually had diffraction spots in several layers above and below the layers where they were present due to tails on the beam (numbers in parenthesis). The extent in the xy-plane is given as the diameter of a disc as calculated in section 6.1.3, and relates to the section where the diameter is largest.

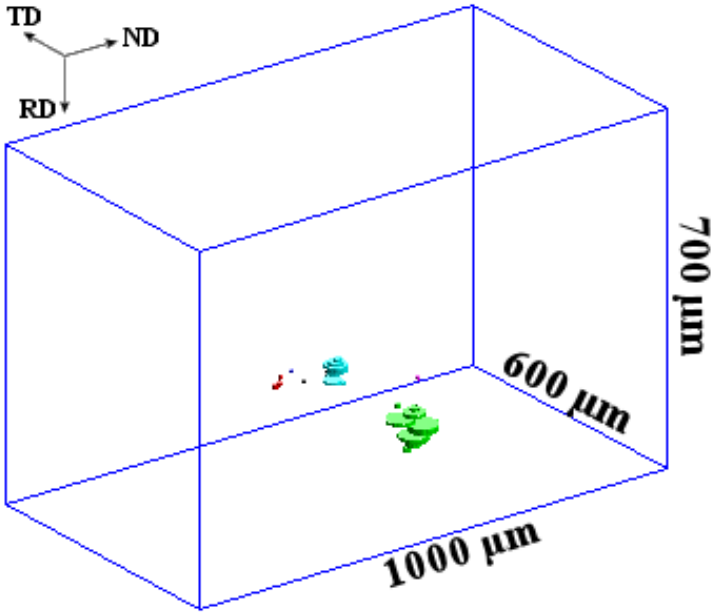

(a) Side view.

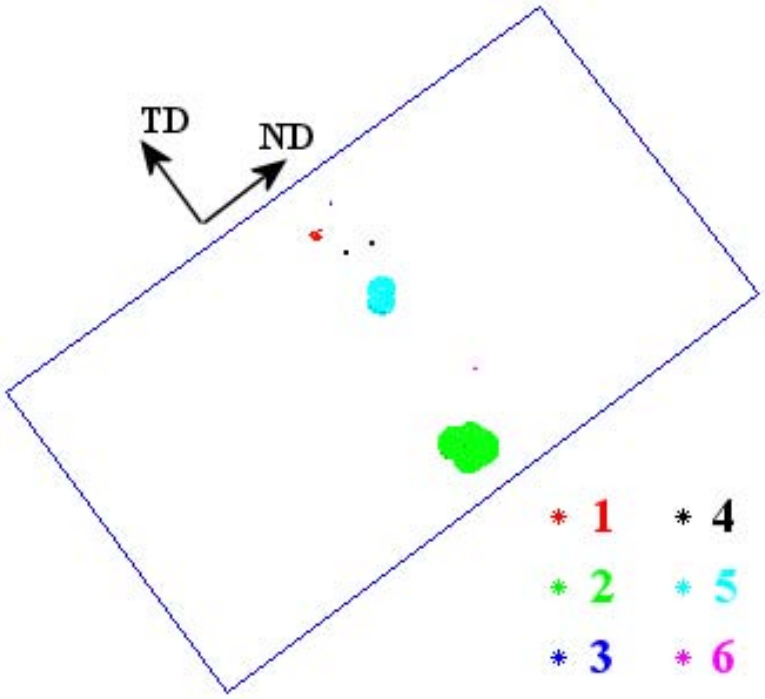

(b) Top view.

Figure 6.2: The 6 nuclei of new orientations. The volume in each layer has been plotted as a disc. The outline of the gauge volume is marked with blue lines.

6.1.3 Nuclei volumes

The volume corresponding to the diffraction spots can be calculated by calibration to the gold reference scan mentioned in section 5.4. The integrated intensity was found by adding up the intensity in a 21×21 pixel box around the diffraction spot in 5 consecutive (in ω) background-corrected images. This box size was found to be sufficient to contain the total intensity of the diffraction spots for more than half of the spots, despite deviations from the calculated spot position and saturation overflow. A larger box size would have been too prone to contain intensity from diffraction spots from other material volumes, either recrystallized crystallites or deformed grains. If the box contained diffraction spots from other grains, the spot was discarded in the analysis. However, diffraction spots close to the detection limit may not have been observed and could thus give an error in the volume calculation. For each spot, the volume was calculated using equation 5.4. The volume assigned to a nucleus was calculated as the average of the volumes corresponding to all accepted diffraction spots of the nucleus on the $\langle 111 \rangle$, $\langle 200 \rangle$, $\langle 220 \rangle$ and $\langle 311 \rangle$ rings. This ranged from 14 to 24 different diffraction spots.

As the beam was focused narrowly in the z direction, the volume found in this way corresponded to the volume of the small slice of a given grain which was illuminated by the beam during the imaging. Figure 6.2 shows a map of the six nuclei that were found away from the surfaces. In each layer, the volume was found from the intensity and plotted as a disk of diameter:

$$ECD_{\text{disc}} = 2\sqrt{\frac{V_c/h}{\pi}} \tag{6.1}$$

centered at the calculated center-of-mass position of the nucleus in that layer. Here $h = 7\mu$m is the hight of the layer. This means that the map is not a true representation of the actual nucleus shape. The standard deviation on the diameter EDC_{disc} was of the order of 20%. In table 6.1, the approximate extent in the xy plane of the nuclei L_{xy} is given as the maximal value of ECD_{disc} for each nucleus. A good agreement is seen between the order of magnitude of this number and the nucleus extent in the z direction L_z.

It is seen that some of the nuclei had grown quite large during the annealing, while others were still small. Two of the nuclei were seen only in one layer (3 and 6). Nucleus 4 was seen in two layers but with a significantly different center-of-mass, as is evident in the figure. The orientation of nucleus 4 was close to that of the tails of nucleus 5. The misorientation between nuclei 4 and 5 was only 5°, although most of the diffraction spots were clearly separated on the detector. However, a few of the diffraction spots were so close that they were visible in the same image or two images of neighboring

ω separated by only a few pixels on the detector. This could have caused the indexing software Grainspotter to calculate the center-of-mass based on a mixture of diffraction spots from the two nuclei. This gave the relatively large uncertainty on the position of nucleus 4.

6.2 Descriptions of the gauge volume before and after annealing

While the 3DXRD microscope has been used for three dimensional mapping of undeformed structures on several occasions, e.g. [72, 73, 105, 106], mapping of deformed materials has so far only been shown feasible with simulated near-field detector data [107]. However, the software has now been developed to a point where also moderately deformed samples may be mapped with a good accuracy.

In the present case, a map was reconstructed from the data set taken with the far-field detector. Originally, the intention was to do the mapping using the near-field data as had been done in the simulations, but as described this was not possible. Although a lower spatial resolution was obtained using the far-field data, this data contained diffraction from much smaller volume elements and was therefore very useful. The reconstruction process is completely new and took place late in the project, so only two layers were reconstructed, one before annealing and one after.

As can be seen in figure 5.2, the difference between diffraction from deformed and undeformed material is significant, making the reconstruction much more complex. The large spread of the diffraction spots from the deformed material makes the determination of positions and orientations difficult by overlap of intensity from many different volume elements. The reconstruction of a map from the present data of two layers in the partially recrystallized sample and deformed sample respectively was done by S. Schmidt using the GrainSweeper algorithm described in section 2.3.5. The maps presented here represent the first successful non-destructive 3-dimensional mapping of a deformed material using 3DXRD.

Because the grains in the sample were rather large, the grains seen in the interior of the sample and the grains seen on the surfaces overlapped to a large extent. The layer chosen for the reconstruction was layer 17 in the scan performed after annealing, corresponding to layer 18 in the scan before annealing due to drift during the experiment. This layer was chosen because it contained diffraction spots from three of the six nuclei of interest (nuclei 1-3), although one of these nuclei (nucleus 2) had already grown quite large

and was centered in another layer. The diffraction spots seen in this layer from nucleus 2 were probably caused by tails on the X-ray beam. The other two nuclei were, however, quite small; nucleus 3 was present only in this layer, while nucleus 1 was present in three layers with this one being the middle one.

In the following, the 3DXRD far-field data and data obtained from the two surfaces by EBSP will be presented and compared. Two complementary ways of visualizing the data are used; pole figures and orientation imaging maps. A pole figure presents the orientations present in the data, but comprises no spatial information. These verify that a good correspondence is found between surface and bulk methods. The orientation imaging maps show the orientations as a function of position and offer the opportunity of comparing nuclei orientations with orientations in the volume elements around the nucleation sites. For a general introduction to various representations of orientation data, see [108].

6.2.1 Orientation representations by {111} pole figures

Pole figures from caking of raw data

3DXRD diffraction data can be characterized as a set of two-dimensional distributions, one for each Debyer-Scherrer ring. These distributions are a function of the rotation angle ω and the azimuthal angle η. By means of a spherical projection, such distributions can be represented as pole figures [109]. The caking was done using Fit2D [110], and the conversion into contours or points in pole figures was done using Matlab scripts adapted from a script by H.F. Poulsen and S. Schmidt. Contour plots reveal a partial pole figure given by the ω range covered.

Figure 6.3 shows {111} pole figures from the same layer before and after annealing. As can be seen, the orientation changes are minimal. The grain named "D" in the EBSP maps (figures 6.7(a) and 6.8(a)) is seen to have diminished in intensity as was expected because it had been partially consumed by the nuclei. The orientations of the two nuclei 2 and 5 also are also apparent in the pole figure, as they were both quite large in this layer. Other new orientations seen in the pole figure after annealing correspond to surface nuclei.

Pole figure from 3DXRD far-field orientation imaging map

The orientations in the orientation imaging map reconstructed from the far-field detector data were plotted in a pole figure for comparison. Only ori-

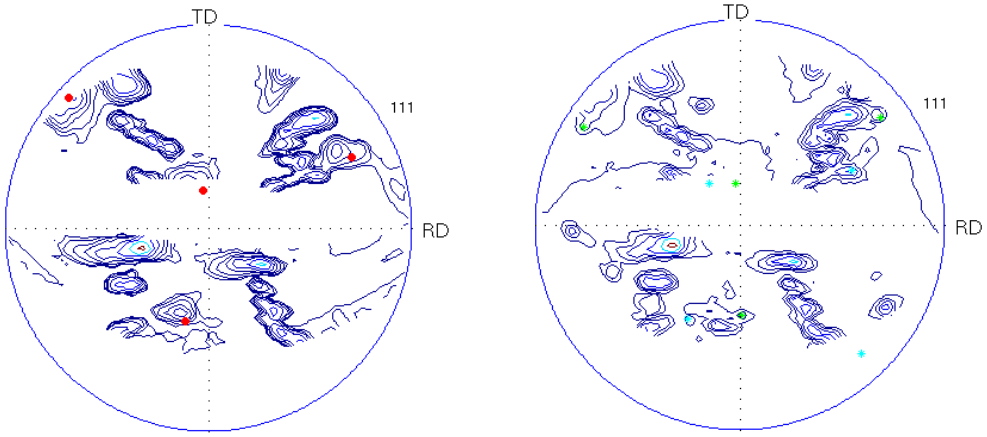

(a) Layer 26 before annealing. The areas near the top, middle and bottom without contour lines correspond to rotations ω which were not imaged. An orientation within the spread of the grain marked "D" in figures 6.7(a) and 6.8(a) is given by red points.

(b) Layer 25 after annealing. The areas near the top, middle and bottom without contour lines correspond to rotations ω which were not imaged. The orientations of Nuclei 2 and 5 are given by green and cyan stars respectively.

Figure 6.3: {111} pole figures from caking of 3DXRD data in a layer before and after annealing. One deformed grain has diminished and several sharp peaks corresponding to undeformed crystallites have appeared.

entations in points with a completeness factor of at least 0.5, i.e. where at least 50% of the expected diffraction spots were observed, are plotted. This included about 99 % of the points within the sample as well as some points outside. Figure 6.4 shows the orientations from the map of layer 17 (figure 6.6) compared with the orientations in an area of the EBSP maps corresponding roughly to 10 layers around the position of this layer. Some grains are only visible on one of the two EBSP pole figures, as not all grains transverse the sample. Together the two pole figures from the EBSP correspond very well to the orientations seen in the 3DXRD reconstruction. The orientations seen in figure 6.4(c) correspond closely to what was observed in the caking of the same layer, validating the orientation reconstruction.

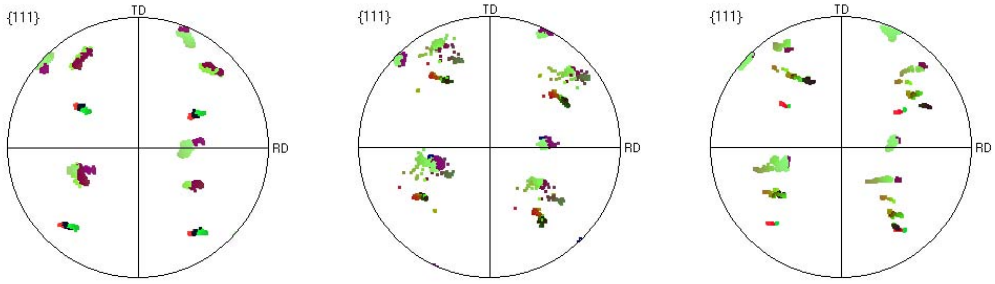

(a) Orientations from one of the surface EBSP maps in a small area around layer 17 after annealing (see figure 6.7(b)).

(b) Orientations from the other surface EBSP map in a small area around layer 17 after annealing (see figure 6.8(b)).

(c) Orientations in the far-field map of layer 17 after annealing (figure 6.6).

Figure 6.4: {111} pole figure of the orientations on the surface ((a) and (b)) compared with the orientations in the far-field map (c).

Pole figures from EBSP maps

EBSP data is traditionally represented as orientation imaging maps (se section 6.2.2). From such maps it is however straightforward to integrate over the spatial dimensions and generate pole figures. In figure 6.4, such pole figures were used to compare the 3DXRD orientations with the orientations seen in small areas on the surfaces. Figure 6.5 shows {111} pole figures of the entire mapped areas corresponding to two of the surfaces of the gauge volume before annealing. The pole figures were generated using the HKL Channel 5 software [62]. The colors were assigned based on Euler angles, so that each orientation will give rise to 4 points of the same color on the pole

figure. However, points of similar orientations may sometimes have quite different colors. This was detailed further in section 4.1.2.

Comparison with figure 6.3 shows that several of the large grains apparent on the surface were also found in the bulk as would be expected. This validates the transformations applied to the 3DXRD data to obtain orientations in the rolling coordinate system as well as the location of the gauge volume in the two types of mapping.

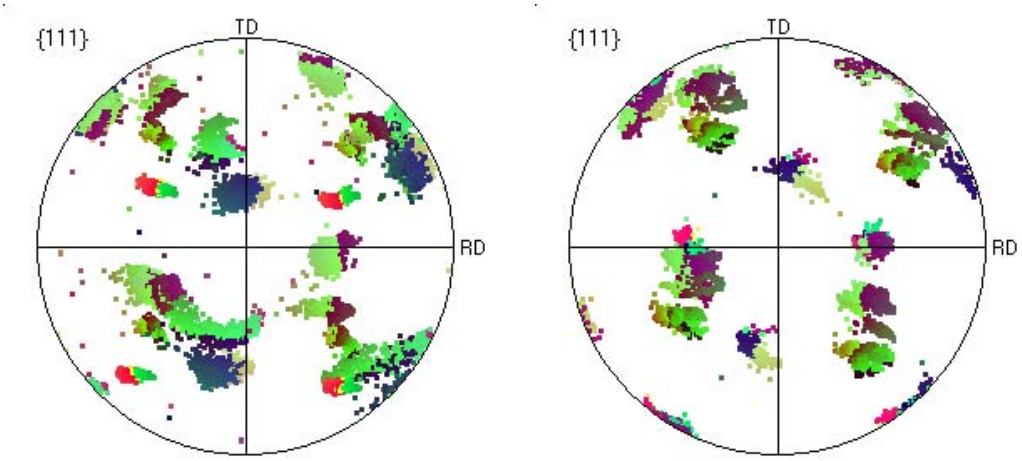

(a) Pole figure of the orientations present on one surface of the gauge volume before annealing (see figure 6.7(a)).

(b) Pole figure of the orientations present the opposite surface of the gauge volume before annealing (see figure 6.7(a)).

Figure 6.5: {111} pole figures from the two EBSP maps of the surface before annealing.

Discussion of pole figure results

The pole figures produced by different experimental methods (surface and bulk) showed many of the same grains, which was expected due to the large grain size. The differences between EBSP and 3DXRD pole figures were largely caused by the fact that the sections these methods probe were perpendicular to each other, i.e. they did not represent the same areas of the sample.

Pole figures based on caking were only partial, as they were based on single scattering vectors, where the different scattering vectors from the same crystal were not correlated to give an orientation. That good agreement was found between this type of pole figure and pole figures based on the

orientations reconstructed in a map was to be expected, as the same data was used. However, this comparison was still an important verification of the mapping method.

None of the pole figures representing the partially annealed structure in layer 17 based on 3DXRD data (caking or GrainSweeper map) were sensitive enough to show the nuclei. However, the nuclei orientations and positions were found directly from the diffraction spots using GrainSpotter, making orientation comparisons possible.

6.2.2 Orientation imaging maps

Spatial maps showing the crystallographic orientations as a function of position were constructed of the surface by EBSP and in the interior of the sample by reconstruction of the 3DXRD data.

Far-field map

As described in section 2.3.5, the program GrainSweeper is capable of reconstructing a map of the orientations on a grid inside the sample. Figure 6.6 shows a map of a single layer reconstructed from the data taken after annealing. The map shows the orientations in all points where the completeness factor is above 0.5. The orientations have been reconstructed on a grid of 10 μm. The uncertainty in position obtained in this way is of the order of two pixels, giving slightly fuzzy grain edges. The pixels have been colored according to the assigned orientation in the same manner as the EBSP maps. A comparison with the cutouts from the EBSP maps show that there is a good agreement with the positions and boundaries of the surface grains. The differences in color e.g. green/purple are due to very small orientation differences as can be seen by the fact that these colors are separated only by low-angle boundaries where they appear in the same map (see section 4.1.2).

Although three of the nuclei with new orientations found in section 6.1.2 had diffraction spots present in this layer, they did not show up on the map. This was partially due to the reconstruction method, which favors large grains. As each pixel is assigned the most likely orientation, the orientation in a pixel may be assigned the value of a large neighboring grain whose internal misorientations make the uncertainty in position quite large. The expected diameters of nuclei 1, 2 and 3 in this layer were 13 μm, 8 μm and 6 μm respectively. This means that they might not have a majority in any pixels and should thus only be present in at most one single pixel on the map. The diameter of nucleus 2 was based on diffraction spots caused by tails on the X-ray beam, as this nucleus was not actually present in layer 17.

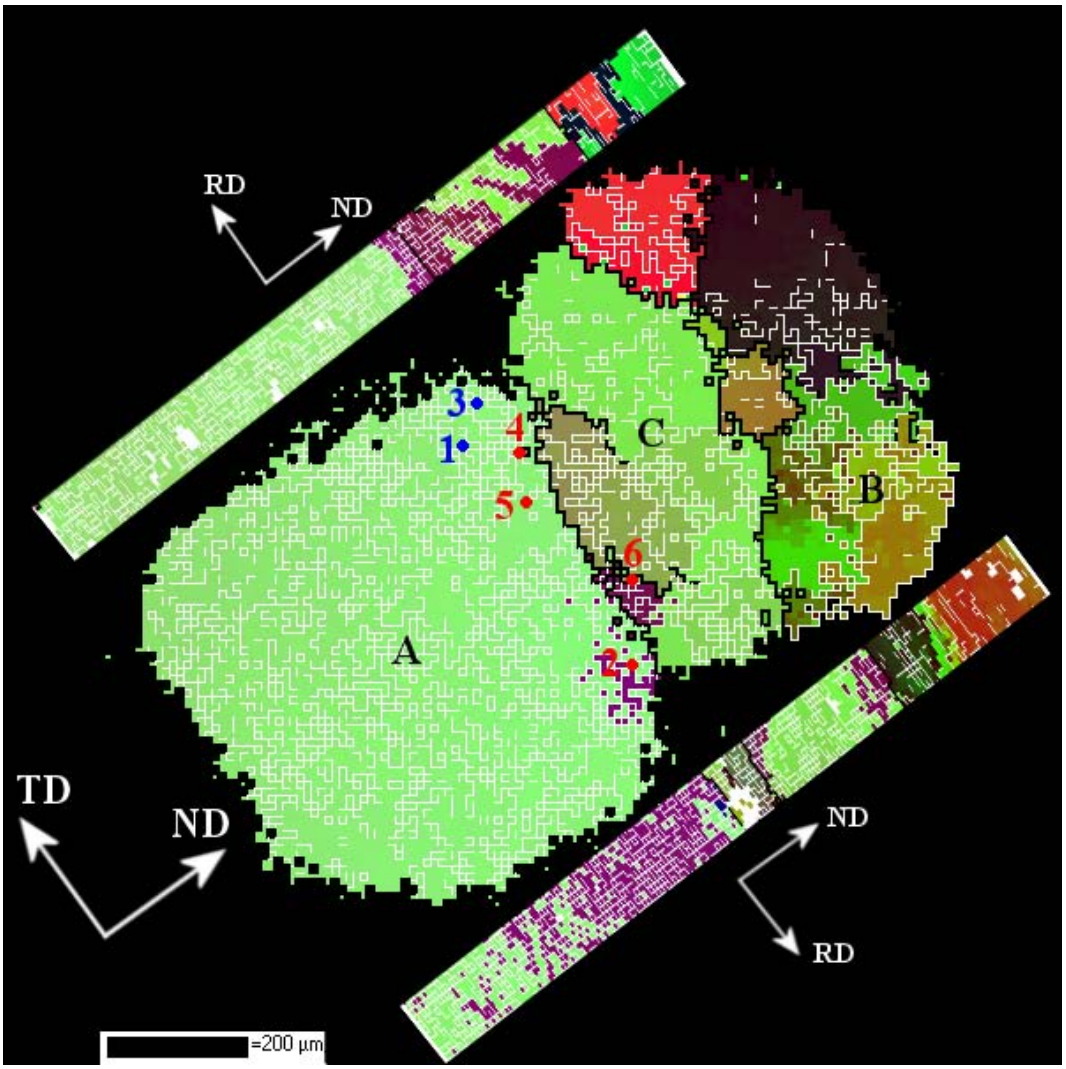

Figure 6.6: Sample cross section at layer 17 after annealing reconstructed from far-field data. Three of the grains appearing on the surface are marked with letters corresponding to the letters in figures 6.7(a) and 6.8(a).The positions of the six nuclei found with new orientations are superposed and marked with circles. The nuclei present in this layer are blue, while other nuclei are red. The sections from the surface maps marked in figures 6.7(b) and 6.8(b) are inserted for comparison of grains and boundaries. These should be considered as sides of a box perpendicular to the plane of the 3DXRD map, giving a 3-dimensional representation. The planes of the three sections are shown by different coordinate systems.

However, the positions of the nuclei were found with GrainSpotter, which finds the center-of-mass position as well as the orientation based on a specific subset of the diffraction spots. The positions of all six nuclei are plotted in figure 6.6. It is seen that all nuclei had appeared relatively close to the line separating grain "A" from the other grains. From the EBSP map it was apparent that this grain continued throughout the gauge volume in the RD direction. However, another grain, marked "D" was not observed in the 3DXRD map of layer 17. From direct observation of diffraction spots it was found that this grain was present in layers 18-60 before annealing, corresponding to a z size of $\sim 300\mu$m. This corresponds to layer 17-59 after annealing due to the small drift during the experiment. The intensity of the diffraction spots from grain "D" was significantly diminished in the images recorded after annealing, which fits well with the observations of the surface, where recrystallized surface crystallites had consumed a great part of this grain (see figure 6.7(b)).

EBSP mapping of the surface

Figures 6.7 and 6.8 show the EBSP maps of two of the sides of the gauge volumes examined by 3DXRD. Areas above and below this volume were also mapped by EBSP. The entire EBSP maps can be seen in appendix A. In the maps, white lines correspond to a misorientation between neighboring points of $>1^\circ$ but $<10^\circ$, while black lines correspond to a misorientation of $>10^\circ$. Both small and large nuclei are visible. These are not identical to the nuclei found by 3DXRD, as only the bulk nuclei were analyzed.

6.3 Comparison of nuclei orientations with deformed orientations

All 6 of the nuclei with new orientations found in the bulk of the sample were quite close in orientation, as can be seen in figure 6.9(a). In this section, their orientations will be correlated with the orientations seen in the deformed orientation imaging maps of the interior and surface of the sample before annealing. The aim is to observe the orientation relationships between the nuclei and the orientations present at the nucleation sites before annealing by an analysis of possible rotation axis. These axis will be correlated to the dislocation structure of the deformed material.

Although grain "D" was not observed in the map of layer 17 after annealing reconstructed from far-field data, EBSP maps of the surface as well as direct observation of the 3DXRD diffraction images indicate that this grain

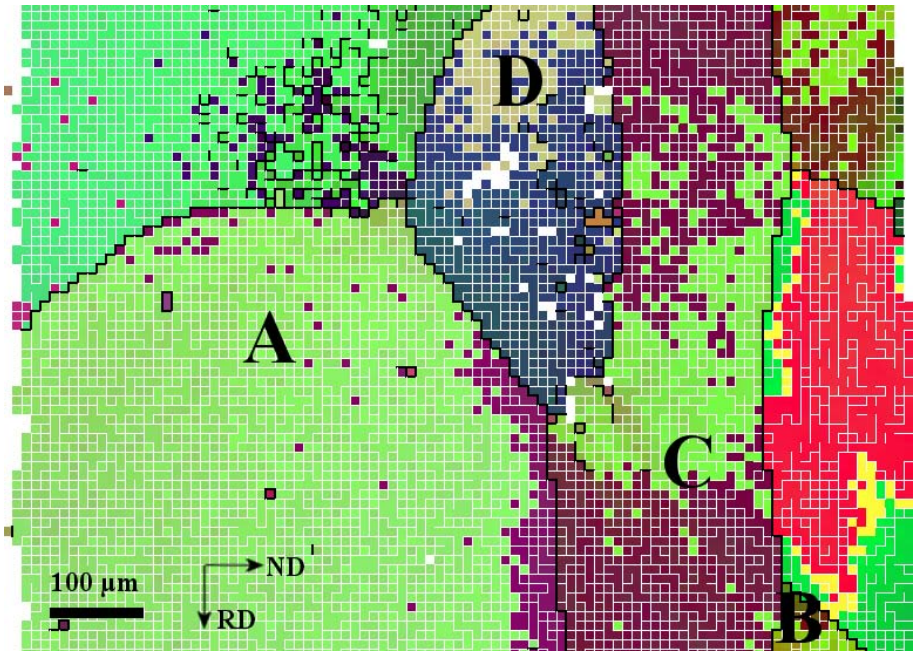

(a) Before annealing. The letters indicate grains which are found on both sides of the sample (compare with figure 6.8(a)). A complete pole figure of all orientations from this map was seen in figure 6.5(a).

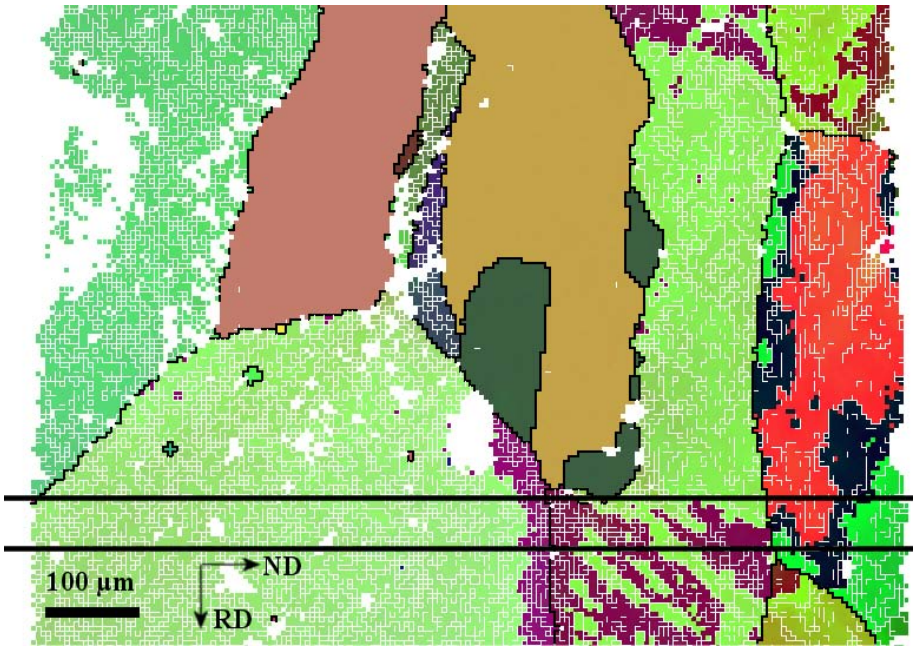

(b) After annealing. The box marks the area around layer 17 plotted in the pole figure 6.5(a).

Figure 6.7: EBSP maps of the surface of the gauge volume before and after annealing.

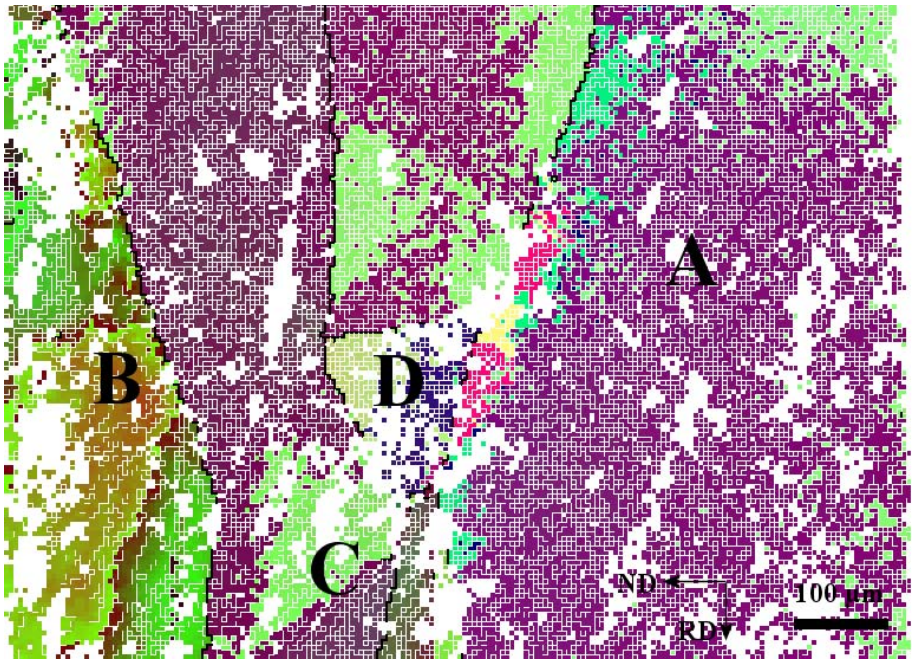

(a) Before annealing. The letters indicate grains which are found on both sides of the sample (compare with figure 6.7(a)). A complete pole figure of all orientations from this map was seen in figure 6.5(a).

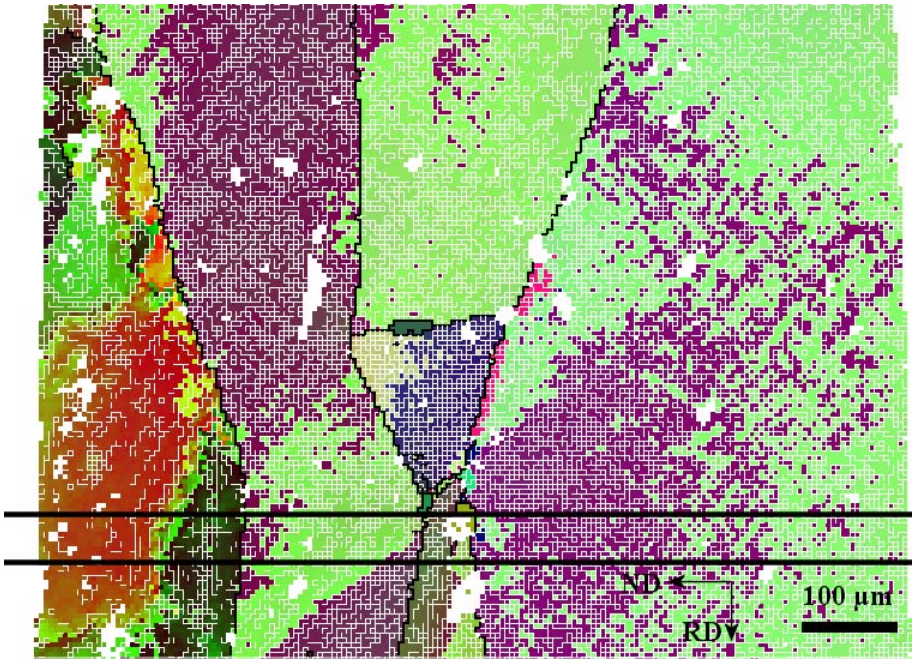

(b) After annealing. The box marks the area around layer 17 plotted in the pole figure 6.5(b).

Figure 6.8: EBSP maps of the surface of the gauge volume before and after annealing.

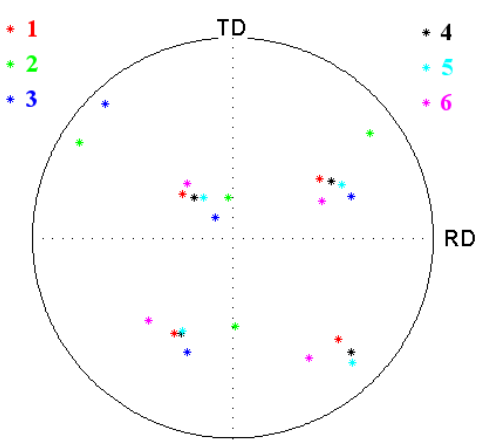

(a) {111} pole figure showing the orientations of the 6 nuclei with new orientations found in the bulk of the sample by 3DXRD.

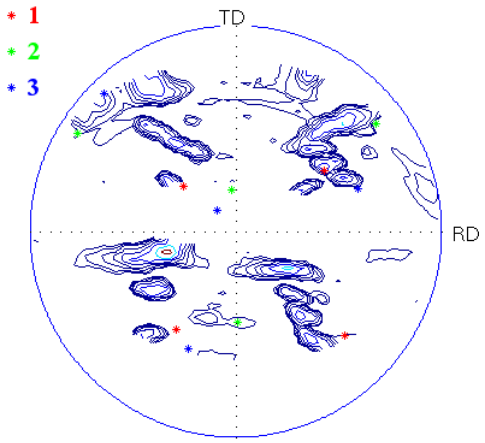

(b) {111} pole figure produced by caking of layer 17 after heating. The areas near the top, middle and bottom without contour lines correspond to rotations ω which were not imaged. The orientations of the three nuclei which had diffraction spots in this layer are overlaid.

Figure 6.9: {111} pole figures of the nuclei and one layer. The nuclei in layer 17 were all too small to appear in the pole figure, unlike the nuclei in layer 25 seen in figure 6.3(b).

was present in all layers where nuclei appeared. Furthermore, the position of grain "D" was seen to be close to the positions of all 6 nuclei. This orientations of grain were therefore also correlated to the nuclei orientations. Analysis of the orientations present in grain "D" indicate that it has high activity on many slip systems, making it likely to form slip plane aligned GNBs. Another map was reconstructed from layer 45 before annealing although no nuclei appeared in this layer, as the diffraction spots from grain "D" were at a maximum in this layer. Figure 6.10 shows this map and a {111} pole figure of the orientations. Grain "D" clearly appears in the map with an orientation within the spread of what was seen on the surfaces (figure 6.11).

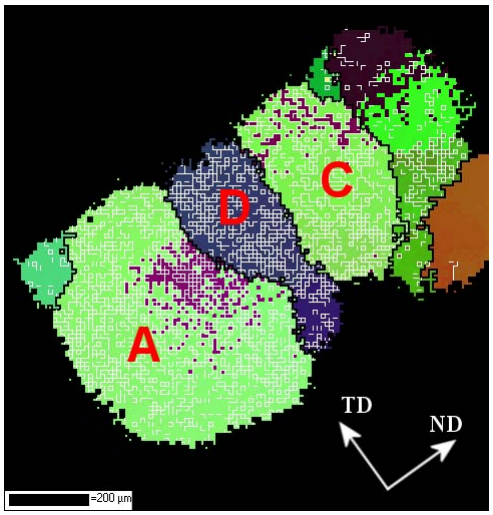

(a) Map of layer 45 before annealing reconstructed from 3DXRD data.

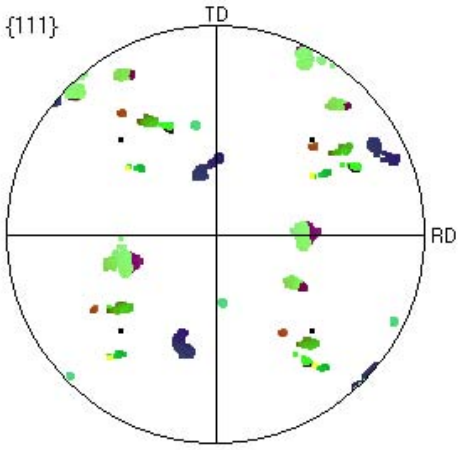

(b) {111} pole figure of the orientations present in the map.

Figure 6.10: The reconstruction of layer 45 showing grain "D" transversing the sample.

6.3.1 Slip plane analysis

An analysis of the active slip planes in the deformed structure to determine the alignment of GNBs was carried out in a similar manner as was done for the EBSP data in chapter 4.

Orientations from 3DXRD map

A comparison of the nuclei present in layer 17 with the orientations close to the nucleation sites in the 3DXRD map of this layer showed no agreement between possible rotation axes and slip plane aligned GNBs.

For completeness, the orientations of all the nuclei were compared with the orientations in all the grains "A", "B", "C" and other minor grains im the 3DXRD map, even though some of these were quite far away from the nucleation sites. No clear correlation between the expected slip planes and the nuclei orientations were found from the map.

Grain "D"

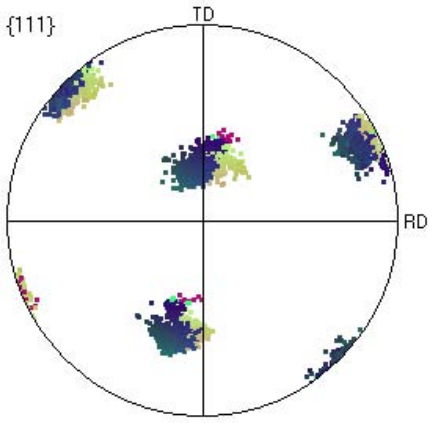

Figure 6.11: {111} pole figure of the orientations seen on both surfaces by EBSP within grain "D".

As all 6 nuclei with new orientations were formed in layers where grain "D" was present, the orientations within this grain were analyzed and compared with the nuclei orientations. The nuclei all had centers-of-mass corresponding well to the position of this grain.

The orientations of grain "D" used for the analysis was the entire set of orientations given by points on either surface assigned to the grain in the scans before annealing. This might include orientations quite far from what was actually present at the nucleation site, but the exact orientations at these sites were not reconstructed. As the orientation differences between points in grain "D" on the two surfaces were minimal, these points were expected to cover the orientations within the grain reasonably well. Also, as was seen from the reconstruction of layer 45 before annealing, the orientation spread

of grain "D" in a single layer was significantly smaller than the spread seen in the RD direction (compare pole figures 6.11 and 6.10(b)). The average orientation was calculated from the EBSP maps to be $(\phi_1, \Phi, \phi_2) = (65, 41, 23)$ with an orientation deviation of up to 11° from this.

Possible rotation axes

Table 6.2 lists all possible rotation axes between a point in grain "D" and the 6 nuclei of new orientations. As the misorientations between the nuclei and the points within the orientation spread of the grain were sometimes quite low, many different rotations around axes with a deviation of less than 10° were possible. It is seen in the table that generally the nuclei with the largest minimum misorientation to the deformed grain have the fewest possible rotation axes, as would be expected. Therefore, the possible rotation axes observed in these nuclei are more reliable than the rotation axes observed for the nuclei with a very small misorientation to the deformed grain.

Observation of the diffraction images before and after annealing confirmed that the orientations of the nuclei were not present before annealing.

Based on a Schmid factor analysis of the orientations in grain "D", 8 active slip systems were possible. These 8 systems were also predicted by the Taylor model, which gave 4 equivalent solutions with 5 systems each. The large number of systems as well as the number of equivalent solutions made it difficult to predict the GNB planes in this grain. There were several different possibilities, including GNBs aligned with all 4 {111} slip planes. In general, however, there were 3 systems common to all of the Taylor model solutions. These originated from 3 different slip planes, where two of them shared the same slip direction, giving codirectional slip. These two systems would give rise to GNB planes near (010) while the third would give a GNB aligned with (1-11).

The axes listed in table 6.2 were all analyzed to determine if they corresponded to normals to any of these expected GNB planes or to deviation axes of these planes.

Possibility of ⟨100⟩-rotations

As was discussed in [111] and section 4.4, the rotation giving new orientations could either originate from a rotation around the GNB plane normal or be caused by a rotation around the axis of misorientation across the GNB. For GNBs of twist character, as was the case for GNBs aligned with {111}, the resulting rotation would be the same. However, a (010)-aligned GNB, as was predicted in this case, is expected to have a tilt character and thus a

Nucleus	Orientation (ϕ_1, Φ, ϕ_2) (min. mis.)	Misorientation axis to deformed grain ("D") slip	Misorientation axis to deformed grain ("D") no slip	Axis deviation	Misorientation angle
1	42 18 50 (14°)	[-101]		4°	36°
		[100]		**1°**	**31°**
			[-211]	5°	
2	80 45 18 (3°)	**[111]**		**2°**	**18°**
		[110]		2°	15°
			[011]	3°	
		[010]		7°	9°
		[112]		1°	11°
			[121]	2°	
			[211]	2°	
3	44 40 44 (7°)	**[11-1]**		**1°**	**16°**
		[110]		1°	19°
			[0-11]	4°	
		[010]		7°	12°
		[11-2]		3°	27°
			[121]	4°	
		[1-21]		7°	17°
		[12-1]		2°	18°
			[21-1]	3°	
4	48 24 42 (8°)	[101]		9°	12°
		[-101]		2°	20°
		[100]		**0°**	**20°**
			[-211]	6°	
5	50 27 37 (6°)	[-101]		3°	11°
		[100]		**1°**	**8°**
			[-211]	7°	
			[2-11]	1°	
6	18 17 62 (19°)	**[100]**		**0°**	**29°**

Table 6.2: The 6 nuclei with new orientations. The minimum misorientation to any point in the surface EBSP map is given for each nucleus. All rotations around an axis within 10° of the ideal are listed; those which which may be explained by the slip plane analysis are listed under "slip", while those where no correspondence was found are listed under "no slip". The axes marked in boldface are the axes considered to be the most likely candidates for the rotations.

misorientation axis lying in the GNB plane. In the present analysis, the rotation axes [101], [$\bar{1}$01], [100] and [001] lie in the (010) plane and were thus possible misorientation axes. Therefore, these axes were also included in the analysis.

Nucleus 6 had only one possible rotation axis, namely [100]. This was also the nucleus seen to have the largest minimum misorientation to all points in the deformed grain, indicating that the rotation axis was reliable. The assignment of this rotation axis was further strengthened by the fact that there was no deviation from this axis, i.e. the orientation of the nucleus was perfectly rotated about [100] from a point seen before annealing.

The [100] rotation axis appeared with a deviation of only 0°-1° for 4 of the 6 nuclei with new orientations, indicating that this axis is a preferred rotation axis for the nucleation process. As described above, slip plane analysis showed that the [100] axis was a possible misorientation axis across (010)-aligned GNBs.

⟨111⟩-rotations

The two nuclei (2 and 3) which did not appear to be rotated around [100] both had a possible rotation about a ⟨111⟩ axis with a low deviation, although in both cases the rotation was relatively small, giving a large uncertainty on the assignment of the correct axis. Nucleus 2 showed a rotation around [111] and nucleus 3 showed a rotation around [11-1] (see table 6.2). These ⟨111⟩ axes were also in agreement with the GNB structure predicted by slip system analysis, being normal to the slip plane aligned GNBs expected to have twist character.

Summary of orientation relations

The orientations of the 6 nuclei with new orientations were compared with the orientations seen in the 3DXRD map of a layer in the partially-annealed structure as well as on the surfaces before annealing. Although the comparison in the bulk was with orientations after annealing, as no map was reconstructed before annealing, the raw data was available from the same layer before annealing, so the orientations of the nuclei could be concluded to be new. Also, the 3DXRD orientation imaging map showed the same large deformed grains as before annealing, so a comparison with these was found to be sound.

No correlations between the orientations of the deformed grains in the 3DXRD map and the new nuclei were found, but a plausible correlation was found with another grain, "D".

The orientations used to represent grain "D" were all taken from the surface EBSPs, and might not be representative of the orientations at the nucleation sites. The presence of transition bands or other deformation structures leading to orientations very different from what was seen at the surfaces is a possibility, although such features were not seen in the reconstructed layer 45 before annealing. However, the orientation spread of grains on the two surfaces was quite similar, and the orientations seen in layer 45 were within the surface orientations with a smaller spread. Due to the small misorientations from grain "D" of some of the nuclei, care was taken to verify that the orientations were not present in the deformed state by direct examination of the diffraction spot positions in the images before and after annealing. Also, due to the orientation spread of grain "D", the rotation angles of the nuclei were likely to be larger than what was given in table 6.2, as this is the rotation angle from a point with the smallest deviation of the rotation axis. But this point was not necessarily in close proximity of the nucleation site, and other points with a similar deviation from the ideal rotation axis might give rotations up to $\sim 20^\circ$ larger. E.g. for nucleus 5 there was another point in the set of orientations from grain "D" from which the deviation from perfect [100]-rotation was just as small (1°), but the rotation was 24°, not 8°.

6.4 Discussion

Map

An orientation imaging map was reconstructed from two separate layers in the un-annealed and annealed sample. This was the first time such a mapping was done on real data from a deformed sample. Furthermore, this reconstruction was based on far-field detector data, where mapping has previously been done using near-field detector data. Although this gave a lower spatial resolution, which at about 15-20 μm was slightly larger than the pixel size used in the reconstruction, a very good result was achieved. Only minor empty areas were seen in the maps. The appearance of the orientation imaging maps shows a rounding of corners of all grains and slightly fuzzy grain boundaries, but the orientations and positions of the grains corresponded well with surface maps.

Nuclei of new orientations

The orientations of the 6 nuclei found in the bulk can be conclusively said to be new, but the exact orientations at the nucleation sites and thus the

precise orientation relationships would require a complete 3-dimensional reconstruction of the gauge volume around the nucleation sites. Thanks to recent progress in software development, this is now possible, but the complete 3D analysis was deemed outside the scope of the present study, in part for reasons of timing. But the orientation relations found still offer a valid analysis of the possible rotation axes between nucleus and deformed structure, although the exact angles of rotation may be different.

The rotation axis [100] was seen in 4 of the 6 nuclei with rotations between 8° and 31°, corresponding to a possible misorientation axis across (010)-aligned GNBs.

The two nuclei not showing a rotation around [100] were the nuclei closest to the surfaces (2 and 3). This may suggest a possible surface origin, although precautions were taken to select only nuclei expected to be bulk.

The fact that a [100] rotation was found is a very interesting result, as the rotation axis did not appear to be the slip plane normal but rather the misorientation axis. The EBSP experiments only found rotations around $\langle 111 \rangle$ axes, corresponding to both the slip plane normal and the expected misorientation axis. The fact that a grain expected to form GNBs of tilt character was seen in this experiment allowed a distinction between the slip plane normal and the misorientation axis to be made. The results indicate that the feature of the microstructure giving rise to nucleation of new orientations may not be the planes of the GNBs but rather the misorientation across them.

Chapter 7

Conclusions

Nucleation of recrystallization was studied by different experimental methods to increase the knowledge of the relationships between the orientations of the recrystallized nuclei and the orientations present in the deformed structure. Both surface and bulk methods were used, the results complementing each other.

In order to have only a few well-defined parent orientations present in the vicinity of any potential nucleation site, a material was prepared from high-purity aluminum with a relatively large grain size. After 30% deformation, the original grains and boundaries were still recognizable in this material, but sufficient energy had been stored mainly in the form of dislocations to initiate nucleation. The dislocations would form call boundaries and GNBs.

The results obtained have lead to the following:

- An optimization of the 3DXRD setup for the purpose of studying nucleation of recrystallization. The setup allowed a large gauge volume to be mapped before and after annealing in order to observe the rare nucleation events. The 3DXRD method probes the bulk of the material non-destructively, allowing measurements to be carried out at the nucleation sites inside the sample before the nucleation. This meant that the orientations present before annealing could be compared directly with the nuclei orientations.

  The 3DXRD results were supported and substantiated by EBSP measurements on several samples. EBSP was also used to map the surfaces of the 3DXRD samples.

- The EBSP results have confirmed that triple junctions and grain boundaries are good nucleation sites. SIBM was seen to be an important nucleation mechanism, creating nuclei with parent orientations, but

nuclei with orientations not present in the deformed material were also seen. The parent oriented nuclei tended to have the largest internal orientation spread.

- From the EBSP measurements it was seen that about 1/3 of the nuclei had orientations not observed before annealing. Using a surface method always leaves some uncertainty about the orientations present below the surface, but results from the 3DXRD experiments have confirmed that nuclei of orientations not present in the deformed state can appear. Examination of the volume around the nucleation sites was done both by pole figures and direct examination of diffraction images.

- An analysis of the orientation relations between the nuclei of new orientations found by the two different experimental methods was carried out. In the EBSP experiments, the nuclei orientations were seen to be rotated about a specific $\langle 111 \rangle$-axis. In all cases which could not be explained by twinning, this axis corresponded to the normal to the $\{111\}$ plane of the most active slip system. GNBs of twist character are expected to form on such planes, meaning that the slip plane normal coincided with the misorientation axis of the GNB. The axis of rotation could thus be either the GNB plane normal or the misorientation axis associated with the GNB.

- In the 3DXRD experiment, some the nuclei of new orientations appeared rotated about such $\langle 111 \rangle$-axes, while the majority were rotated about [100]. This was explained by the inclination of the parent grain to form GNBs of tilt character on $\{010\}$, where [100] could be the misorientation axis. The 3DXRD results thus supported the hypothesis that certain grains forming GNBs aligned with crystallographic planes appeared more likely to give rise to nuclei with new orientations. Furthermore, the rotation axis associated with the new orientations observed appeared to be the misorientation axis rather than the GNB plane normal.

Chapter 8

Experimental outlook

This chapter presents some thoughts on the limitations of the experiments and ideas for improvements. The chapter focuses mainly on 3DXRD experiments, as the EBSP method is well established.

Spark cutting

The main aim of the 3DXRD experiment was to study nucleation of new orientations in the bulk of a sample. However, nucleation was also seen at the surfaces, particularly at one of the spark cut surfaces. Most of these had already appeared before annealing, apparently due to heat from the spark cutting process. This was unfortunate, but as the position of all crystallites could be found from the data set, the bulk nuclei could be separated from those on the surface. The observation of spark cutting initiating nucleation in this type of sample has to be remembered in sample preparation for future experiments on recrystallization.

Different material

Using a different material such as copper would be interesting in order to determine if the hypotheses formed from these experiments on aluminum would hold for other materials as well. Another possibility would be to use aluminum prepared to have a very specific texture with only a few of the grains expected to give rise to nuclei embedded in a structure af many grains predicted to be less active. This would also be a good test of the validity of the predictions. However, the preparation of such a material might not be feasible in practice.

Near-field data

The near-field data was in the end not used for reconstruction of maps. This was because the data was incomplete due to the relatively low efficiency of the detector. The efficiency of the near-field detector was about an order of magnitude less than the efficiency of the far-field detector. A longer exposure time could have increased the intensity of the diffraction spots on this detector. However, the smaller dynamic range of the near-field detector meant that the diffraction spots from small volumes such as nuclei could not have been detected without the diffraction spots of the large deformed grains reaching saturation due to the grain size of the material. A map with a higher spatial resolution could in principle have been reconstructed from near-field data with a longer exposure time. However such a map would likely have contained holes, as small diffracting volumes could not be resolved on the detector. The analysis was therefore based on the data obtained with the far-field detector.

New detectors

Recent work by U. L. Olsen [112] at Risø DTU has focused on the development of a new type of fluorescent screen for use in a new detector. This screen, which is based on a so-called structured scintillator, has a several times higher efficiency than the normal phosphor screens, combined with diminished tails in the point spread function. A stacked detector has been implemented at ID11 comprising two detectors which will eventually both use such screens, allowing orientation imaging maps to be reconstructed much faster and with a higher spatial resolution. The high resolution of this detector makes it ideal for use as a near-field detector, replacing the Quantix detector used for the experiments described in chapter 5.

Another detector being constructed is the so-called nanodetector, which will combine several stacked detectors into a 3D detector with a very high spatial resolution down to 100 nm. This will allow very detailed reconstructions of the deformed structure. For nucleation studies aiming at observing large numbers of nuclei, this detector may nor be relevant, as the volumes mapped will typically be smaller than desired. However, a very high-resolution map of a single nucleation area and the resulting nucleus might offer additional insight into the mechanisms of nucleation.

Surface nuclei in 3DXRD study

Although many of the crystallites found on the surfaces of the sample in the 3DXRD experiment described in chapter 6 were already present before an-

nealing, some of them only appeared during the annealing treatment. These were of course also valid nuclei and could have been subjected to the same analysis as the other nuclei, in correspondence with the study performed by EBSP in chapter 4. At least 4 such nuclei which did not extend outside the gauge volume were observed at the mechanically polished surfaces. However, due to the problems caused by the nuclei appearing at the spark cut surfaces, all surface nuclei were neglected in the data analysis.

3D reconstruction

A complete three-dimensional reconstruction could in principle be made from the present data both before and after annealing. As the mapping was quite time-consuming and was done late in the project, a few of the most relevant layers were selected for reconstruction. This gave good results and was sufficient for the analysis required.

A stacking of layers would however provide the complete spatial information, allowing the orientations in selected volumes to be studied.

Complete three-dimensional maps of deformed samples based on near-field data will be reconstructed in the near future by members of the M4D centre. The use of near-field data means that a higher spatial resolution can be obtained than what was seen in the maps presented here.

Future experiments

The ideal experimental result for this type of study should include many more bulk nuclei. Also, if the orientations at the nucleation sites were known with a higher spatial resolution, a better comparison of the orientations could be made. Better spatial resolution is available using near-field detectors, but as discussed, this may limit other aspects of the data that may be obtained.

The experimental method used for the 3DXRD experiment described here may not readily be improved to give orders of magnitude more nuclei to improve on the statistics. Several minor improvements are possible with the present setup, such as:

- Using a starting material with a slightly smaller grain size. This would allow smaller volumes to be detected without saturating the detector. As nucleation is expected to happen mainly at triple junctions and grain boundaries, more nuclei might be observed in the same volume. However, the challenge would be to anneal to a point where many nuclei had appeared but none of them had grown too large.

- Using a smaller step size in the rotation and/or the layer spacing using a beam focused to a smaller height in z would give a better spatial resolution of the map. These improvements would both require either more time or give a smaller gauge volume.
- Using new detectors with a higher spatial resolution and/or improved efficiency. As mentioned in chapter 7, such detectors are being developed.
- Measuring at a lower energy would also give an increase in the flux and thus decrease the acquisition time.

But the best way to obtain a large number of nuclei is simply to map a much larger volume using a similar or smaller angular and spatial resolution as was done here. At present, this is not possible within a normal beam time. However, several planned improvements of the hardware available may make such a study feasible.

- The beamline ID-11 will have a new in-vacuum undulator installed, which is expected to increase the flux by a factor of ~ 8.
- In time, the beamline wishes to replace the Frelon detectors with a Pilatus detector, which gives a significantly lower level of background noise by sidestepping the need for a fluorescent screen and by detecting single photons.

Together with some of the improvements mentioned for the present setup, a factor of ~ 100 may thus be attainable in the volume mapped per time. Of course, a continued quest for increased spatial resolution and a smaller detection limit would again decrease this factor.

Bibliography

[1] C. Kittel. *Introduction to Solid State Physics, 7th ed.* Wiley, 1996.

[2] K. Marthinsen and N. Ryum. Transformation kinetics and microstructure for grain boundary nucleated recrystallization in two dimensions. *Acta Materialia*, 45(3):1127–1136, March 1997.

[3] F. J. Humphreys and M. Hatherley. *Recrystallization and related annealing phenomena*. Elsevier Ltd., Oxford, U.K., 1. edition, 1995.

[4] J. Hansen, J. Pospiech, and Lücke K. *Tables for Texture Analysis of Cubic Crystals*. Springer, 1978.

[5] Y. Quere. *Physics of Materials*. Taylor & Francis, 1998.

[6] E. C. W. Perryman. Observations on the structural changes accompanying recovery in super-purity aluminium. *Acta Metallurgica*, 2(1):26–37, 1954.

[7] E. C. W. Perryman. Relationship between recovery and recrystallization in superpurity aluminum. *Transactions Of The American Institute Of Mining And Metallurgical Engineers*, 203(9):1053–1064, 1955.

[8] M.M. Eisenstadt. *Introduction to Mechanical Properties of Materials*. The Macmillan Company, 1971.

[9] X. Huang and G. Winther. Dislocation structures. part i. grain orientation dependence. *Philosophical Magazine*, 87(33):5189–5214, 2007.

[10] Subra Suresh. *Fatigue of Materials*. Cambridge University Press, 2 edition, 1998.

[11] G.I. Taylor. Plastic strain in metals. *Journal of the Institute of Metals*, 62:307–324, 1938.

[12] D. Kuhlmann-Wilsdorf and N. Hansen. Geometrically necessary, incidental and subgrain boundaries. *Scripta Metallurgica et Materialia*, 25:1557–1562, 1991.

[13] R. D. Doherty, D. A. Hughes, F. J. Humphreys, J. J. Jonas, D. J. Jensen, M. E. Kassner, W. E. King, T. R. McNelley, H. J. McQueen, and A. D. Rollett. Current issues in recrystallization: a review. *Materials Science And Engineering A-Structural Materials Properties Microstructure And Processing*, 238(2):219–274, November 1997.

[14] N. Hansen. New discoveries in deformed metals. *Metallurgical and Materials Transactions A (Physical Metallurgy and Materials Science)*, 32A(12):2917–2935, 2001.

[15] J. W. Cahn. A new theory of recrystallization nuclei. *Proceedings of the Physical Society. Section A*, 63:323–336, 1950.

[16] R. D. Doherty and J. A. Szpunar. Kinetics of sub-grain coalescence - a reconsideration of the theory. *Acta Metallurgica*, 32(10):1789–1798, 1984.

[17] J. C. M. Li. Possibility of subgrain rotation during recrystallization. *Journal Of Applied Physics*, 33(10):2958–&, 1962.

[18] P.A. Beck and P.R. Sperry. Strain induced boundary migration in high purity aluminum. *Journal of Applied Physics*, 21(2):150–152, 1950.

[19] P. Faivre and R. D. Doherty. Nucleation of recrystallization in compressed aluminium: studies by electron microscopy and kikuchi diffraction. *Journal of Materials Science*, 14:897–919, 1979.

[20] A. R. Jones, B. Ralph, and N. Hansen. Subgrain coalescence and the nucleation of recrystallization at grain-boundaries in aluminum. *Proceedings Of The Royal Society Of London Series A-Mathematical Physical And Engineering Sciences*, 368(1734):345–&, 1979.

[21] F. J. Humphreys and M. Ferry. On the role of twinning in the recrystallization of aluminium. *Scripta Materialia*, 35(1):99–105, July 1996.

[22] P. Wilkes. *Solid State Theory in Metallurgy*. Cambridge University Press, 1973.

[23] D.A. Porter and K.E. Easterling. *Phase transformations in metals and alloys*. CRC Press, Boca Raton, FL, 2. edition edition, 2004.

[24] J. W. Cahn. The kinetics of grain boundary nucleated reactions. *Acta Metallurgica*, 4(5):449–459, 1956.

[25] F. J. Humphreys. Nucleation of recrystallisation in metals and alloys with large particles. *Proceedings of the 1st Risø International Symposium on Metallurgy Materials Science*, pages 35–44, 1980.

[26] F.J. Humphreys and M.G. Ardakani. The deformation of particle-containing aluminum single-crystals. *Acta Metallurgica et Materialia*, 42(3):749–761, MAR 1994.

[27] H Paul, JH Driver, and Z Jasienski. Shear banding and recrystallization nucleation in a cu-2%al alloy single crystal. *Acta Materialia*, 50(4):815–830, FEB 25 2002.

[28] J. H. Driver, H. Paul, Glez J.-C., and Maurice C. Relations between deformation substructure and nucleation in fcc crystals. *Proceedings of the 21st Risø International Symposium on Materials Science*, pages 35–48, 2000.

[29] F Inoko and K. Kashihara. Formation of recrystallized grains along deformation bands in aluminum single crystals. *Materials Science Forum*, 113-115:139, 1993.

[30] F. Inoko, T. Okada, M. Tagami, and K. Kashihara. Relation between deformed microstructure and <111>(fcc) and <011>(bcc) rotation recrystallization mechanisms. *Proceedings Of The 20th Risø International Symposium on Materials Science*, pages 375–380, 1999.

[31] K. Kashihara, M. Tagami, T. Okada, and F. Inoko. Nucleation of recrystallized grains in multiple slipped structure without deformation band in aluminum single crystal. *Materials Science And Engineering A-Structural Materials Properties Microstructure And Processing*, 291(1-2):207–217, October 2000.

[32] K. Kashihara, M. Tagami, T. Okada, and F. Inoko. Nucleation of recrystallized grains in interiors and surfaces of aluminum single- and poly-crystals. *Proceedings of the 21st Risø International Symposium on Materials Science*, pages 371–377, 2000.

[33] A. W. Larsen. *Quantitative studies of the nucleation of recrystallization in metals utilizing microscopy and X-ray diffraction.* PhD thesis, Risø National Laboratory, Roskilde, Denmark, 2005.

[34] A. W. Larsen, H. F. Poulsen, L. Margulies, C. Gundlach, Q. F. Xing, X. X. Huang, and D. J. Jensen. Nucleation of recrystallization observed in situ in the bulk of a deformed metal. *Scripta Materialia*, 53(5):553–557, September 2005.

[35] T. Okada, M. Tagami, K. Kashihara, and F. Inoko. Relationship between active slip systems and orientations of recrystallized grains in fe-30cr alloy. *Isij International*, 38(6):518–523, 1998.

[36] T. Okada, W. Y. Liu, and F. Inoko. Recrystallization mechanism involving $\langle 110 \rangle$ rotation in fe-30cr alloy single crystal. *Materials Transactions Jim*, 40(7):586–593, July 1999.

[37] H Paul. Nucleation of recrystallization in channel-die compressed al single crystals. *Materials Chemistry and Physics*, 81(2-3):531–534, AUG 28 2003. 11th International Conference on Electron Microscopy of Solids, Krynica, Poland, May 19-23, 2002.

[38] H. Paul and J. Driver. New orientation formation during recrystallization of cold deformed, high symmetry aluminium bicrystals. *Microchimica Acta*, 155(1-2):235–242, SEP 2006.

[39] H Paul, JH Driver, C Maurice, and Z Jasienski. Crystallographic aspects of the early stages of recrystallisation in brass-type shear bands. *Acta Materialia*, 50(17):4339–4355, OCT 9 2002.

[40] H. Paul, J. H. Driver, and A. Lens. Mechanisms of new orientation formation during recrystallization of cold deformed aluminium bicrystals. *Materials Science Forum*, 495-497:1249–1254, 2005.

[41] H. Paul, J. H. Driver, C. Maurice, and A. Piatkowski. Recrystallization mechanisms of low stacking fault energy metals as characterized on model silver single crystals. *Acta Materialia*, 55(3):833–847, FEB 2007.

[42] T. J. Sabin and D. Juul Jensen. Nucleation at triple junctions in pure aluminium. *Proceedings of the 21st Risø International Symposium on Materials Science*, pages 539–544, 2000.

[43] T. J. Sabin, G. Winther, and D. J. Jensen. Orientation relationships between recrystallization nuclei at triple junctions and deformed structures. *Acta Materialia*, 51(14):3999–4011, August 2003.

[44] S.R. Skjervold and N. Ryum. Orientation relationships in a partially recrystallised polycrystalline alsi-alloy. *Acta Materialia*, 44:3407–3419, 1996.

[45] G. Wu, A. Godfrey, D. Juul Jensen, and Q. Liu. The orientations of nuclei at triple junctions in deformed columnar grain ni. *ICOTOM 14: Textures of Materials Pts 1 and 2*, 495-497(Part 1&2):1309–1314, 2005.

[46] G. L. Wu and D. Juul Jensen. Orientations of recrystallization nuclei developed in columnar-grained ni at triple junctions and a high-angle grain boundary. *Acta Materialia*, 55(15):4955–4964, SEP 2007.

[47] B. Radhakrishnan, G. B. Sarma, and T. Zacharia. Modeling the kinetics and microstructural evolution during static recrystallization - monte carlo simulation of recrystallization. *Acta Materialia*, 46(12):4415–4433, July 1998.

[48] M. Upmanyu, D. J. Srolovitz, A. E. Lobkovsky, J. A. Warren, and W. C. Carter. Simultaneous grain boundary migration and grain rotation. *Acta Materialia*, 54(7):1707–1719, April 2006.

[49] G. Winther and X. Huang. Dislocation structures. part ii. slip system dependence. *Philosophical Magazine*, 87(33):5215–5235, 2007.

[50] B. Duggan. Term suggested at international conference on textures of materials, icotom 11. 1996.

[51] H.F. Poulsen. *3DXRD - a new probe for materials science*. Risø National Laboratory, Roskilde, Denmark, 2004.

[52] M.N. Alam, M. Blackman, and D.W. Pashley. High-angle kikuchi patterns. *Proceedings of the Royal Society of London Series A-Mathematical and Physical Sciences*, 221(1145):224, 1954.

[53] J.A. Venables and C.J. Harland. Electron back-scattering patterns-a new technique for obtaining crystallographic information in the scanning electron microscope. *Philosophical Magazine*, 27(5):1193–1200, 1973.

[54] D.J. Dingley. Diffraction from sub-micron areas using electron backscattering in a scanning electron microscope. *Scanning Electron Microscopy*, pages 569–575, 1984.

[55] D. Dingley. Progressive steps in the development of electron backscatter diffraction and orientation imaging microscopy. *Journal Of Microscopy-Oxford*, 213:214–224, March 2004.

[56] N.C.K. Lassen, D.J. Jensen, and K. Conradsen. Image-processing procedures for analysis of electron back scattering patterns. *Scanning Microscopy*, 6(1):115–121, MAR 1992.

[57] http://www.crystaltexture.com, 2009.

[58] D. Juul Jensen and V. Randle. Combined advanced techniques in the study of annealing processes. *Proceedings Of The 10th Risø International Symposium on Materials Science*, pages 103–126, 1989.

[59] D. J. Dingley and V. Randle. Microtexture determination by electron back-scatter diffraction. *Journal Of Materials Science*, 27(17):4545–4566, September 1992.

[60] P.J. Goodhew, J. Humphreys, and R. Beanland. *Electron Microscopy and Analysis*. Taylor & Francis, 2001.

[61] N. C. Krieger Lassen. *EBSD on JEOL JSM-840 using CROMATIC v. 2.10*. Risø National Laboratory, 2001.

[62] http://www.oxinst.com/products/microanalysis/ebsd/ebsd-acquisition-software/pages/channel5.aspx, 2009.

[63] H. F. Poulsen, S. Garbe, T. Lorentzen, D. J. Jensen, F. W. Poulsen, N. H. Andersen, T. Frello, R. Feidenhansl, and H. Graafsma. Applications of high-energy synchrotron radiation for structural studies of polycrystalline materials. *Journal Of Synchrotron Radiation*, 4:147–154, May 1997.

[64] H.F. Poulsen and D. Juul Jensen. Synchrotron radiation diffraction: A novel tool for recrystallization studies in bulk μm sized local areas. *Proceedings of the 16th Risø International Symposium on Materials Science*, pages 503–508, 1995.

[65] L. Margulies, G. Winther, and H. F. Poulsen. In situ measurement of grain rotation during deformation of polycrystals. *Science*, 291(5512):2392–2394, March 2001.

[66] C. Gundlach, W. Pantleon, E. M. Lauridsen, L. Margulies, R. D. Doherty, and H. F. Poulsen. Direct observation of subgrain evolution during recovery of cold-rolled aluminium. *Scripta Materialia*, 50(4):477–481, February 2004.

[67] E. M. Lauridsen, D. J. Jensen, H. F. Poulsen, and U. Lienert. Kinetics of individual grains during recrystallization. *Scripta Materialia*, 43(6):561–566, August 2000.

[68] E.M Lauridsen, S. Schmidt, S.F. Nielsen, L. Margulies, H.F. Poulsen, and D. Juul Jensen. Non-destructive characterization of recrystallization kinetics using three-dimensional x-ray diffraction microscopy. *Scripta Materialia*, 55(1):51–56, July 2006. Viewpoint set no. 41 '3D Characterization and Analysis of Materials' Organized by G. Spanos.

[69] P. Hedström, U. Lienert, J. Almer, and M. Odén. Elastic strain evolution and η-martensite formation in individual austenite grains during in situ loading of a metastable stainless steel. *Materials Letters*, 62:338–340, 2008.

[70] X. Fu, H.F. Poulsen, S. Schmidt, S.F. Nielsen, E. M. Lauridsen, and D. Juul Jensen. Non-destructive mapping of grains in three dimensions. *Scripta Materialia*, 49(11):1093–1096, December 2003.

[71] S. F. Nielsen, W. Ludwig, D. Bellet, E. M. Lauridsen, H.F. Poulsen, and D. Juul Jensen. Three dimensional mapping of grain boundaries. *Proceedings of the 21th Risø International Symposium on Materials Science*, pages 473–478, 2000.

[72] S. Schmidt, S. F. Nielsen, C. Gundlach, L. Margulies, X. Huang, and D. J. Jensen. Watching the growth of bulk grains during recrystallization of deformed metals. *Science*, 305(5681):229–232, July 2004.

[73] S. Schmidt, U.L. Olsen, H.F. Poulsen, H.O. Sørensen, E.M. Lauridsen, L. Margulies, C. Maurice, and D. Juul Jensen. Direct observation of 3-d grain growth in al-0.1%mn. *Scripta Mater*, 59:491–494, 2008.

[74] J. Als-Nielsen and D. McMorrow. *Elements of Modern X-Ray Physics*. Wiley, 2001.

[75] http://www.risoe.dk/afm/synch/micro.htm, 2009.

[76] Esrf highlights, 2006.

[77] U. Lienert, H. F. Poulsen, V. Honkimaki, C. Schulze, and O. Hignette. A focusing multilayer analyser for local diffraction studies. *Journal Of Synchrotron Radiation*, 6:979–984, September 1999.

[78] H.F. Poulsen. *Three-Dimensional X-Ray Diffraction Microscopy: Mapping Polycrystals and their Dynamics*. Springer, 2004.

[79] C. Schulze, U. Lienert, M. Hanfland, M. Lorenzen, and F. Zontone. Microfocusing of hard x-rays with cylindrically bent crystal monochromators. *Journal Of Synchrotron Radiation*, 5:77–81, March 1998.

[80] http://www.esrf.eu/usersandscience/experiments/materialsscience/id11, 2009.

[81] E. M. Lauridsen, S. Schmidt, R. M. Suter, and H. F. Poulsen. Tracking: a method for structural characterization of grains in powders or polycrystals. *Journal Of Applied Crystallography*, 34:744–750, December 2001.

[82] H. F. Poulsen, S. F. Nielsen, E. M. Lauridsen, S. Schmidt, R. M. Suter, U. Lienert, L. Margulies, T. Lorentzen, and D. J. Jensen. Three-dimensional maps of grain boundaries and the stress state of individual grains in polycrystals and powders. *Journal Of Applied Crystallography*, 34:751–756, December 2001.

[83] D. Juul Jensen, E. M. Lauridsen, L. Margulies, H. F. Poulsen, S. Schmidt, H. O. Sorensen, and G. B. M. Vaughan. X-ray microscopy in four dimensions. *Materials Today*, 9(1-2):18–25, January 2006.

[84] http://www.totalcryst.dk, 2009.

[85] http://fable.wiki.sourceforge.net/, 2009.

[86] U. Lienert, H.F. Poulsen, and A. Kvick. High energy x-ray microscope for the local structural characterization of bulk materials. *Collection of Technical Papers - AIAA/ASME/ASCE/AHS/ASC Structures, Structural Dynamics and Materials Conference*, 3:2067–2075, 1999.

[87] S. Schmidt. http://fable.wiki.sourceforge.net/grainspotter, 2009.

[88] S. Schmidt. http://fable.svn.sourceforge.net/viewvc/fable/grainsweeper/, 2009.

[89] R. A. Vandermeer and P. Gordon. Edge-nucleated, growth controlled recrystallization in aluminum. *Transactions Of The American Institute Of Mining And Metallurgical Engineers*, 215(4):577–588, 1959.

[90] O. V. Mishin, B. Bay, and D. J. Jensen. Through-thickness texture gradients in cold-rolled aluminum. *Metallurgical And Materials Transactions A-Physical Metallurgy And Materials Science*, 31(6):1653–1662, June 2000.

[91] W. Truszkowski, J. Krol, and B. Major. Inhomogeneity of rolling texture in fcc metals. *Metallurgical Transactions A (Physical Metallurgy and Materials Science)*, 11A:749–758, 1980.

[92] S. S. West, S. Schmidt, and D. Juul Jensen. Experimental quantification of nucleation. *Proceedings of the 29th Risø International Symposium on Materials Science*, pages 383–389, 2008.

[93] Q. Liu, D. Juul Jensen, and N. Hansen. Effect of grain orientation on deformation structure in cold-rolled polycrystalline aluminium. *Acta Materialia*, 46(16):5819–5838, 1998.

[94] G. Winther. Slip patterns and preferred dislocation boundary planes. *Acta Materialia*, 51(2):417–429, January 2003.

[95] G. Winther, D. Juul Jensen, and N. Hansen. Dense dislocation walls and microbands aligned with slip planes - theoretical considerations. *Acta Materialia*, 45(12):5059–5068, December 1997.

[96] Y Huang and FJ Humphreys. Measurements of grain boundary mobility during recrystallization of a single-phase aluminium alloy. *Acta materialia*, 47(7):2259–2268, MAY 28 1999.

[97] E. Nes and H.E. Vatne. The $40°\langle 111\rangle$ orientation relationship in recrystallisation. *Zeitschrift fur Metallkunde*, 87(6):448–453, 1996.

[98] C.Y.J. Barlow, B. Bay, and N. Hansen. A comparative investigation of surface relief structures and dislocation microstructures in solid-rolled aluminium. *Philosophical Magazine A (Physics of Condensed Matter, Defects and Mechanical Properties)*, 51:253–275, 1985.

[99] V. Randle, N. Hansen, and D. Juul Jensen. The deformation behaviour of grain boundary regions in polycrystalline aluminium. *Philosophical Magazine A*, 73:265–282, 1996.

[100] C. Gundlach. *Recovery in Aluminium*. PhD thesis, University of Copenhagen, 2006.

[101] A. P. Hammersley, S. O. Svensson, A. Thompson, H. Graafsma, A. Kvick, and J. P. Moy. Calibration and correction of distortions in 2-dimensional detector systems. *Review Of Scientific Instruments*, 66(3):2729–2733, March 1995.

[102] B.E. Warren. *X-Ray Diffraction*. Dover, 1990.

[103] W.H. Zachariasen. *Theory of X-ray Diffraction in Crystals*. Dover, 1967.

[104] http://www.esrf.eu/usersandscience/experiments/tbs/scisoft/xop2.3/main, 2009.

[105] K. Hannesson and D. J. Juul Jensen. Three dimensional characterization of grain structures by ebsp and 3dxrd. *Materials Science Forum*, 558-559:751–756, 2007.

[106] S. Schmidt, H. F. Poulsen, and G. B. M. Vaughan. Structural refinements of the individual grains within polycrystals and powders. *Journal of Applied Crystallography*, 36:326–332, April 2003.

[107] L. Rodek, H. F. Poulsen, E. Knudsen, and G. T. Herman. A stochastic algorithm for reconstruction of grain maps of moderately deformed specimens based on x-ray diffraction. *Journal of Applied Crystallography*, 40(Part 2):313–321, APR 2007.

[108] M. Hatherley and W.B. Hutchinson. An introduction to textures in metals. The Institution of Metallurgists, 1979. Monograph No 5.

[109] H. F. Poulsen, E. M. Lauridsen, S. Schmidt, L. Margulies, and J. H. Driver. 3d-characterisation of microstructure evolution during annealing of a deformed aluminum single crystal. *Acta Materialia*, 51(9):2517–2529, May 2003.

[110] A.P. Hammersley, S.O. Svensson, M. Hanfland, A.N. Fitch, and D Häusermann. Two-dimensional detector software: From real detector to idealised image or two-theta scan. *High Pressure Research*, 14:235–248, 1996.

[111] S.S. West, G. Winther, and D Juul Jensen. Analysis of orientation relations between deformed grains and recrystallization nuclei. *Submitted*, 2009.

[112] U.L. Olsen. *New generation of efficient high resolution detector for 30-100 keV*. PhD thesis, Risø DTU and University of Copenhagen, 2008.

[113] S. S. West, G. Winther, L. Margulies, E. Knudsen, H. O. Sørensen, S. Schmidt, and D. Juul Jensen. Mapping partially recrystallized structures by 3dxrd. *Materials Science Forum*, 558-559:389–394, 2007.

Appendix A

EBSP maps

Figures A.1 to A.7 show the EBSP maps on which the analysis in chapter 4 is based.

The EBSP maps of the surfaces of the 3DXRD sample used for the experiment described in chapters 5 and 6 are seen in figures A.8 and A.9.

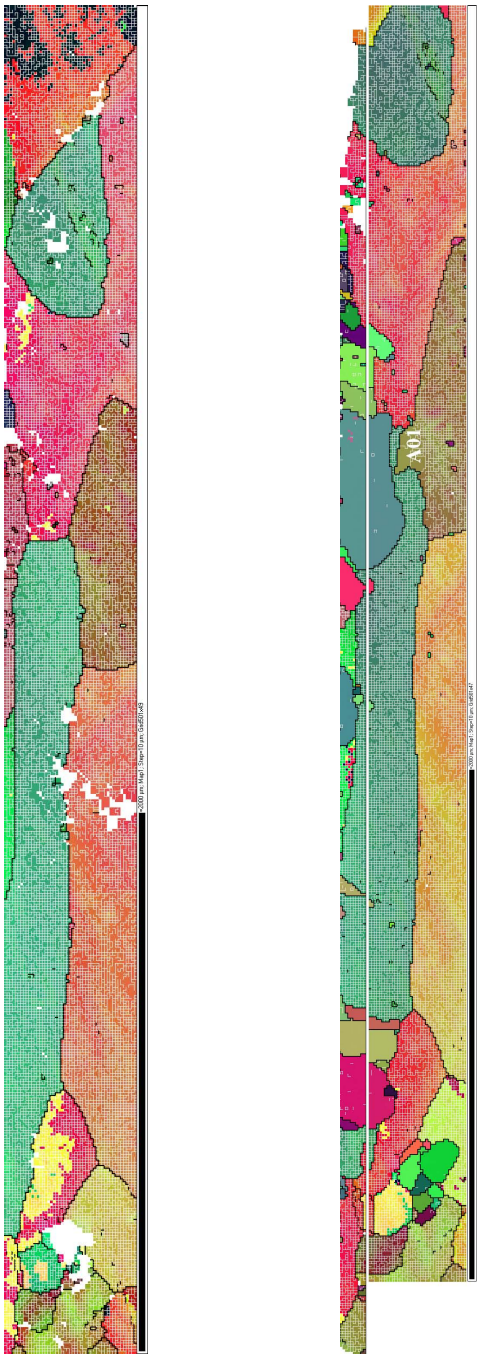

(a) Before annealing.

(b) After annealing at 320° for 15 minutes.

Figure A.1: EBSP sample A.

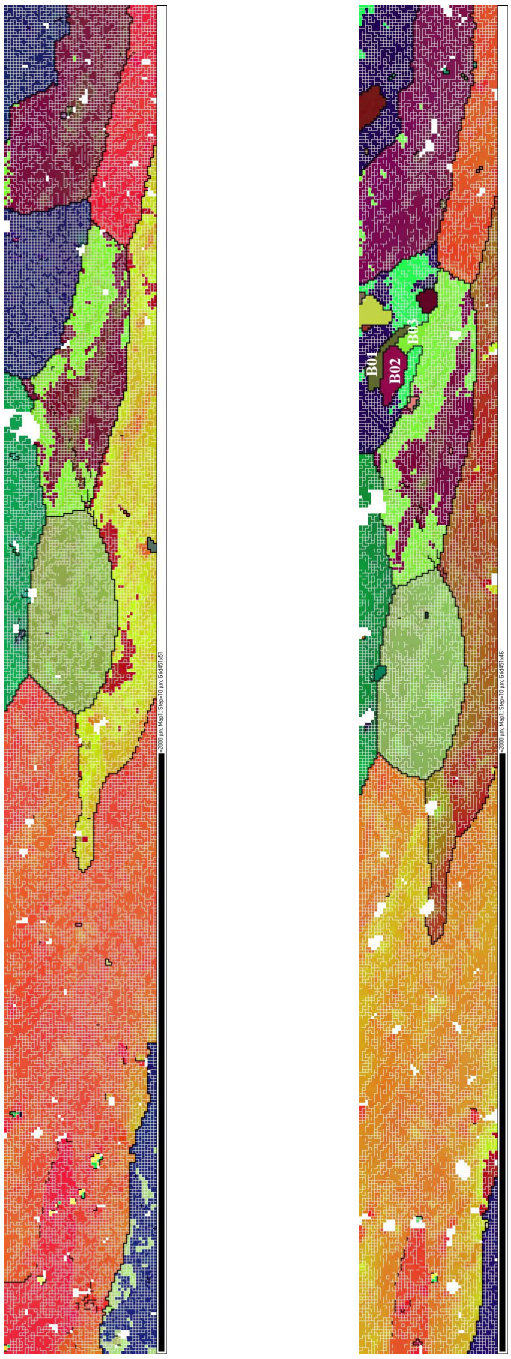

(a) Before annealing.

(b) After annealing at 320° for 15 minutes.

Figure A.2: EBSP sample B.

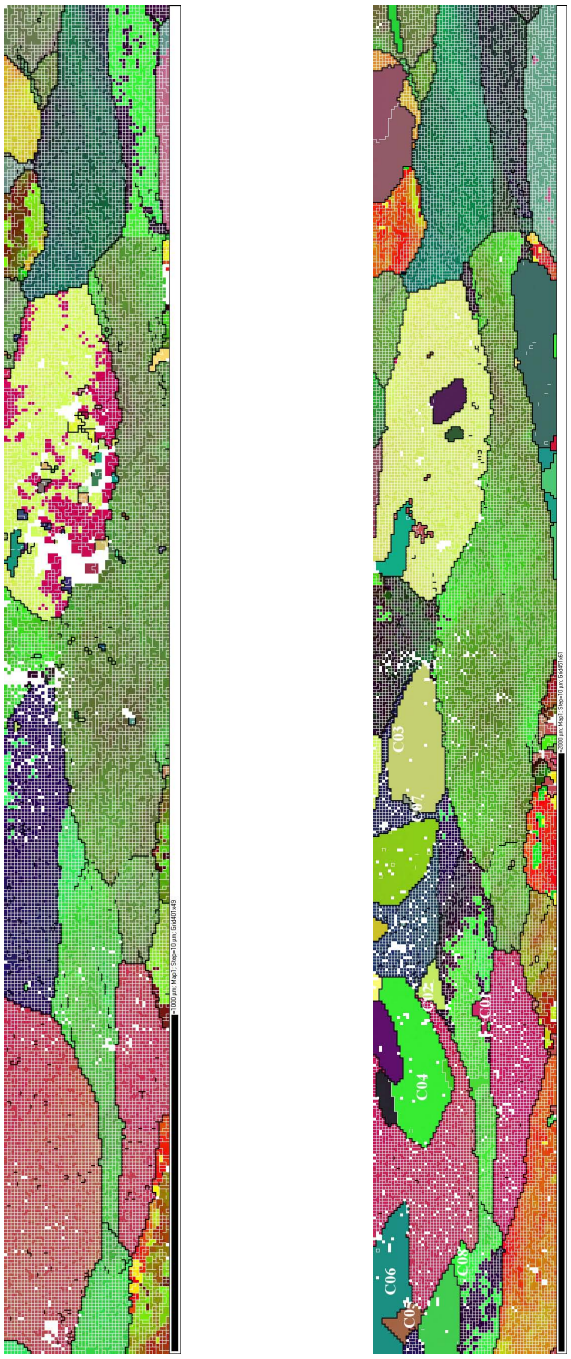

(a) Before annealing.

(b) After annealing at 315° for 15 minutes.

Figure A.3: EBSP sample C.

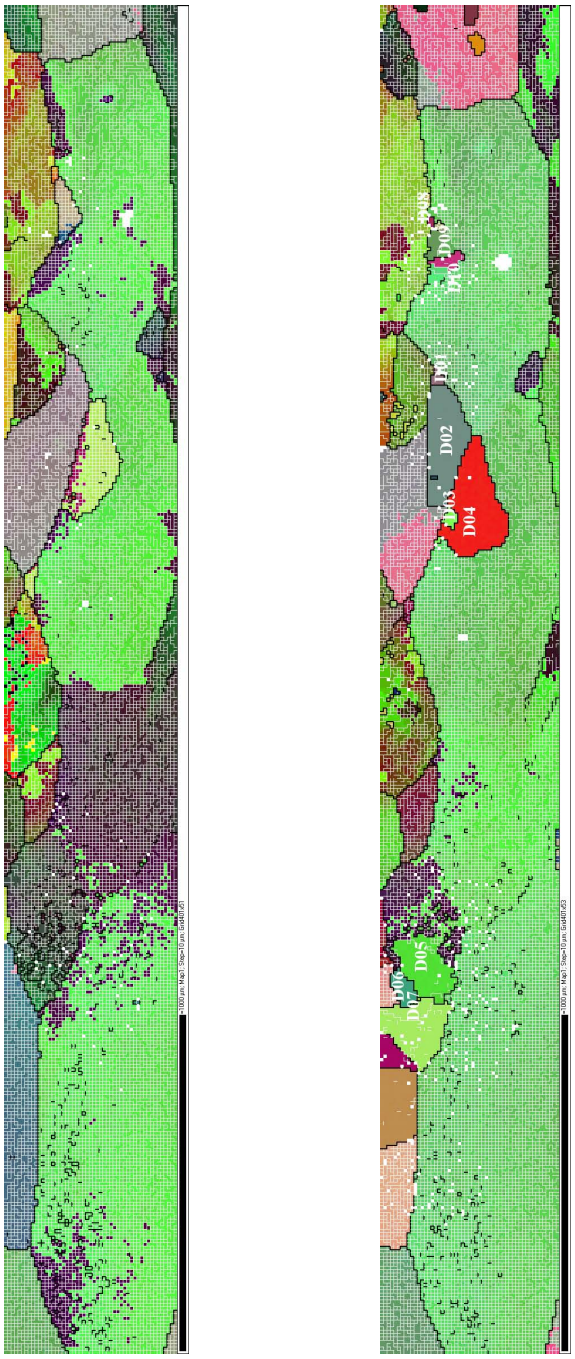

(a) Before annealing.

(b) After annealing at 315° for 15 minutes.

Figure A.4: EBSP sample D.

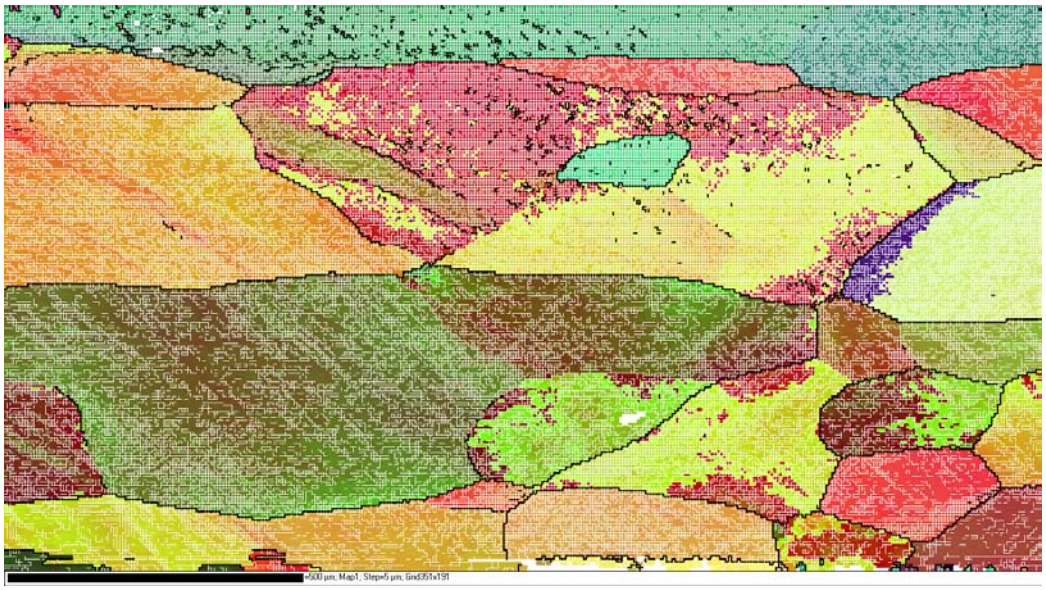

(a) Before annealing.

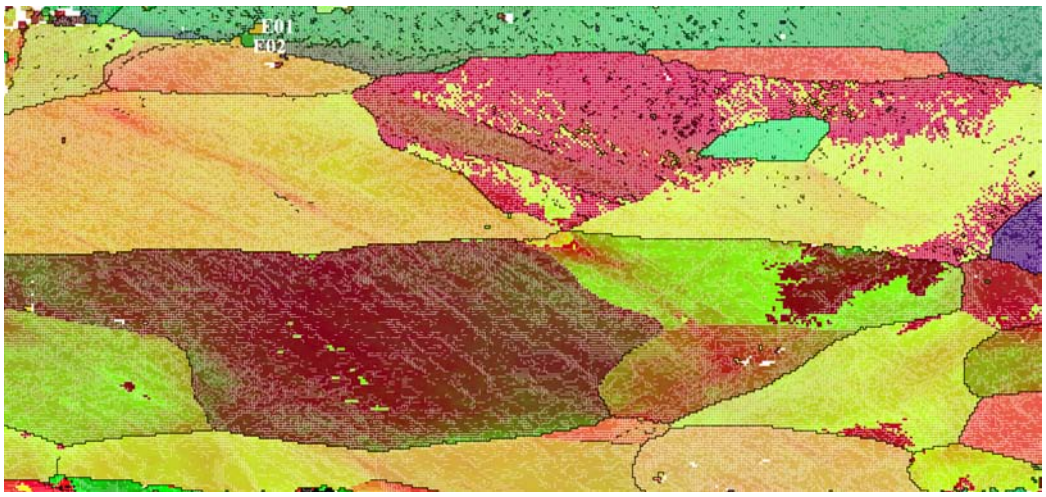

(b) After annealing at 315° for 12 minutes.

Figure A.5: EBSP sample E.

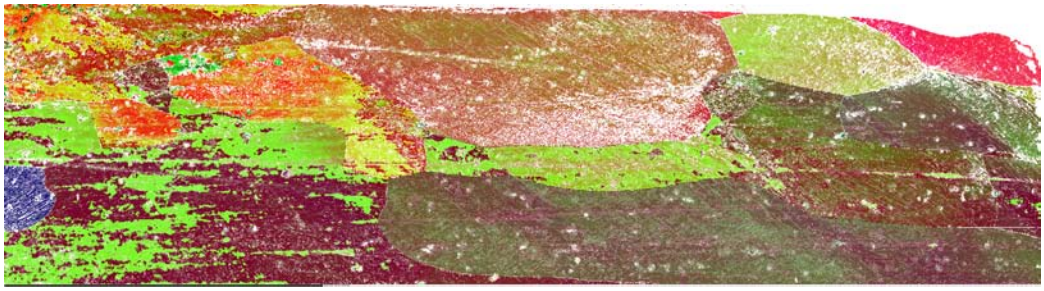

(a) Before annealing.

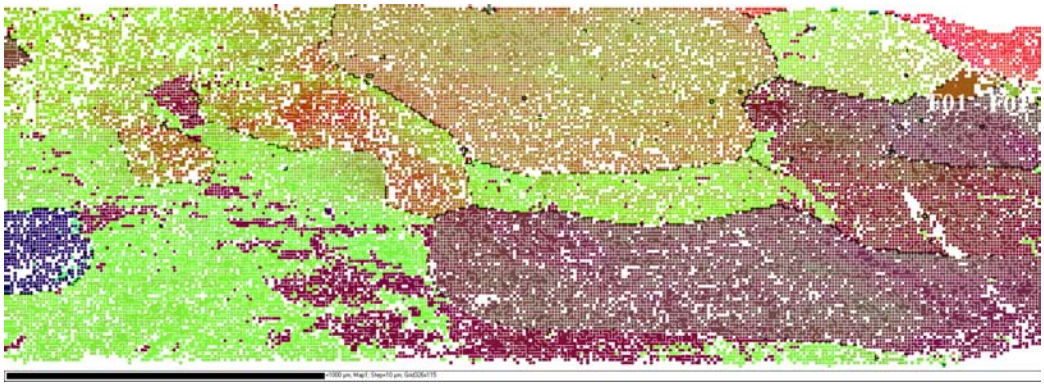

(b) After annealing at 320° for 10 minutes.

(c) After annealing at 320° for 10 minutes.

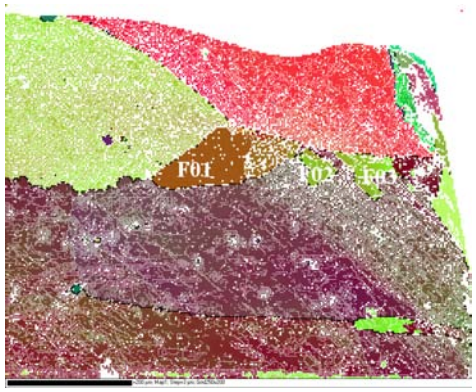

(d) After annealing at 320° for 10 minutes.

Figure A.6: EBSP sample F.

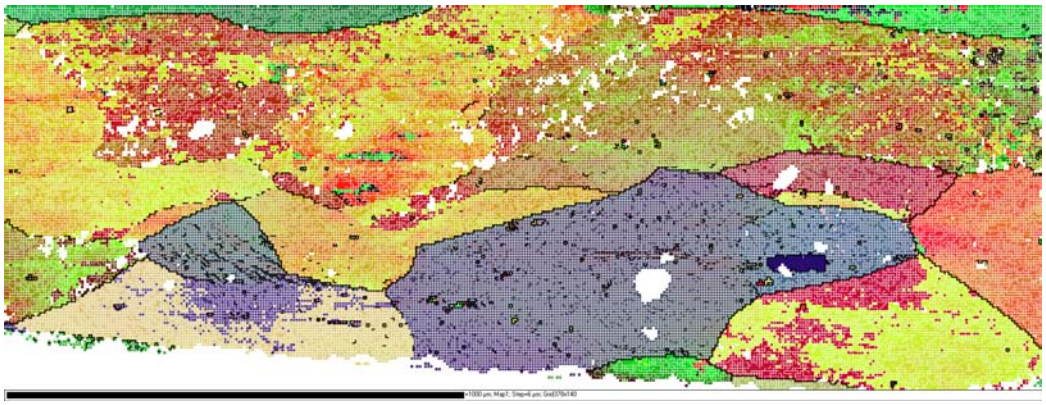

(a) Before annealing.

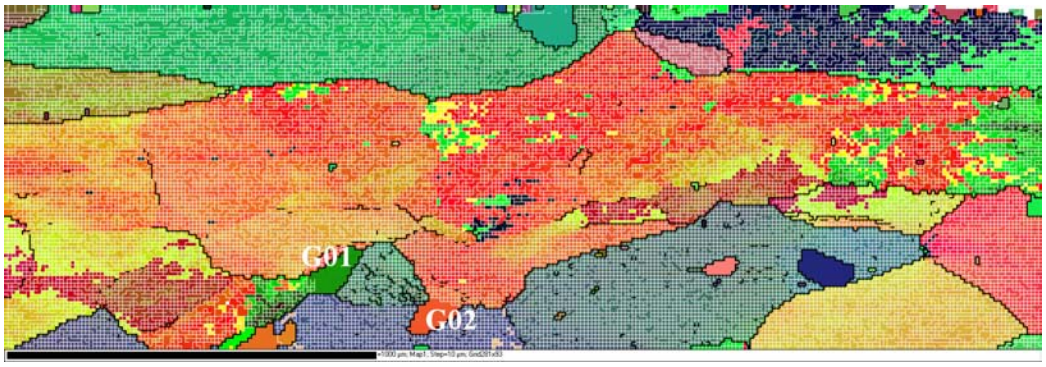

(b) After annealing at 320° for 15 minutes.

Figure A.7: EBSP sample G.

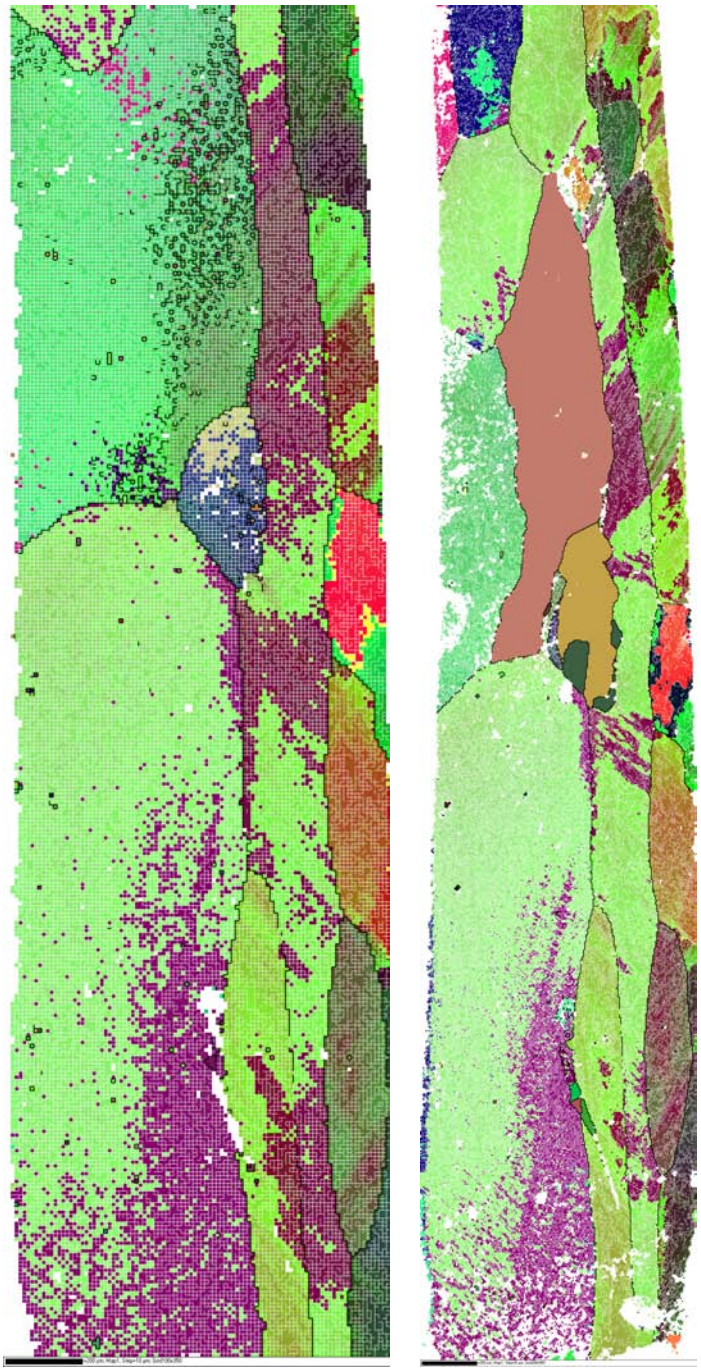

(a) Complete EBSP map one side of the 3DXRD sample before annealing. Compare with the gauge volume in figure 6.7(a).

(b) Complete EBSP map one side of the 3DXRD sample after annealing at 320° for 2 minutes. Compare with the gauge volume in figure 6.7(b).

Figure A.8: 3DXRD sample

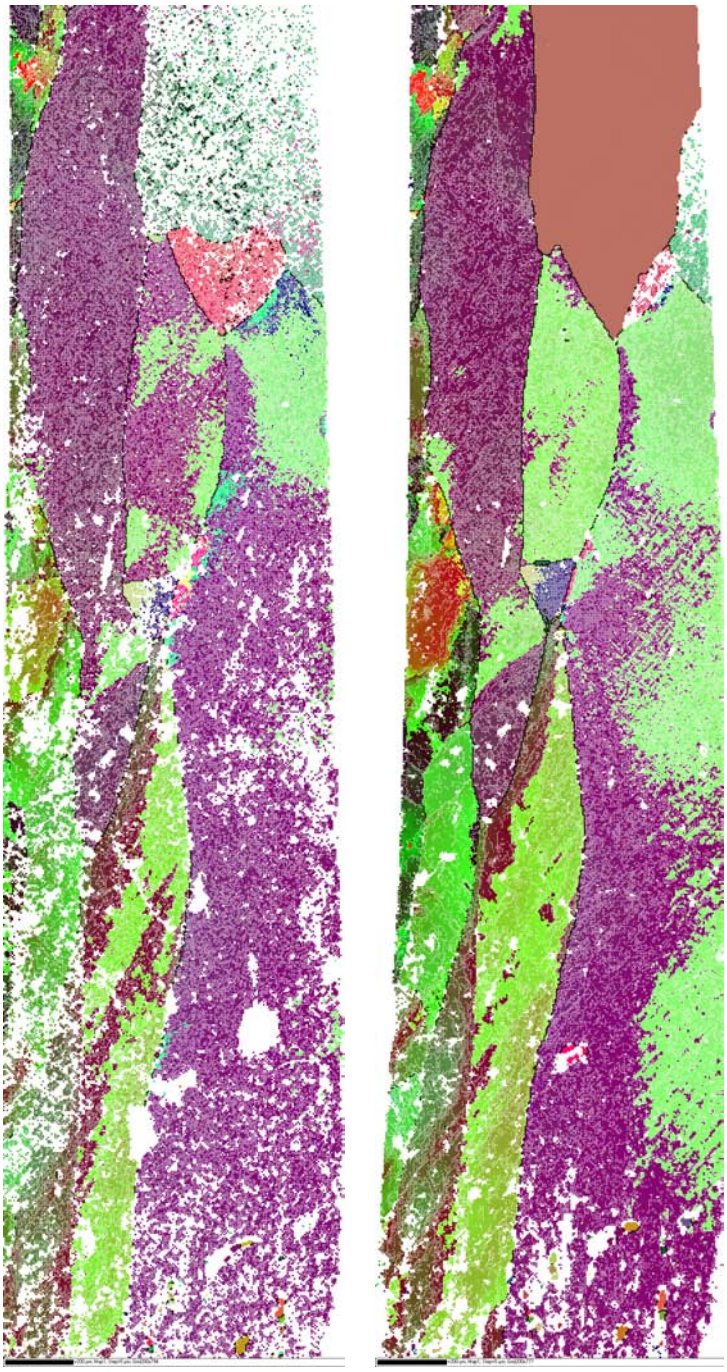

(a) Complete EBSP map one side of the 3DXRD sample before annealing. Compare with the gauge volume in figure 6.8(a).

(b) Complete EBSP map one side of the 3DXRD sample after annealing at 320° for 2 minutes. Compare with the gauge volume in figure 6.8(b).

Figure A.9: 3DXRD sample

Appendix B

Preliminary 3DXRD Experiment

As described in section 2.3, 3DXRD is a method capable of probing the bulk of crystalline materials. Therefore, the results seen on the surface with EBSP are well supplemented by experiments by X-ray diffraction.

The experiment described in this chapter allowed observation of a deformed sample before and after annealing to early recrystallization. The material used was identical to that used for the EBSP experiments described in chapter 4 and the 3DXRD experiment in chapter 5.

The aim of the experiment was to find the optimal way to observe nucleation of recrystallization in the bulk of a deformed aluminum sample. The desired results were the same as for the subsequent, more successful experiment of chapters 5 and 6; to map the deformed structure at nucleation sites before and after annealing to nucleation in order to do an analysis of the orientation relationship between the deformed structure and the nucleus. A special focus was nuclei with new orientations, and the 3DXRD method is ideal for finding these, as there will be no overlap of diffraction spots.

Two recrystallized grains were identified in the sample after annealing, but more appeared to be present. These grains had already grown quite large and appeared to have an orientation similar to a deformed grain, meaning that it was not meaningful to perform a detailed analysis of orientation relationships. Further, the mapping method focused on mapping specific areas around triple junctions before annealing and then mapping the entire sample cross section after nucleation turned out to be less efficient than expected. The experiment gave valuable insights into the limitations of the setup used and aided in the planning of the next experiment.

B.1 3DXRD setup

This experiment took place in July 2006, i.e. before the new experimental hutch was installed at beamline ID11 of the ESRF. This means that the setup used was slightly different from the present possibilities which were used for the second 3DXRD experiment described in chapter 5.

The sample, which had a cross section of 200μm×700μm, was mounted in the 3DXRD furnace in the beam. The mappings before and after annealing were made without the quartz tube, but between annealing steps, measurements were made with the quartz tube in place.

Two different detectors were used alternately; the Sensicam detector as a near-field detector at distances 2.5, 3.0 and 3.5 mm and the Frelon 2K as a far-field detector at distance 11.3 cm. For the Frelon detector, the pixels were digitally binned in such a was as to make the effective pixel area 4 times larger, i.e. giving an effective number of pixels of 1024×1024 in stead of 2048×2048.

The X-ray beam had an energy of 29.6 keV and was focused vertically using a bent Laue crystal. Two different beam configurations were used:

1 The beam was focussed to FWHM 12 μm in the vertical direction. Further, the beam was focussed horizontally to 300 μm using a second Laue crystal and then slit to 150 μm to ensure a homogeneous beam profile. This beam was used for local measurements around triple junctions in the deformed state.

2 The beam was focussed to FWHM 6 μm in the vertical direction. In the horizontal direction, the beam was left unfocussed and slit to 800 μm, which was the maximum width possible with a homogeneous beam profile. This beam width allowed illumination of the entire cross section of the sample at all rotations. This configuration was used for the final mapping og a coherent gauge volume of the sample after nucleation had occurred.

B.2 Experimental procedure

The sequence of the experiment was as follows:

- The sample was mapped by EBSP on one side with a step size of 10 μm.
- At the 3DXRD beamline, the sample was mounted in the furnace with TD parallel to the beam. The quartz tube was left off initially.

- Based on the positions of triple junctions seen on the surface of the sample by EBSP, the approximate positions of these triple junctions were found by scanning in the z direction with the narrow beam (configuration 1) using the far-field detector.
- The quartz tube was mounted on the furnace, and the sample was annealed in several steps at 315°C-320°C.
- A volume where recrystallization diffraction spots were seen was selected for mapping. This mapping was done using the far-field detector and the wide beam of configuration 2 (see above), covering the entire cross section of the sample.
- The same volume was mapped with the near-field detector using tracking at 3 different distances.
- After the experiment, the sample was mapped again by EBSP on both sides with a step size of 2 μm.

B.2.1 Detection limit

The detection limit was determined using a rolled aluminum foil with a thickness of 25 μm in a similar manner to what was described in section 5.4 for the second 3DXRD experiment. The foil was rotated from -45° to 45° in a single 20 second exposure with an attenuation factor of ~ 7.

The detection limit was calculated to be $ECD = 0.9\mu$m using the {220} Debye-Scherrer ring. There were two main reasons why the detection limit in this case was better than what was achieved in the second 3DXRD experiment. Firstly due to binning of the pixels and secondly because a smaller sample volume was being illuminated in each layer. This was due to the beam height and sample cross section. As the detection limit was in both cases limited by the dynamic range of the detector, a smaller maximum volume meant that smaller volumes could be detected without saturating the detector.

B.2.2 Mapping before annealing

The positions of triple junctions observed on the surface of the sample were used as a starting point to find the approximate location of triple junctions in the sample. This was done by taking a series of images with the same x, y and ω positions while moving the sample in the z direction and observing when the diffraction spots from the large deformed grains appeared or disappeared.

This was a quite elaborate process, as the grains in the sample were not columnar and the triple junctions thus did not necessarily go through the sample as seen on the surface.

A detailed mapping was performed around 10 triple junctions using an omega step size of 0.25° with 0.5 second exposures and scanning over [-22.5°:22.5°]. 15-16 layers spaced by 12 μm in height corresponding to the beam height were recorded for each triple junction.

B.2.3 Annealing

Before the experiment, several test annealings were carried out at Risø, determining that the optimal annealing temperature was between 315°C an 325°C.

After the initial mapping, the quartz tube was mounted and the furnace with the sample was heated to 315°C for 3 minutes. It was then decided that an annealing temperature of 320°C should be used, and the sample was annealed at this temperature for further 3,3,5 and 10 minutes, giving a total annealing time of 21 minutes at 320°C.

Between annealings, the sample was cooled to 170°C and a brief scan with the beam in configuration 2 and the far-field detector was performed in order to observe if any diffraction spots recognizable as nuclei appeared. When nuclei were seen, the sample was allowed to cool to room temperature, and the quartz tube was removed.

B.2.4 Mapping after annealing

After heating, a gauge volume containing 6 of the 10 triple junctions which had been mapped before annealing was selected. This gauge volume was mapped using the far-field detector and the wide beam configuration (2). 51 layers spaced by 6 μm in z were mapped using an ω step of 1°, an exposure time of 0.5 seconds and scanning the interval [-60°:60°].

A similar volume was then mapped using the near-field detector. With the same starting layer, 62 layers were mapped, giving a slightly larger gauge volume for the near-field mapping. This mapping was done using tracking, i.e. every third layer was probed 3 times with the detector at 3 different distances, namely 2.5, 3.0 and 3.5 mm. For each layer, images were recorded using an ω step of 1°, an exposure time of 12 seconds and scanning the intervals [-60°:-30°] and [30°:60°].

The much longer exposure time was necessary due to the lower efficiency of the near-field detector. Along with the tracking, this meant that the near-field mapping was considerably more time-consuming than the far-field

mapping. the far-field mapping took about 3 hours, while the near-field mapping took approximately 47 hours.

B.3 Results

B.3.1 Recrystallized grains

The data was analyzed to obtain the orientations of the undeformed nuclei in a different manner than for the data of the experiment in chapter 5, as the same software packages were not available at the time.

The diffraction spots originating from recrystallized material were harvested from the far-field detector data taken after annealing by caking of the Debye-Scherrer rings. The peaks appearing in only one of a series of consecutive images were selected and used as input for an earlier version of the program GrainSpotter.

Two rather large recrystallizing grains were found and their orientations indexed. These had grown so large that they could not rightly be called nuclei. The two grains had a misorientation to each other of 8°, and examination of the surfaces showed that one of them transversed the sample, appearing on both sides.

B.3.2 Orientations

A pole figure was reconstructed from caking of layer 7 of the far-field mapping. This pole figure can be seen in figure B.1, where the orientations of the two recrystallized grains identified in the layer are also marked. Figure B.2 shows the orientations observed on the two surfaces by EBSP in an area spanning approximately 10 layers around the position of layer 7, and good agreement with the orientations in the bulk is seen.

B.3.3 EBSP maps

The surfaces of the sample were mapped using EBSP after the experiment. The recrystallized grains that were identified in the 3DXRD data are marked as N1 and N2 in figures B.3(b) and B.4. Another recrystallized grain, N3, seen on the surface could not be indexed from the data, as it had an orientation very close to a deformed grain seen in the same layer, causing the spots to overlap.

Some internal deformation is visible in the recrystallized grains, particularly in figure B.4. Both N1 and N2 have orientations similar to the red

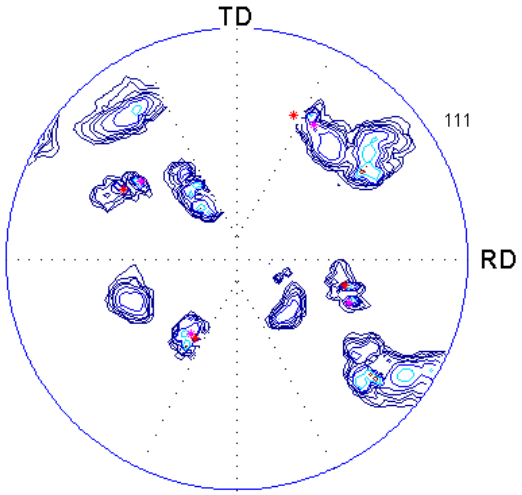

Figure B.1: Pole figure constructed by caking of the ⟨111⟩ Debye-Scherrer ring in the diffraction images of layer 7 of the far-field mapping. The areas without contour lines close to TD correspond to rotations ω which were not imaged. The magenta and red stars indicate the orientations of the two recrystallized grains that have been found using GrainSpottter.

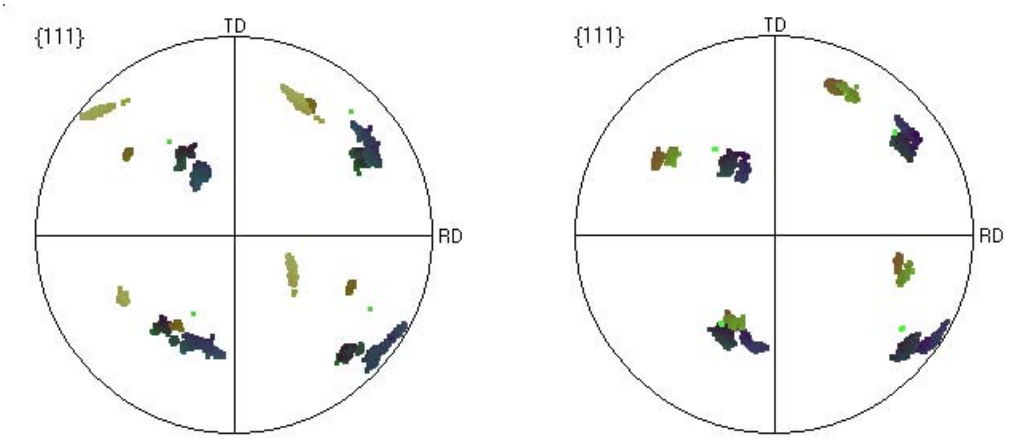

(a) Pole figure of the orientations within the area marked in figure B.3(b).

(b) Pole figure of the orientations within the area marked in figure B.4.

Figure B.2: Pole figures of the EBSP data from the two sides of the sample after annealing. The colors correspond to the colors on the maps.

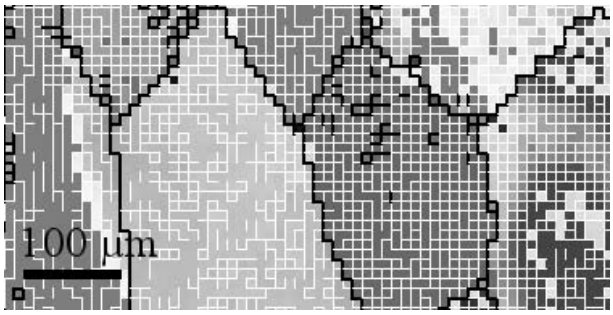

(a) EBSP map before annealing with step size 10 μm.

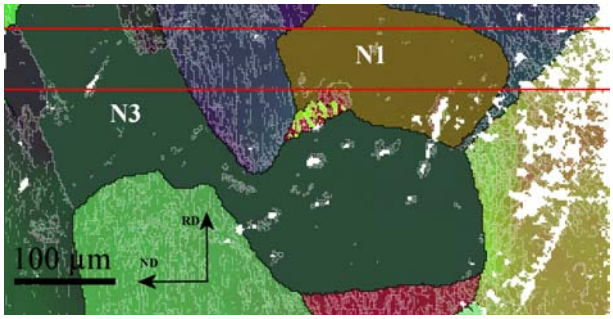

(b) EBSP map after annealing with step size 2 μm.

Figure B.3: EBSP maps of the RD-ND surface of the gauge volume mapped by 3DXRD. The red lines in (b) indicate an area of about 10 layers centered on the approximate location of layer 7. This is the area used to produce the pole figure in figure B.2(a).

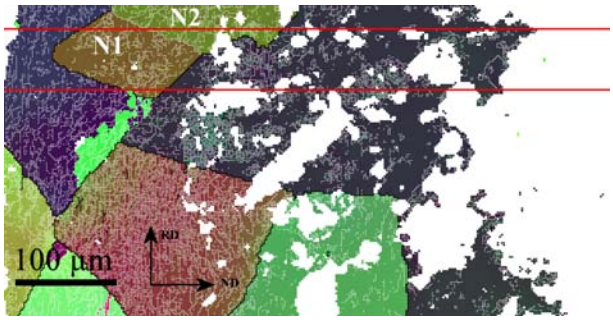

Figure B.4: EBSP map after annealing with step size 2 μm. The map shows the opposite side of the sample compared to figure B.3. This side was not mapped before annealing and was not as thoroughly mechanically polished, giving more noise.

deformed grain. Although there seems to be no direct connection between the recrystallized grains and this deformed grain in the figure, comparison with the EBSP map before annealing (figure B.3(a)) shows that this grain extended to the position of N1 and N2 before annealing, but was partially consumed by N3.

Observation of the diffraction images revealed that the orientations of N1 and N2 were present with an intensity close to the detection limit in several layers below the position of the recrystallized grains. In lower layers, much more broadened diffraction spots of a deformed grain of a similar orientation were seen. This indicates that N2 and N2 may have nucleated from this deformed grain, but was later severed from it after nucleation. The low-intensity presence in the layers between the two was likely due to tails on the beam.

The two recrystallizing grains identified were most likely nucleated by the SIBM mechanism. After the annealing, they were no longer connected to their parent grain, but their rather high internal misorientations also fit well with the observations of parent-oriented nuclei observed in the EBSP experiments in chapter 4.

B.3.4 Volumes

Both of the two recrystallizing grains N1 and N2 extended outside the gauge volume. Their volumes in each layer were calculated in a similar manner as was done in chapter 6. The volumes were not calibrated to the reference scan, so only relative volumes were found. Figure B.5 shows the volumes in the first 16 layers. Below this, a deformed grain of a similar orientation was present with a very small volume.

B.3.5 Other nuclei

Inspection of the diffraction images showed other spot-like diffraction spots, some of them very small. The analysis method used was not able to index the orientations giving rise to these.

B.4 Experiences gained

This experiment was not able to give information of the orientation relationships between nuclei of new orientations and the deformed structure, as no nuclei of new orientations were found. However, some important lessons were

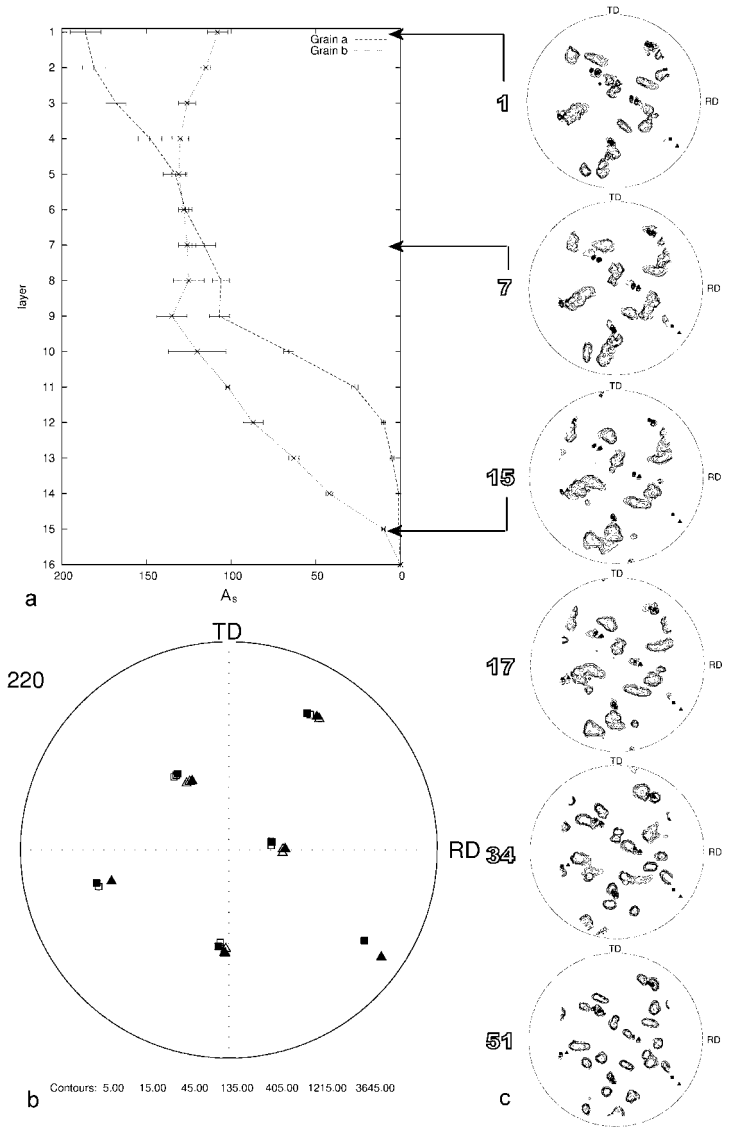

Figure B.5: (a): Area of the parts of the two grains that are inside the beam for the first 16 layers. Although both grains are present in the same layers, the difference in area shows that two separate grains are observed. (b): {220} pole figure representing the diffraction spots (open symbols) and the fitted orientations (filled symbols) of the two new grains. These points are also overlaid on (c): The {220} pole figures for some of the layers with the layer numbers to the left of the pole figures, illustrating the difference between the narrow spots of the recrystallized grains and the broader peaks of the deformed structure (from [113]).

learned, giving improvements for the second experiment described in chapter 5.

As mentioned, diffraction spots from other smaller nuclei were also observed in the diffraction images and pole figures, but could not be orientation indexed. This was partially because of the software available at the time, which was not designed for this purpose. E.g. the harvesting procedure for recrystallized diffraction spots was not ideal. Another reason for the failure to index all diffraction spots was the angular resolution of the mapping after annealing, where a 1° step in ω was seen not to be precise enough.

Binning was used on the diffraction images. This reduced the noise level, but gave a lower resolution on the position of the diffraction spots, which affected the precision of the orientation indexing. If the positions of grains inside the sample were to be fitted from the data, the binning would also have reduced the precision of the position fit, but no positions were fitted from these data.

At the time of this experiment, the GrainSweeper software for reconstruction of deformed material did not exist. Therefore, no direct comparison could be made of recrystallized orientations and parent orientations at the nucleation sites. However, as the only two recrystallized grains found from the 3DXRD data had a clear parent orientation, such a comparison would not have been relevant. Therefore, the data recorded with the near-field detector which would have been able to give the positions of the nuclei was not analyzed.

Overall, the main points requiring improvement were:

- A finer step size in ω was needed to find all nuclei and their orientations.
- Mapping with a narrow beam around triple junctions before annealing was much too complicated and the results were not directly comparable with the results after annealing. Mapping the entire cross section of the sample before and after annealing was therefore a better solution, although more time-consuming.
- Mounting and removing the quartz tube for annealing meant that recalibration of all positions were necessary, and still gave som uncertainty on positions between mappings. Although this gave less diffuse scattering, an entire experiment performed without touching the sample might be preferable.

Apart from these, a wider beam

Appendix C

Authored publications

A1 S.S. West, G. Winther, L. Margulies, E. Knudsen, H.O. Sørensen, S. Schmidt and D. Juul Jensen: *Mapping partially recrystallized structures by 3DXRD*, Materials Science Forum **558-559**, pp. 389-394, (2007).

A2 S.S. West, S. Schmidt and D. Juul Jensen: *Experimental quantification of nucleation*, Proceedings of the 29th Risø International Symposium on Materials Science, pp. 383-389, (2008).

A3 S. S. West, S. Schmidt og D. Juul Jensen: *Kimdannelse ved rekrystallisation studeret med EBSP og 3DXRD*, Dansk Metallurgisk Selskabs Årsmøde, (2009). (Annual meeting of the Danish metallurgical Society)

A4 S.S. West, G. Winther and D. Juul Jensen: *Analysis of orientation relations between deformed grains and recrystallization nuclei*, Submitted to: Metallurgical and Materials Transactions A (Physical Metallurgy and Materials Science), (2009).

A5 S.S. West, S. Schmidt, H.O. Sørensen, G. Winther, H. F. Poulsen, L. Margulies, C. Gundlach and D. Juul Jensen: *Direct non-destructive observation of bulk nucleation in 30% deformed aluminum*, submitted to Scripta Materialia (2009).

A1 Mapping partially recrystallized structures by 3DXRD

S.S. West, G. Winther, L. Margulies, E. Knudsen, H.O. Sørensen, S. Schmidt and D. Juul Jensen, Materials Science Forum **558-559**, pp. 389-394, (2007).

Materials Science Forum Vols. 558-559 (2007) pp. 389-394
online at http://www.scientific.net

Mapping partially recrystallised structures by 3DXRD

S. S. West[1,a], G. Winther[1,b], L. Margulies[1,2,c], E. Knudsen[1,d], H. O. Sørensen[1,e], S. Schmidt[1,f] and D. Juul Jensen[1,g]

[1]Risø National Laboratory, 4000 Roskilde, Denmark
[2]ESRF, 6 Rue Jules Horowitz, BP220, 38043 Grenoble Cedex, France
[a]stine.west@risoe.dk,
[b]grethe.winther@risoe.dk,
[c]margulies@esrf.fr,
[d]erik.knudsen@risoe.dk,
[e]henning.sorensen@risoe.dk,
[f]soeren.schmidt@risoe.dk,
[g]dorte.juul.jensen@risoe.dk

Keywords: 3DXRD, partially recrystallised structures, 5D maps.

Abstract. A partially recrystallised sample has been characterised by 3DXRD. A gauge volume of 200µm × 700µm × 300µm has been fully mapped. Deformed and recrystallised regions within the selected gauge volume are distinguished based on the sharpness of the diffraction spots. Information corresponding to a 5D (Φ_1, Φ, Φ_2, z, $x \cdot y$) map is deducted from the 3DXRD data.

Introduction

During recrystallisation the new grains expand in the 3 spatial dimensions, meaning that this process is inherently difficult to characterise by surface studies. By serial sectioning and Electron Backscattered Diffraction Patterns (EBSP) maps of the structure may be constructed. However, this destroys the sample so that the dynamics of the process cannot be studied at the level of individual grains.

The 3-Dimensional X-Ray Diffraction (3DXRD) method [1,2] developed by Risø in collaboration with the European Synchrotron Radiation Facility has the potential to map the grain structure non-destructively, thus enabling characterisation before, during and after annealing. The number of parameters - or dimensions - included in the maps may vary. The goal is 7D maps, which display the 3 parameters describing the crystallographic orientation (Φ_1, Φ, Φ_2) as a function of the 3 spatial parameters (x, y, z) and can follow the evolution of these 6 parameters with time. 6D maps have been demonstrated for fully recrystallised materials [3]. In the case of deformed structures the internal deformation induced orientation spread in the grains greatly complicates the analysis as the diffraction spots become broad and start to overlap.

The present paper presents mapping of a partially recrystallised structure in coarse grained aluminium of high purity.

The total dimensionality of the map is 5D, counting the 3D from the crystallographic orientations and 2D from the spatial information in the form of area fractions along one sample axis.

Experiments

To facilitate the construction of the map, a rather large grain size was required as well as suitable triple junctions for inducing nucleation and recrystallisation of new grains [4,5,6].

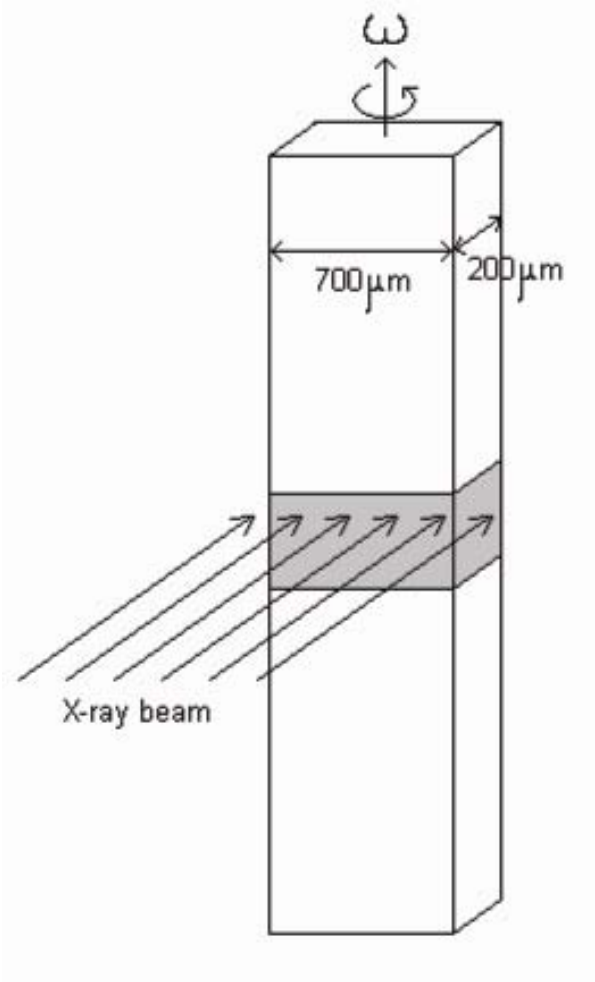

(a) The 3DXRD setup. The grey area marks the volume studied by 3DXRD.

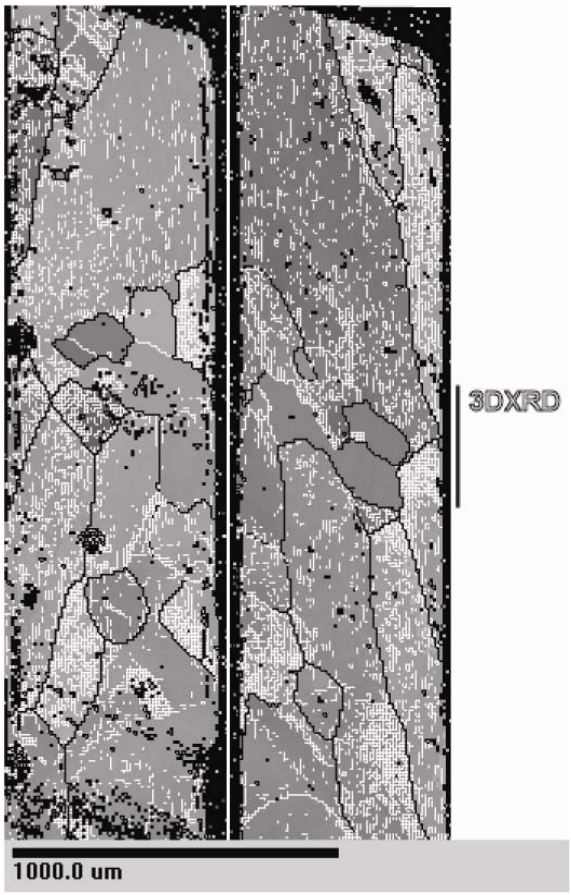

(b) EBSP of the sample after annealing. The region studied by 3DXRD is marked. The non-horizontal top is caused by a slight drift in the SEM during the EBSP data taking.

.Figure 1: Sketch of the 3DXRD setup and EBSPs of the two sides of the sample after the experiment. The white lines in the EBSPs correspond to a misorientation of >2°, while the black lines correspond to a misorientation of >15°.

The material for this study was 99.996% pure aluminium with initial grain sizes in the range 100-1000µm and an average grain size of 470µm.

The material was deformed by cold rolling to 30% reduction to produce sufficient stored energy to initiate nucleation, while still leaving the original grains recognisable in EBSP and by 3DXRD. A lath-shaped sample was spark cut with the geometry shown in Fig. 1 and electropolished.

From several prepared samples, a sample was chosen that had several well-defined triple junctions visible on the surface. For the 3DXRD experiment, the sample was mounted in a tube furnace in the beam at beamline ID11 at the ESRF synchrotron radiation facility in France with the transverse direction (TD) along the vertical axis (see Fig. 1(a)). The beam was monochromatic with an energy of 29.6 keV and was focused vertically to 6 µm. Horizontally, the beam was slit to 800 µm to ensure that the entire cross section of the sample was always illuminated by the beam during measurements which require rotations around the vertical axis.

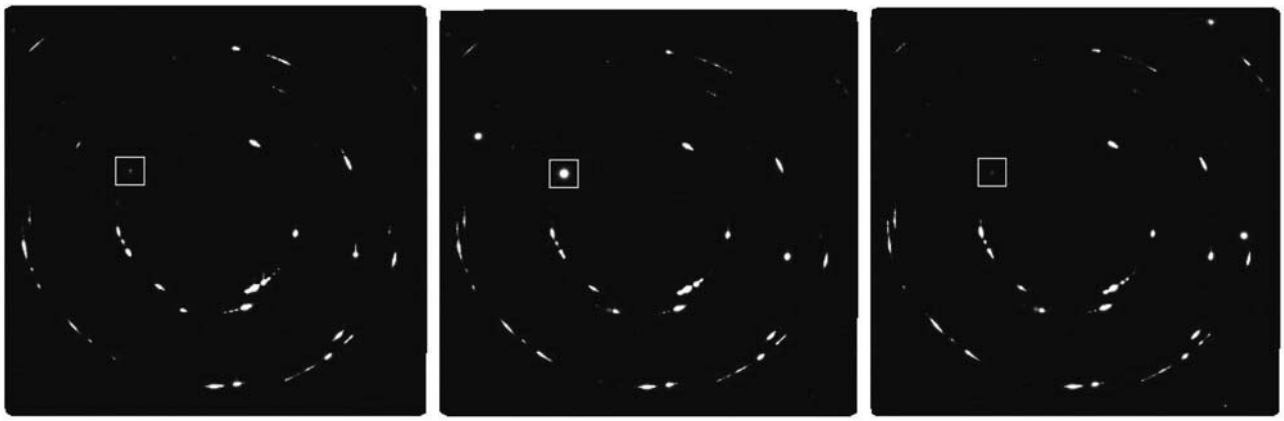

(a) ω =-44.5° (b) ω =-43.5° (c) ω =-42.5°

Figure 2: Data images with background subtracted. The box marks a diffraction spot from a new grain on the {111}-ring. The spot is not visible in the neighbouring images at ω=± 1°, showing that the diffracting crystal has very little internal misorientation. The deformed structure shows as peaks with a much larger extent along the rings as well as through several images.

The sample was annealed at 320° C in several steps to a total of 21 minutes in a protected argon atmosphere.

Diffraction data were obtained for a gauge volume of 51 layers spaced at 6 μm with the Frelon CCD-detector. For each layer, the sample was rotated around the vertical axis, and images were obtained in the ω-range -60° to 60° with a 1° spacing.

After the X-ray experiment the annealed sample was characterized by EBSP. The measurements show that the selected gauge volume contains both recrystallised and deformed grains, i.e. grains with very little or extensive internal orientation spread, respectively. The EBSP characterisation was carried out without any further polishing, as the argon atmosphere in the furnace left the surface pristine. The EBSP maps for the front and back faces of the sample are shown in Fig.1(b), and the approximate position of the volume selected for characterisation by 3DXRD is marked. Although the sample is quite thin, it is seen that the grains are not columnar.

Results and Discussion

Fig.2 shows examples of X-ray diffraction images of the annealed sample with the background subtracted by the method developed by Bowen et al. [8]. The images are from the same sample layer at neighbouring rotation angles ω. A sharp circular diffraction spot is seen on the innermost Debye-Scherrer ring at ω=-43.5°, corresponding to a reflection from a {111} plane. This spot does not appear in the neighbouring images at ω ± 1°, indicating that the diffracting crystal has very little internal misorientation, i.e. it is recrystallised. The broader spots also appear in several neighbouring images and originate from deformed grains.

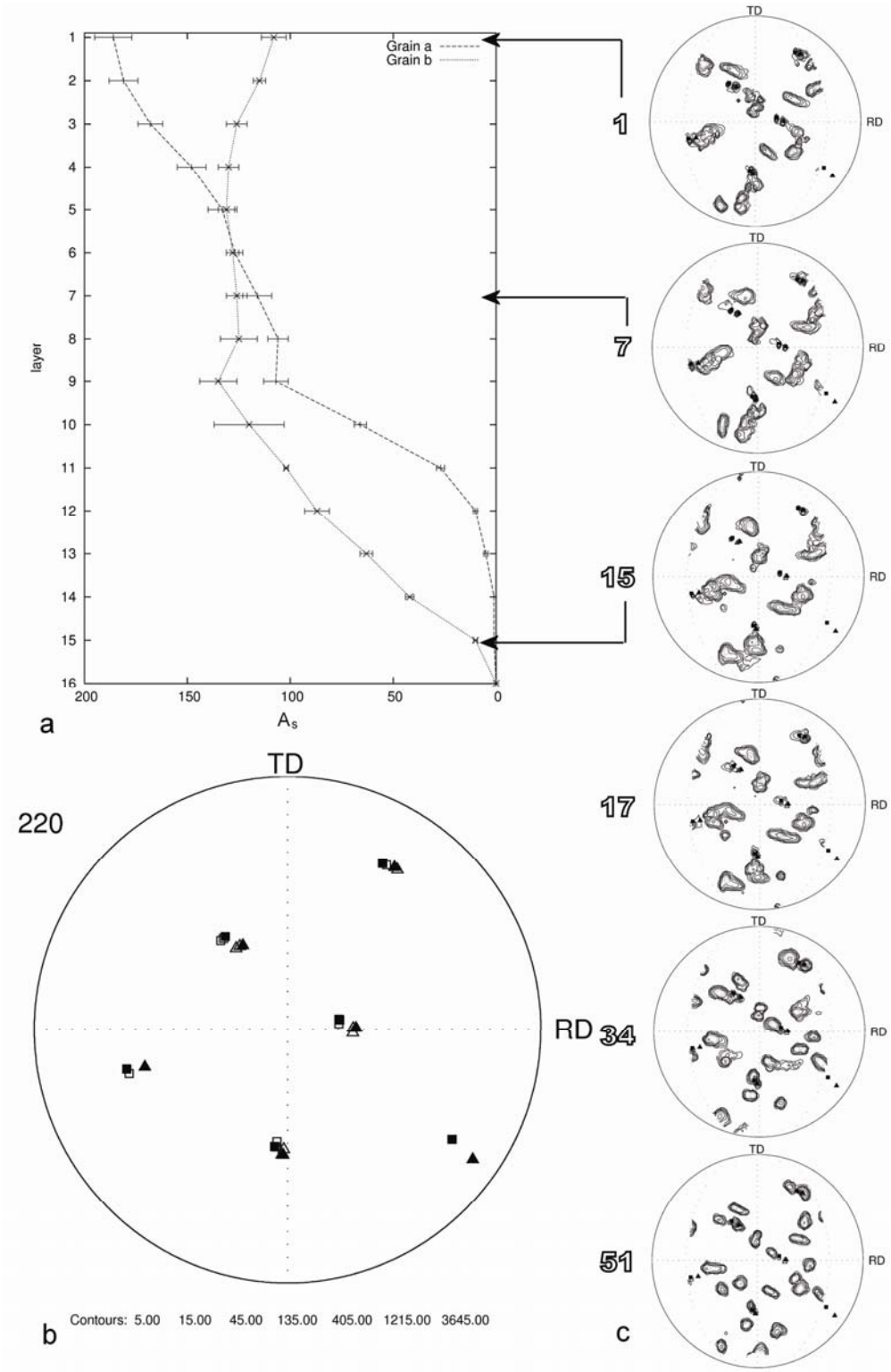

Figure 3: (a): Area of the parts of the two grains that are inside the beam for the first 16 layers. Although both grains are present in the same layers, the difference in area shows that two separate grains are observed. (b): {220} pole figure representing the diffraction spots (open symbols) and the fitted orientations (filled symbols) of the two new grains. These points are also overlaid on (c): The {220} pole figures for some of the layers with the layer numbers to the left of the pole figures, illustrating the difference between the narrow spots of the recrystallised grains and the broader peaks of the deformed structure.

From the ω range of detector images from a given layer (as the ones shown in Fig.2) a pole figure can be constructed for each Debye-Scherrer ring visible. Examples of {220} pole figures for different layers are shown in Fig.3(c). In the pole figures, the deformed grains are seen as broad peaks, while new recrystallising grains show up as more isolated intense spots. By indexing, several

diffraction spots can be linked together to represent the orientation of a grain. From the diffraction spots present in the 7th layer, two new recrystallised grains have been indexed. These grains are also present in other layers above and below layer 7.

Superimposed on the pole figure are the positions of the recrystallised diffraction spots found from the experimental data and a best fit to the orientations of these two grains. The orientations have been obtained using the GrainSpotter indexing software we have recently developed. The two fitted grain orientations have been obtained from 13 different diffraction spots each, from the rings {111}, {200} and {220}, and the fitted orientations match all of these spots to within approximately 2° (see figure 3(b)).

Each layer has a thickness of 6 µm, and the volume of the grains inside this layer can be calculated from the intensity of the diffraction spots. Due to the large size of the grains, this volume corresponds to an area times the thickness, i.e. $V \alpha A \cdot 6$ µm.

Fig.3(a) shows the relative areas of the two grains throughout the first 16 layers. The area is calculated by:

$$A = k \cdot \frac{I \cdot \sin(2\theta) \,|\, \sin(\eta) \,|}{|\, F_{hkl} \,|^2} \tag{1}$$

where I is the measured integrated intensity of a diffraction spot and $|F_{hkl}|$ is the structure factor. As the constant k is unknown, only the relative areas A_s are found, where $A=k \cdot A_s$. The volumes shown in the figure are averages over all {111}-reflections (3 for grain *a* and 4 for grain *b*).
Both of the two grains are present in the 16 first layers, corresponding to approximately 100µm, but whereas grain b has its maximum area $A_{s,max,b}$ in layer 1, grain a has its maximum value in layer 9 with $A_{s,max,a} \sim 75\ \% \ A_{s,max,b}$, proving clearly that although the grains are close in orientation (see Fig 3, they are not identical.

The deformed material in the layers below the new grains show the presence of an orientation similar to that of the two new grains, though it is unclear whether the new grains are physically connected to this part of the deformed matrix.

Conclusions and Outlook
A method has been demonstrated for non-destructive mapping of a partially-recrystallised polycrystalline sample. The orientations of two new recrystallising grains have been found as well as the volume profile of these grains in the *z* direction.

By indexing the X-ray diffraction spots in the data, the orientation of these two newly-nucleated grains have been found, and they are shown to have a small misorientation to each other. The mapping of the area of these grains through the sample indicate that the size and shape of the two grains is different although the position within the beam plane has yet to be determined. This constitutes a 5D map of the new grains.
Diffraction spots have been seen in other layers, indicating other recrystallising grains. The present method will be used to obtain orientations of all these new grains in the gauge volume and produce a 3-dimensional map of their spatial distribution as well
as the distribution of the deformed structure.

The deformed grains are isolated in orientation space, allowing the same indexing method to be used for determining their orientations and, by integrating the intensity, their relative areas throughout the layers.

The 3D position of the grains inside the sample cannot be resolved from the data presented here. However, additional data was taken with a high-resolution Sensicam detector at several distances close to the sample. This enables 3-dimensional reconstruction of the sample, which is planned as the next step in the data analysis.

Acknowledgements
The authors gratefully acknowledge the Danish National Research Foundation for supporting the Center for Fundamental Research: Metal Structures in Four Dimensions, within which this work was performed.

References

[1] H. F. Poulsen *Three-Dimensional X-Ray Diffraction Microscopy* (Springer, 2004)
[2] H. F. Poulsen, S. Garbe, T. Lorentzen, D. Juul Jensen, F. W. Poulsen, N. H. Andersen, T. Frello, R. Feidenhans'l and H. Graafsma: J. of Synchr. Rad. 4 (1997) 147-154
[3] K. Hannesson and D. Juul Jensen: these proceedings
[4] R. A. Vandermeer, P. Gordon: Trans. Metall. Soc. AIME (1959) 577-588
[5] T. J. Sabin, G. Winther, D. Juul Jensen: Acta Mat. 51 (2003) 3999-4011
[6] A. W. Larsen, H. F. Poulsen, L. Margulies, C. Gundlach, Q. Xing, X Huang, D. Juul Jensen: Scripta Mat. 53 (2005) 553-557
[7] H. F. Poulsen, E. M. Lauridsen, S. Schmidt, L. Margulies, J. H. Driver: Acta Mat. 51 (2003) 2517-2529
[8] J. R. Bowen, E. M. Lauridsen, J. Teuber: submitted (2006)

A2 Experimental quantification of nucleation

S.S. West, S. Schmidt and D. Juul Jensen, Proceedings of the 29th Risø International Symposium on Materials Science, pp. 383-389, (2008).

EXPERIMENTAL QUANTIFICATION OF NUCLEATION

S. S. West, S. Schmidt and D. Juul Jensen

Center for Fundamental Research: Metal Structures in Four Dimensions, Material Science Department,
Risø DTU, 4000 Roskilde, Denmark

ABSTRACT

The present work presents a study of nucleation of recrystallisation. Nucleation is important for the understanding of the formation of the microstructure of metals, which is of interest in order to produce lighter and stronger metals to reduce energy expenditure.

The work falls in two parts; the first is a surface investigation by electron backscattered diffraction patterns (EBSP) which shows orientation relationships between the deformed matrix and the nuclei. The second part proposes an experiment by 3-dimensional X-ray diffraction (3DXRD) which will map a gauge volume of 600μm×1000μm×700μm before and after annealing to form nuclei in order to investigate the orientations present at the nucleation sites before and after nucleation.

1. INTRODUCTION

When thinking about energy materials, the first thought may be on materials which help producing energy, like materials for wind turbine blades or for power plant tanks and tubings. As most of the papers in these proceedings illustrate there is a big need for research improving existing materials or finding new solutions for these “energy producing materials”. Another class of materials may however be equally important, namely materials which can contribute to energy savings. Here a classic example is lighter and stronger materials. For metals, thermomechanical processing is a tool for tailoring properties and thus for making light and strong components.

The present paper deals with thermomechanical processing of the lightweight metal aluminium and focuses on nucleation of recrystallization. When a deformed metal is recrystallized, nuclei which are almost strain-free small perfect crystals develop locally in the deformed structure and grow driven by the energy stored in the deformed materials (Doherty, Hughes, Humphreys,

Jonas, Juul Jensen, Kassner, King, McNelley, McQueen, and Rollett 1997). The nucleation process is extremely difficult to quantify experimentally because the nuclei are few in number (like looking for a needle in a haystack) and as soon as a nucleus has formed, one can not quantify what was there at that site before annealing and thus what mechanism led to the formation of exactly that nucleus. This latter problem has been referred to as the problem of the lost evidence (Duggan 1996). It is well accepted that nuclei form primarily at deformation inhomogeneities associated with high stored energy, e.g. near 2^{nd} phase particles, along grain boundaries and at triple junctions (e.g. Doherty et al. 1997), however it is not known where along the triple junction or grain boundary or at which particles nuclei will form.

Also it is not known which crystallographic orientation the nuclei will have. The most accepted view is that the nuclei will have the same crystallographic orientation as was there at that site in the deformed condition (e.g. Humphreys and Arkadani 1994) and for example the strain induced boundary migration (SIBM) nucleation mechanism (Beck and Sperry 1950) will give nuclei with such "old orientations". However it has also been observed that some nuclei may form with orientations that could not be found in the deformed matrix (Sabin, Winther, and Juul Jensen 2003, Larsen, Poulsen, Margulies, Gundlach, Xing, Huang, and Juul Jensen 2005, Wu and Juul Jensen 2007).

The aim of the present work is to study nucleation in-situ and focus on orientation relationships between the individual nuclei and the deformed state at the nucleation sites. To simplify the investigation, weakly deformed pure aluminium is chosen because preferential nucleation along triple junction lines is expected in such a sample (Vandermeer and Gordon 1959). The experimental investigation is done by electron backscattering pattern (EBSP) analysis of a series of samples in the deformed state and after annealing. Exactly the same sample areas were characterized allowing a direct investigation of orientation relationships. This EBSP method is relatively easy to use but does only allow direct observation at the surface of the sample. To overcome this limitation previously also 3 dimensional high energy X-ray diffraction (3DXRD) has been used on similar samples (Larsen et al. 2005). However the 3DXRD method used in that investigation turned out to be very difficult to analyze and in the present paper an improved 3DXRD method is suggested.

2. 2-DIMENSIONAL INVESTIGATIONS

2.1 Experimental. A series of samples were prepared from 99.996% pure aluminium with an average grain size of approximately 500μm which had been deformed to 30% reduction by cold rolling. Samples were prepared with a square tip of 1×6mm and were mechanically polished to a thickness of 0.6mm and then electropolished on both sides. This geometry is needed for the 3DXRD experiment while still allowing investigation by EBSP on two sides of the specimen. These samples were then examined by EBSP before and after annealing at temperatures between 588K and 598K (315°C and 325°C) for different periods of time to determine the ideal conditions for examining nucleation of recrystallisation. Due to the large grain sizes, the samples turned out to be very inhomogeneous in their nucleation behaviour. While some samples did not nucleate at all, nuclei had already grown to become very large in other samples given the same annealing time and temperature. The heat treatment was done in a tube furnace where the sample was in thermal contact with a heated copper rod. The furnace contained a protected argon atmosphere and the temperature was increased from room temperature to annealing temperature over a period of 10 minutes. The sample was allowed to cool in the furnace with an initial cooling rate of about 25K/minute.

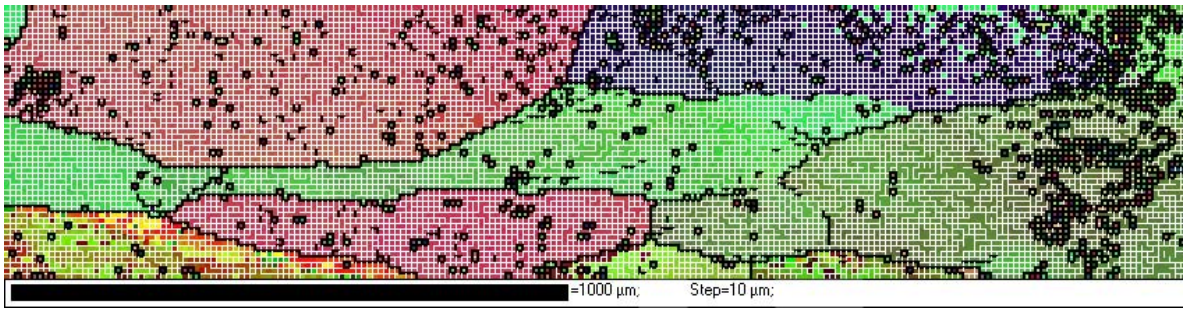

(a)

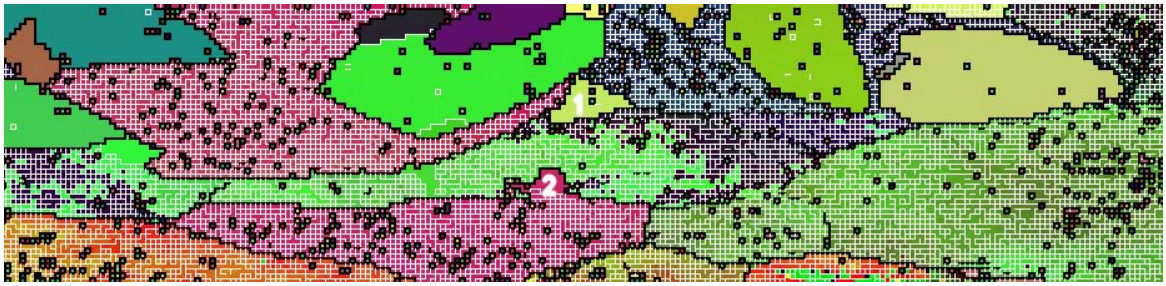

(b)

Fig.1. EBSP maps of a sample (a) before annealing (b) after annealing. White lines correspond to minimum 1° misorientation, while black lines correspond to minimum 10° misorientation. The step size is 10µm.

The microstructure was characterised by EBSP before and after annealing in a JEOL 840 scanning electron microscope with a step size of 10µm, and maps were constructed (Fig. 1).

2.2. Results and discussion. Fig. 1 shows EBSP maps of a sample before and after annealing at 588K (315°C) for 15 minutes. The maps reveal that recrystallisation has begun in the sample and several nuclei have already grown to very large sizes. The two nuclei marked 1 and 2 in Fig.1 were selected for further study because they are still relatively small. Nucleus 1 appeared at a triple junction between three deformed grains, while nucleus 2 appeared at a grain boundary between two deformed grains. This agrees well with the general view of grain boundaries and triple junctions as potential nucleation sites (Doherty et al. 1997).

The maps also contain some pixels which have most probably been mis-indexed. Where most of the correctly indexed pixels have orientations found from 7 or 8 bands in the Kikuchi patterns, there are also pixels where the orientation has been estimated from as few as 2 or 3 bands. These orientations are generally not correct and appear as pixels of different colouring than the neighbouring pixels, surrounded by black (>10° misorientation) lines.

Fig. 2 shows an enlargement of the triple junction where nucleus 1 appeared before and after annealing. A yellow square on the grain boundary shows where a single pixel was present before annealing with the same orientation as nucleus 1 has after the annealing. This single pixel (10×10µm) was indexed from 5 Kikuchi bands and the orientation is thus slightly dubious. However, this poor quality of the Kikuchi pattern could be related to a small diffracting area, so there might have been a small area <10µm in the deformed microstructure near the triple junction which had the orientation of nucleus 1.

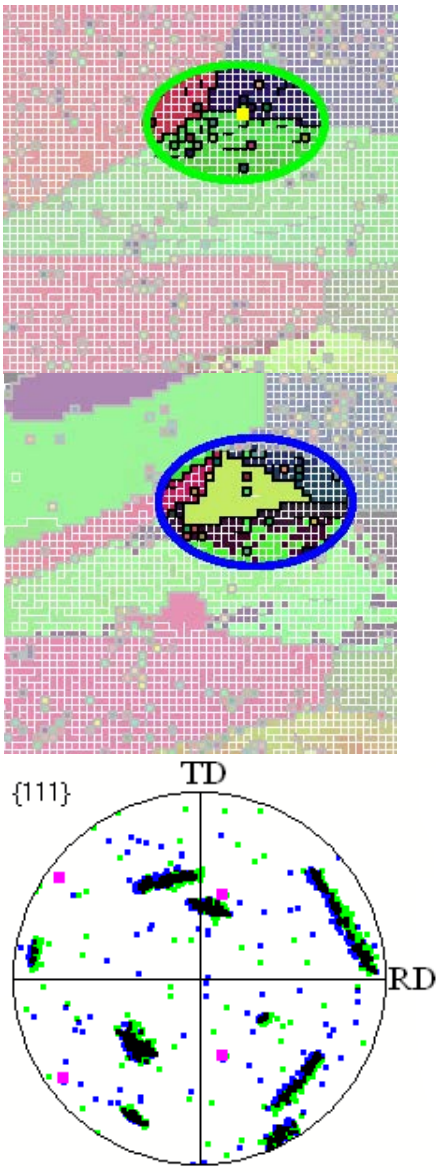

Fig.2. Top: EBSP maps before and after annealing of the area where nucleus 1 appeared. The yellow square marks a pixel with the same orientation as the nucleus. Bottom: {111} pole figure of the areas marked by ellipses in the EBSP maps. Green points mark the orientations before annealing, while blue points mark the orientations after annealing. Apart from a small rotation due to a slight misalignment of the sample between the two mappings, the orientations fall within the same areas. The nucleus orientation is marked by magenta squares. It can be seen that it falls almost exactly on top of a single green point.

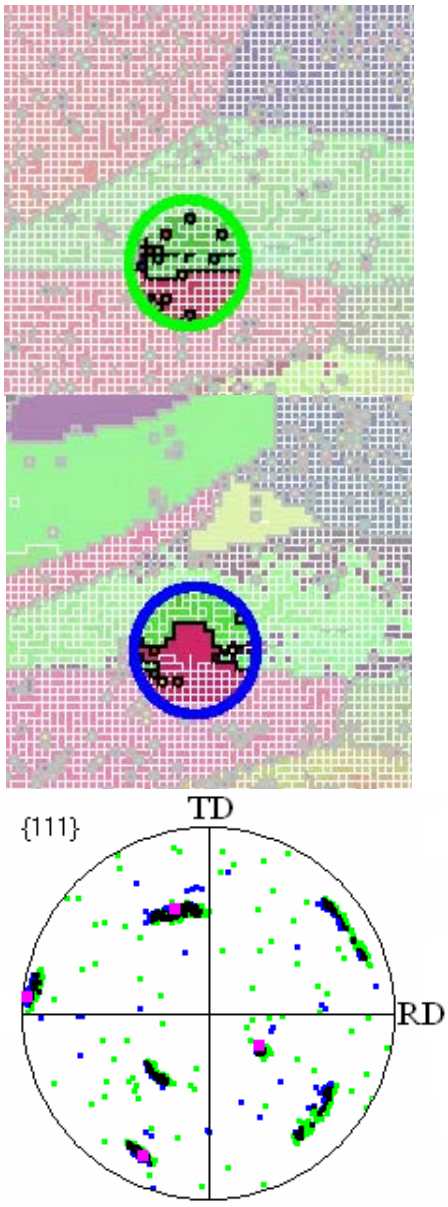

Fig.3. As Fig. 2 for nucleus 2. Here the nucleus has an orientation identical to one of the parent grains, as can be seen by the fact that the magenta squares fall on top of an ensemble of green points corresponding to a major component in the deformed state.

Nucleus 2 has the same orientation as one of the parent grains and is an example of strain-induced boundary migration. Fig. 3 shows the enlarged map of the nucleating area before and after annealing as well as pole figures of a small circular area around the nucleus.

The two nuclei shown here both have orientations already present in the deformed state before annealing. Other nuclei have been seen with new orientations (e.g. Wu et al. 2005). But because EBSP is a surface method, it can never be conclusively proven that a small volume with the nucleus orientation was not present. As EBSP only samples approximately 10nm below the surface, such a volume could easily be present close to the surface and still remain undetected.

To conclusively determine if new orientations can appear, the sample must be examined in three dimensions before and after the annealing with a resolution smaller than the size of the smallest possible element in the deformation microstructure which can develop into a viable nucleus.

3. OUTLOOK

3-dimensional X-ray diffraction (3DXRD) is a method for studying the bulk of crystalline samples non-destructively. By using high-energy X-ray diffraction and scanning the sample for different rotations, a 3D map of a recrystallised sample can be produced (Fu, Poulsen, Schmidt, Nielsen, Lauridsen, and Juul Jensen 2003). This method has also been shown by simulation to be feasible for lightly deformed material (Rodek, Poulsen, Knudsen and Herman 2007). Because the method is based on orientation indexing from diffraction spots, the method is especially well suited for finding new orientations, as these will give diffraction spots separated from the large diffraction spots caused by the mosaicity of the original grains in the deformed sample.

A previous 3DXRD experiment found only very few nuclei (Larsen et al. 2005). A new and improved experimental setup has therefore been devised.

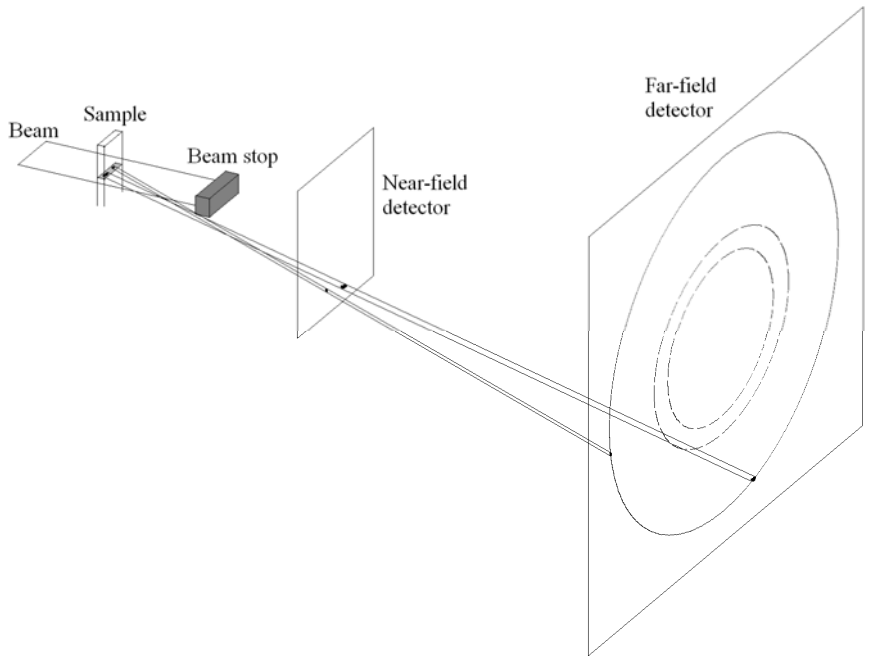

Fig. 4. Setup with 2 detectors. On the far-field detector, diffraction spots will gather on Debye-Scherrer rings depending on the distance between atomic planes. On the near-field detector however, the position and shape of diffraction spots on the detector also reveal the position and shape of the diffracting grains inside the sample.

3.1 3DXRD experimental method. For the experiment, a sample similar to the ones used in the EBSP investigations will be mounted in the tube furnace in the beam at the beamline ID11 at the synchrotron radiation facility ESRF in France. The beam will be focused horizontally to 7μm and with a width of 1500μm covering the entire cross section of the sample. The sample will be annealed partially to contain deformed grains as well as new recrystallising grains and nuclei. A gauge volume of 600μm×1000μm×700μm will be fully mapped before and after annealing. Two detectors can be used simultaneously at distances 1.2 and 17cm (Fig. 4). While the near-field detector gives detailed information about the grain shape and position, the far-field detector facilitates orientation indexing based on diffraction spots seen on sharp Debye-Scherrer rings.

The mapping will be done by rotating the sample in the beam over two 45° ranges in the rotation angle ω; [-22.5; 22.5] and [67.5;112.5] in steps of 0.25°. This high angular resolution is crucial for determining the orientations of the recrystallised nuclei. Because the beam will be focused in the z-direction, each rotation gives a map of a thin slice though the sample. The rotation can then be done for many consecutive layers in order to obtain a full 3D map.

The chief improvements of the experimental setup compared to Larsen et al.2005 are therefore:

- The larger volume mapped, which increases the likely number of nuclei likely to be seen. This is important as nuclei are quite rare. The complete cross section of the sample is mapped both before and after the annealing, making comparison more straightforward.

- The increased angular resolution, which makes it possible to determine the orientations of the nuclei with high precision.

- The use of two detectors simultaneously, which will facilitate the creation of a complete map of the sample both before and after the annealing, giving the exact 3D position of the nuclei inside the sample. This allows for distinction between surface and bulk nucleation.

Classically, the critical nucleus size, i.e. the smallest possible nucleus capable of growth, is of the order of 1μm for this type of material (Doherty et al. 1997). The detection limit should thus be smaller than this to be able to determine if the nuclei seen in the experiment have orientations different from what was seen in the deformed structure. A detection limit of about 0.5μm was found to be realistic for the setup described here.

This shows that the 3DXRD method has exactly the requirements needed to study nucleation of recrystallisation. It will be possible to determine which orientations were present at the site before nucleation in 3D, hopefully contributing to the understanding of the nucleation mechanisms, especially for grains of orientations different from those of the parent grains.

4. CONCLUSIONS

The results presented here confirm that triple junctions and grain boundaries are likely sites of nucleation of recrystallisation. A sample was characterised before and after annealing, and several nuclei had emerged. One nucleus had grown by strain induced boundary migration, while the other had an orientation different from any of the parent grains. However, a small

volume (<10μm) with this new orientation may have been present at the nucleation site in the deformed state.

The study was performed using EBSP, which is a surface method and thus not necessarily representative of the bulk. Also, the study was performed with a step size much larger than the critical size of a nucleus capable of growth. A new experiment is proposed using high-energy X-ray diffraction to study a large volume of material before and after annealing in 3D with a sufficiently high resolution.

As nucleation is very important for controlling the recrystallisation texture and microstructure it is considered essential to further the understanding of the underlying nucleation mechanisms for e.g. tailoring thermomechanical processes to obtain specific light and strong metals and alloys with potentials for energy savings.

ACKNOWLEDGEMENTS

The authors gratefully acknowledge the Danish National Research Foundation for supporting the Center for Fundamental Research: Metal Structures in Four Dimensions, within which this work was performed.

REFERENCES

Beck, P.A., and Sperry, P.R. (1950), Strain Induced Grain Boundary Migration in High Purity Aluminum. J. Appl. Phys. 21, 150.

Doherty, R.D., Hughes, D.A., Humphreys, F.J., Jonas, J.J., Juul Jensen, D., Kassner, M.E., King, W.E., McNelley, T.R., McQueen, H.J. and Rollett, A.D. (1997). Current issues in recrystallization: a review. Mater. Sci. Eng. A 238, 219-274.

Duggan, B. (1996). Term suggested at international conference on textures of materials, ICOTOM 11.

Fu, X., Poulsen, H.F., Schmidt, S., Nielsen, S.F., Lauridsen, E. M., and Juul Jensen, D. (2003). Non-destructive mapping of grains in three dimensions. Scripta Mater. 49, 1093-1096.

Humphreys, F.J., Ardakani, M.G. (March 1994). The deformation of particle-containing aluminium single crystals. Acta Metall. Mater. 42, 749-761.

Larsen, A.W., Poulsen, H.F., Margulies, L., Gundlach, C., Xing, Q.F., Huang, X.X. and Jensen, D.J. (2005) Nucleation of recrystallization observed in situ in the bulk of a deformed metal. Scripta Mater. 53, 553-557.

Rodek, L., Poulsen, H.F., Knudsen, E. and Herman, G.T. (2007). A stochastic algorithm for reconstruction of grain maps of moderately deformed specimens based on X-ray diffraction J. Appl. Cryst. 40, 313-321.

Sabin, T.J., Winther, G. and Juul Jensen, D. (2003). Orientation relationships between recrystallization nuclei at triple junctions and deformed structures. Acta Mater. 51, 3999-4011.

Vandermeer, R.A. & Gordon, P. (1959). Edge-Nucleated, Growth Controlled Recrystallization In Aluminum. Trans. Amer. Inst. Mining And Metallurgical Engineers 215, 577-588

Wu, G.L., Juul Jensen, D. (2007). Orientations of recrystallization nuclei developed in columnar-grained Ni at triple junctions and a high-angle grain boundary. Acta Mater. 55, 4955-4964.

A3 Kimdannelse ved rekrystallisation studeret med EBSP og 3DXRD

S. S. West, S. Schmidt og D. Juul Jensen, Dansk Metallurgisk Selskabs Årsmøde, (2009). (Annual meeting of the Danish metallurgical Society)

Risø DTU
National Laboratory
for Sustainable Energy

DTU

Kimdannelse ved rekrystallisation studeret med EBSP og 3DXRD

S. S. West, S. Schmidt og D. Juul Jensen

Metal Structures
in
4D

Abstract

Denne artikel omhandler et studie af rekrystallisation, specielt kimdannelse under varmebehandling af deformeret aluminium. Kimdannelse er vigtig for forståelsen af, hvordan mikrostrukturen af metaller dannes og udvikler sig under rekrystallisation. Forståelsen af mikrostrukturen medfører mulighed for at skræddersy materialer med bestemte makroskopiske egenskaber, f.eks. styrke og smidighed.

Artiklen består af to dele; den første er et overfladestudium udført med Electron Backscattered Diffraction Patterns (EBSP) metoden i et scannings-elektronmikroskop. Her undersøges forholdet mellem den krystallografiske orientering af det deformerede materiale og de nye kim. Den anden del beskriver et eksperiment udført med 3-dimensionel røntgen-diffraktion (3DXRD), hvor et volumen på 600μm×1000μm×700μm er undersøgt ved hjælp af højenergetisk røntgenstråling fra en synkrotron. Orienteringerne af nye kim er fundet og et tredimensionelt kort over deres positioner inden i prøven præsenteres.

1. Introduktion

Når et deformeret metal opvarmes, finder der typisk rekrystallisation sted. Denne proces består i, at de deformerede krystalgitre erstattes af nye perfekte krystaller stort set uden indre fejl og spændinger. Disse krystaller starter som kim, der udvikler sig fra steder i den deformerede struktur, hvor der er særlig høj lokal deformation og deres vækst drives derefter af den energi, der er i den deformerede struktur [1]. Kimdannelses-processen er ekstremt svær at kvantificere og kan sammenlignes med at søge efter en nål i en høstak, og ligeså snart kimet er dannet, melder der sig et nyt problem; kimet fortærer den deformerede struktur og gør det dermed umuligt at bestemme, hvad der var til stede på kimdannelses-stedet i den oprindelige struktur. Dette problem er blevet kaldt spørgsmålet om det forsvundne bevis [2].

Det er generelt accepteret at kimdannelse primært finder sted ved lokale inhomogeniteter i deformationsstrukturen som f.eks. korngrænser, trippel-grænser og partikler af en anden fase [1]. Men alligevel vides det ikke, hvor langs korn- og trippel-grænserne kimene vil komme, eller ved hvilke partikler. Det vides heller ikke hvilken krystallografisk orientering, de nye kim vil have. De mest accepterede teorier siger, at orienteringen af kimene allerede var til stede i den deformerede tilstand (se f.eks. [3]). Mekanismer for formation af sådanne kim med samme orientering som de deformerede korn (kaldet forældre-kornene) kunne f.eks. være Strain-Induced Boundary Migration (SIBM) [4], Subgrain Coarsening eller Subgrain Coalescence (for nærmere beskrivelse af disse tre mekanismer, se [5]). Der findes da også ofte kim med forældre-orienteringer, men herudover er der også rapporteret at nye krystallografiske orienteringer er set [6,7,8].

Målet med arbejdet beskrevet her er at studere kimdannelsen ved at observere de samme prøver før og efter opvarmning med særlig fokus på orienteringerne af de kim, der bliver dannet. For at simplificere undersøgelserne er materialet for eksperimenterne blevet valgt til at være aluminium af høj renhed som er svagt deformeret, så de oprindelige korngrænser stadig er tydelige. I et sådant materiale forventes kimdannelsen primært at foregå langs korn- og trippelgrænser [9].

Den første del af eksperimentet foregår med scannings-elektronmikroskop (SEM), hvor orienteringerne i punkter på overfladen findes ved hjælp af tilbagespredt diffraktion

(EBSP). En række prøver undersøges før og efter opvarmning, hvilket muliggør en direkte undersøgelse af orienterings-forholdet mellem det deformerede materiale og kimet. Denne metode er relativt simpel at anvende, men tillader kun undersøgelser af overfladen af prøven. For at overkomme denne begrænsning har der tidligere været foretaget eksperimentelle undersøgelser med tredimensionel røntgendiffraktion (3DXRD) [6]. Metoden i dette eksperiment viste sig dog at være svær at analysere og arbejdet i denne artikel bygger derfor videre på 3DXRD-systemet med en forbedret metode, der giver mere detaljerede oplysninger.

2. Elektron-mikroskopi

2.1. Eksperimentelt

En række aluminiumsprøver blev skåret ud af 99,996% rent aluminium med en oprindelig gennemsnitlig kornstørrelse på omkring 500µm, som var blevet deformeret 30%. Deformationen var sket ved koldvalsning med petroleum som smøremiddel, og prøverne havde et rektangulært tværsnit på 1×0,6mm hvor to sider var mekanisk poleret mens de to andre var gnistskåret. Herefter var alle fire sider elektropoleret. Denne geometri er nødvendig for at prøverne kan bruges til begge typer eksperiment; 3DXRD-eksperimentet kræver at hele tværsnittet af prøven skal kunne indeholdes i et røntgenbeam på 1200-1500µm, og samtidig kræver EBSP-forsøgene, at den overflade, der skal undersøges, er plan. Det blev besluttet at bruge samme type prøver til begge eksperimenter for at have direkte sammenlignelige data.

I overfladeforsøgene blev en række prøver undersøgt før og efter opvarmning til temperaturer mellem 315 og 325° C i forskellige tidsrum for at finde de ideelle betingelser for kimdannelse. Fordi prøverne havde meget store oprindelige korn, var de generelt meget inhomogene i deres opførsel. Hvor nogle prøver slet ikke dannede kim, havde kimene allerede vokset sig meget store i andre prøver med samme varmebehandling. Varmebehandlingen blev foretaget i en ovn designet til 3DXRD-eksperimenterne bestående af en opvarmet kobberstang, der var i termisk kontakt med prøven. Kobberstang og prøve var så indkapslet i et rør, hvori der var en beskyttet atmosfære bestående af argon for at forhindre at overfladen blev oxideret under opvarmningen. Opvarmningen fra stuetemperatur til den ønskede temperatur tog ca. 10 minutter og efter opvarmning forblev prøven i ovnen og kølede ned her med en kølerate der startede på 25°/minut og herefter faldt af.

Mikrostrukturen blev karakteriseret med EBSP i et JEOL 840 scannings-elektronmikroskop, og maps af overfladen blev konstrueret (se fig. 1).

2.2. Resultater og diskussion

Figur 1 viser EBSP-maps taget på overfladen af en prøve hhv. før og efter opvarmning til 315° C i 15 minutter. Det ses, at rekrystallisationen er begyndt i prøven efter varmebehandlingen, og adskillige nye kim er begyndt at vokse frem. Visse kim er allerede blevet meget store – ideelt set vil vi gerne fange kimene når de stadig er så små, at det er muligt at se, hvor de er opstået. Kimene markeret 1 og 2 er endnu ikke blevet så store, og er derfor udvalgt til yderligere studier. Kim 1 er opstået ved en trippel-grænse, hvor tre af de oprindelige korn mødes. Kim 2 er vokset frem på en korngrænse. Dette er i god overensstemmelse med den generelle antagelse om, at kimdannelsen primært vil finde sted sådanne steder [1,9].

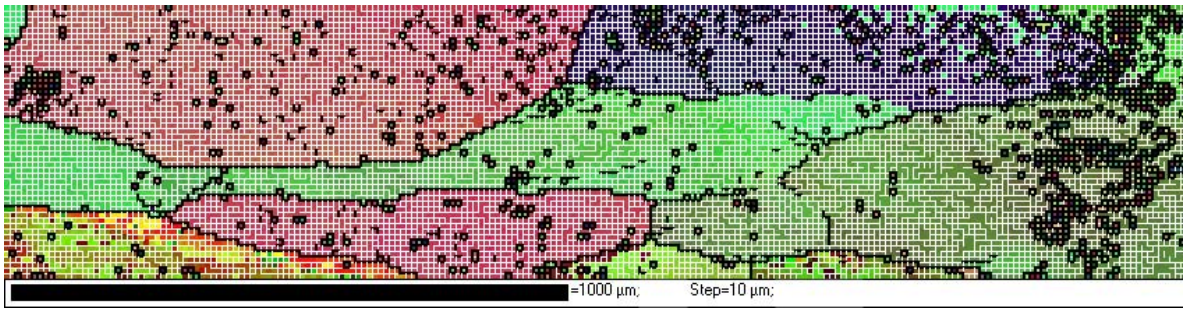

(a)

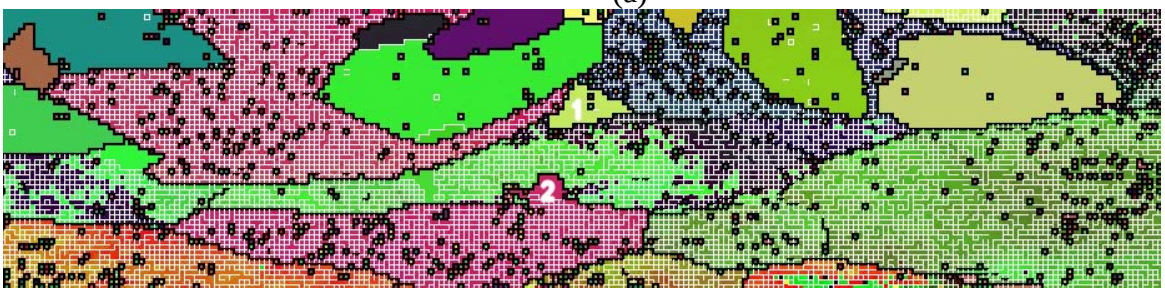

(b)

Figur 1. EBSP-maps af en prøve (a) før opvarmning (b) efter opvarmning. Hvide linjer svarer til minimum 1° misorientering mellem nabo-pixels og sorte linjer svarer til minimum 10° misorientering. Skridtstørrelsen er 10µm. Farvelægningen er baseret på de tre Euler-vinkler (φ_1, Φ, φ_2), således at pixels med samme farver har samme orienteringer.

Selvom det meste af mappet giver et fornuftigt billede af orienteringerne på prøven, er der også visse pixels, der sandsynligvis er fejlindiceret. Orienteringen er fundet ud fra et fit til det Kikuchi-mønster, der opstår ved tilbagespredning fra prøven. Hvor de fleste af de korrekt indicerede pixels er fittet ud fra 7 eller 8 linjer i mønsteret, findes der også pixels, hvor orienteringen er estimeret ud fra helt ned til 2-3 linjer. Dette er ikke nok til at sikre at den korrekte krystallografiske orientering er bestemt. De fejlindicerede pixels ses typisk som pixels af en anden farve end de omgivende og er ofte omgivet af sorte (>10° misorientering) linjer.

Figur 2 viser en forstørrelse af området omkring den trippel-grænse, hvor kim 1 opstod. Et gult punkt lige på grænsen mellem to af kornene markerer en enkelt pixel (10×10µm), som var til stede før opvarmningen og som havde samme orientering som kimet fik efter opvarmning. Hvorvidt der er tale om en reelt indiceret eller en fejlindiceret pixel er uvist, da den med sine 5 Kikuchi-linjer ligger lige på grænsen til det acceptable. En dårlig kvalitet af Kikuchi-mønsteret kan dog skyldes, at det diffrakterende område er meget småt, dvs. mindre end de 10×10µm. Muligheden for, at der har været et lille område tilstede tæt ved trippel-grænsen med den nye orientering som så er vokset til det kim, der ses, kan derfor ikke udelukkes.

Kim 2 har en orientering, der falder indenfor orienteringsspredningen af det ene forældrekorn, og er et typisk eksempel på Strain-Induced Boundary Migration (SIBM), hvor et kim opstår på grænsen mellem to korn med samme orientering som det ene korn, hvorefter forskellen i drivende kraft (stored energy) mellem de to korn driver det til at vokse ind i kornet med den højeste energi.. Figur 3 viser en forstørrelse af mappet omkring kimet.

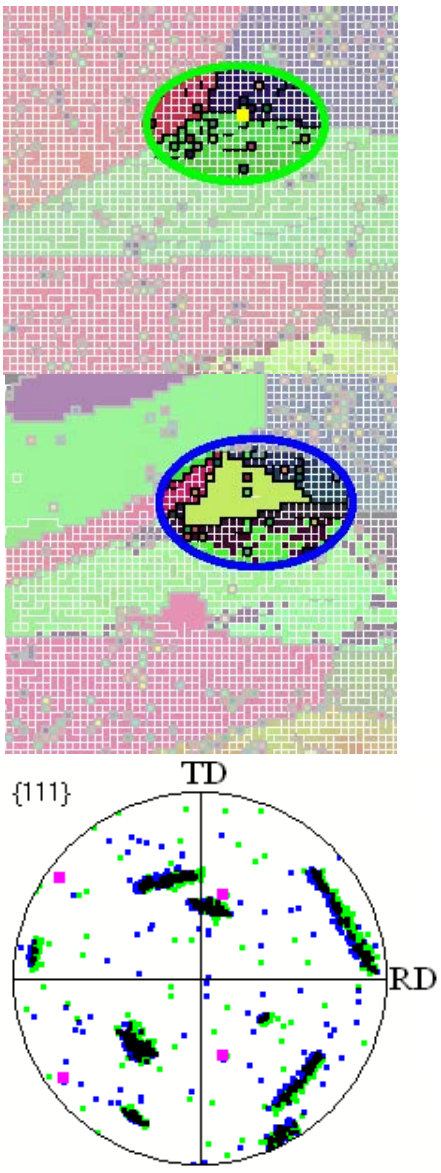

Figur 2. Øverst: EBSP maps af området omkring kim 1. Den gule pixel markerer en pixel med den samme orientering som kimet. Nederst: {111} polfigur af området markeret med ellipser. Grønne punkter er fra mappet før opvarmning, blå fra mappet efter. Ud over en mindre rotation, der skyldes prøveorienteringen i mikroskopet, falder orienteringerne inden for samme område. Kim-orienteringen er markeret med fire større magenta punkter. Den falder præcis oveni orienteringen der svarer til det gule punkt på mappet, og er roteret ca. 40° fra begge de to forældre-korn.

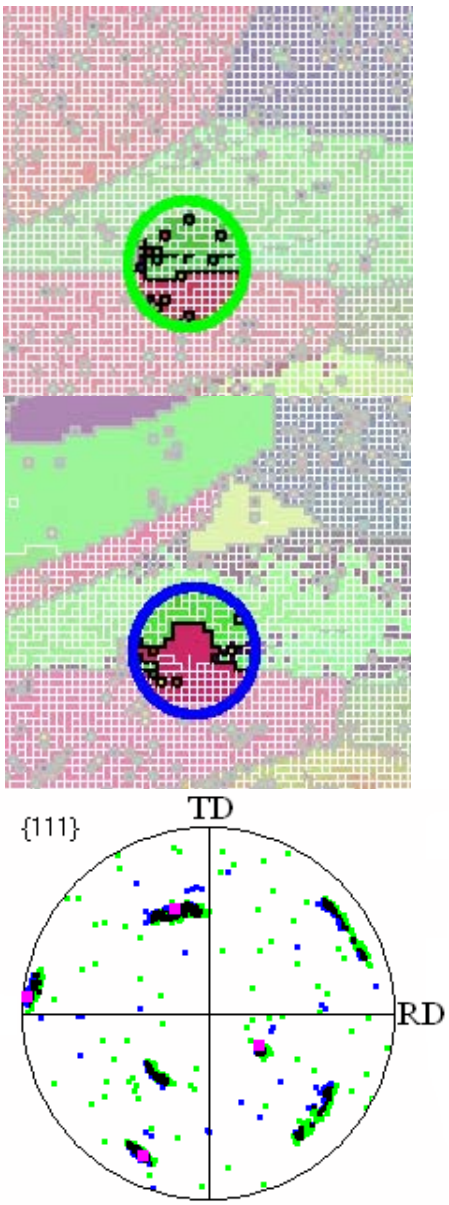

Figur 3. Som figur 2, men for kim 2. Her har kimet en orientering, der falder inden for orienterings-spredningen af et af forældre-kornene. I mappet ses dette ved, at farven af kimet er tæt på farven af det nederste korn, og at der desuden ikke er nogen sort linje imellem de to, svarende til at misorienteringen er mindre end 10°. Herudover ses det også på polfiguren, at de fire kvadrater, der markerer kimets orientering falder indenfor forældrekornets orientering.

De to kim præsenteret her har begge orienteringer, der helt sikkert eller muligvis var til stede i den deformerede tilstand af prøven. Undersøgelser har vist, at kim med nye orienteringer også bliver dannet (f.eks. [8]). Men da EBSP er en overflade-metode, vil den aldrig være i stand til at udelukke, at der har været et lille volumen til stede før opvarmning med samme orientering som et givent kim. Da EBSP kun undersøger de øverste ~10 nm af prøven, kunne et sådant volumen nemt være til stede lige under overfladen uden af blive opdaget. For med sikkerhed at kunne afgøre, om en given orientering er ny, kræves det altså at materialet kan undersøges ikke-destruktivt i tre dimensioner både før og efter opvarmning.

3. Røntgen-forsøg

Tredimensionel røntgendiffraktion (3DXRD) er en metode til at studere det indre af krystallinske prøver ikke-destruktivt. Hvor overfladem etoder som EBSP kun kan karakterisere et snit gennem prøven, er denne metode vigtig fordi den kan se igennem materialet. Hvis samme materiale skal karakteriseres før og efter opvarmning, vil karakterisering af en overflade desuden have det problem, at det ikke kan udelukkes at opførslen på overfladen afviger fra opførslen inde i prøven.

Ved hjælp af diffraktion af højenergetisk røntgenstråling og ved at rotere prøven for at opnå diffraktion fra forskellige vinkler kan en tredimensionel rekonstruktion af materialet laves [10]. Ved hver rotationsvinkel vil de korn, der opfylder Bragg-betingelsen give diffraktionspletter på detektoren. Ud fra diffraktionsmønsteret for forskellige vinkler kan de forskellige orienteringer rekonstrueres. Hvis detektoren er tæt på prøven, vil kornets form og position i prøven desuden påvirke diffraktionsplettens form og placering på detektoren. Derfor er det fordelagtigt at anvende to detektorer for både at få orienteringen meget nøjagtigt (med den fjerneste detektor) og desuden også placering og form (med den nærmeste detektor). Se opstillingen på figur 4.

Simulationer har vist, at tredimensionelle rekonstruktioner også er mulige for svagt deformerede materialer [11]. Da metoden er baseret på at finde orienteringer ud fra diffraktionsspots, er den særlig velegnet til at finde kim med nye orienteringer. Et kim med forældre-orientering vil have diffraktionsspots oveni eller tæt på spots fra det deformerede forældre-korn, hvilket gør det svært eller umuligt at detektere kimet. Et kim med ny orientering vil imidlertid dukke om som diffraktionsspots på helt nye steder.

Et tidligere 3DXRD-eksperiment fandt kun 3 kim, da kimene kun er ganske få og små og derfor kræver undersøgelse af et meget stort volumen [6]. Et nyt og forbedret setup blev derfor brugt til dette forsøg.

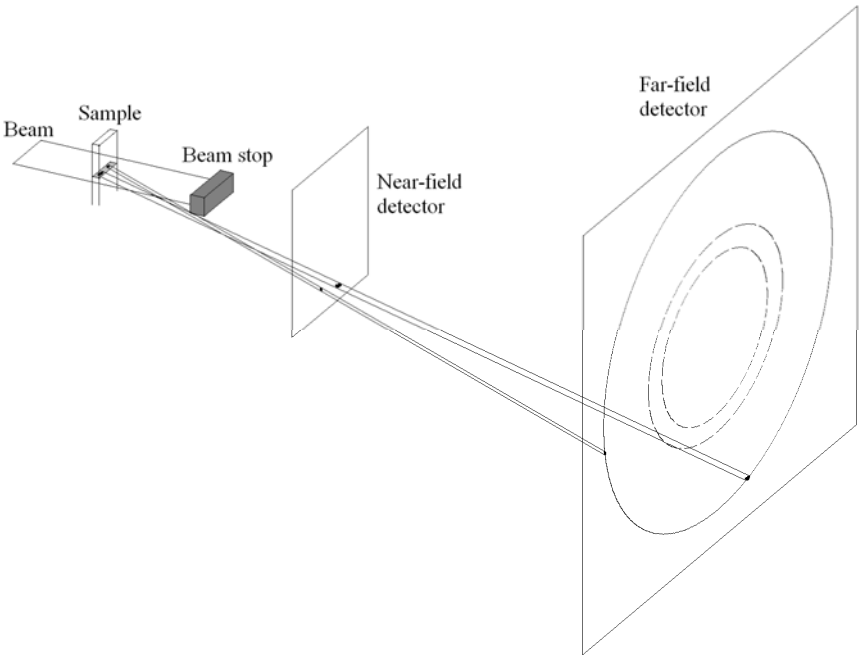

Figur 4. Opstilling med to detektorer. På den fjerneste detektor vil diffraktionspletterne samle sig på smalle Debye-Scherrer-ringe, mens på den nærmeste detektor vil positionen og formen af diffraktionspletterne afspejle de diffrakterende korns form og position i prøven.

3.1. 3DXRD-opstilling

En prøve af samme type som til EBSP-forsøget blev brugt til røntgen-eksperimentet. Ovnen blev opstillet i røntgenstrålen på beamlinjen ID11 på synkrotronfaciliteten ESRF i Frankrig. Røngenstrålen blev fokuseret lodret til en højde på 7μm, hvor bredden af strålen var 1500μm, hvilket betød at hele prøvens tværsnit var inde i strålen ved alle rotationsvinkler. Ca. 100 lag af højde 7μm blev studeret ved 360 forskellige rotationsvinkler med 0.25° imellem for at kortlægge de krystallografiske orienteringer i de enkelte lag. De samme lag blev undersøgt før og efter at prøven var blevet opvarmet i kort tid til 320° C, hvor rekrystallisationen var begyndt. Det betyder, at et volumen på 600μm×1000μm×700μm blev kortlagt. Til kortlægningen blev to detektorer anvendt samtidig med afstande 1,2 og 17cm (Fig. 4).

De vigtigste forbedringer på opstillingen i forhold til [6] er:

- Et større volumen er mappet, hvilket øger chancen for at finde kim. Hele tværsnittet af prøven er desuden mappet både før og efter, hvilket gør sammenligning af data mere ligetil.

- Vinkelopløsningen er øget, hvilket gør bestemmelsen af kimenes orientering meget nøjagtig.

- To detektorer anvendes samtidig, hvilket betyder, at den nøjagtige 3D-position af kimene i prøven kan findes. Dette betyder, at det er muligt at skelne mellem kim, der er dannet på overfladen og kim, der er inden i prøven.

3.2 Tre-dimensionelle resultater

Omkring 60 kim blev identificeret i dataene efter opvarmning. Af disse viste størstedelen sig dog at stamme fra overfladen af prøven, især de to flader, der var gnistskåret. Ved nærmere eftersyn var mange af disse overfladekim allerede til stede inden opvarmningen og er derefter vokset da prøven blev varmet op. Dette er en vigtig opdagelse, da gnistskæring ofte betragtes som en nænsom metode, der efterlader overfladen upåvirket. Men ud fra dette forsøg ses, at gnistskæringen faktisk giver kimdannelse allerede under processen.

Af de fundne kim var der dog 6, som ikke rører nogle af overfladerne, og dermed med sikkerhed kan siges ikke at stamme derfra.. Figur 5 viser et kort over disse 6 kims placering. I hvert enkelt lag er massecentrum og volumen fundet ud fra diffraktionspletternes placering og intensitet på diffraktionsbillederne på den fjerneste detektor. En skive med det givne volumen er derefter tegnet ind på figuren.

Nogle af kimene er allerede vokset til en størrelse ~100μm, mens de mindste er ~10μm. I princippet er det med forsøgsopstillingen muligt at opdage kim helt ned til 2-3μm i diameter. Eksponeringstiden på 1 sekund var sat efter at fange så små pletter som muligt netop for også at kunne studere helt små kim, men samtidig undgå at de store diffraktionspletter fra de store deformerede korn gik i mætning på detektoren.. På grund af kimenes meget lille interne misorientering (kimene er stort set perfekte krystaller), fordeler diffraktionen fra kimet sig og et meget lille område og kun et enkelt eller to på hinanden følgende billeder. Dette gør, at selvom kimene er mindre end de deformerede korn, er der stadig en risiko for, at deres diffrationspletter går i mætning. Dette giver en vis usikkerhed på bestemmelsen af massecentrum og volumen.

Flere af kimene ligger forholdsvis tæt på hinanden, hvilket tyder på, at de kan stamme fra samme korn- eller trippelgrænse. Dette er interessant, fordi det antyder, at det er bestemte korngrænser, der er de foretrukte kimdannelses-steder for kim med nye orienteringer.

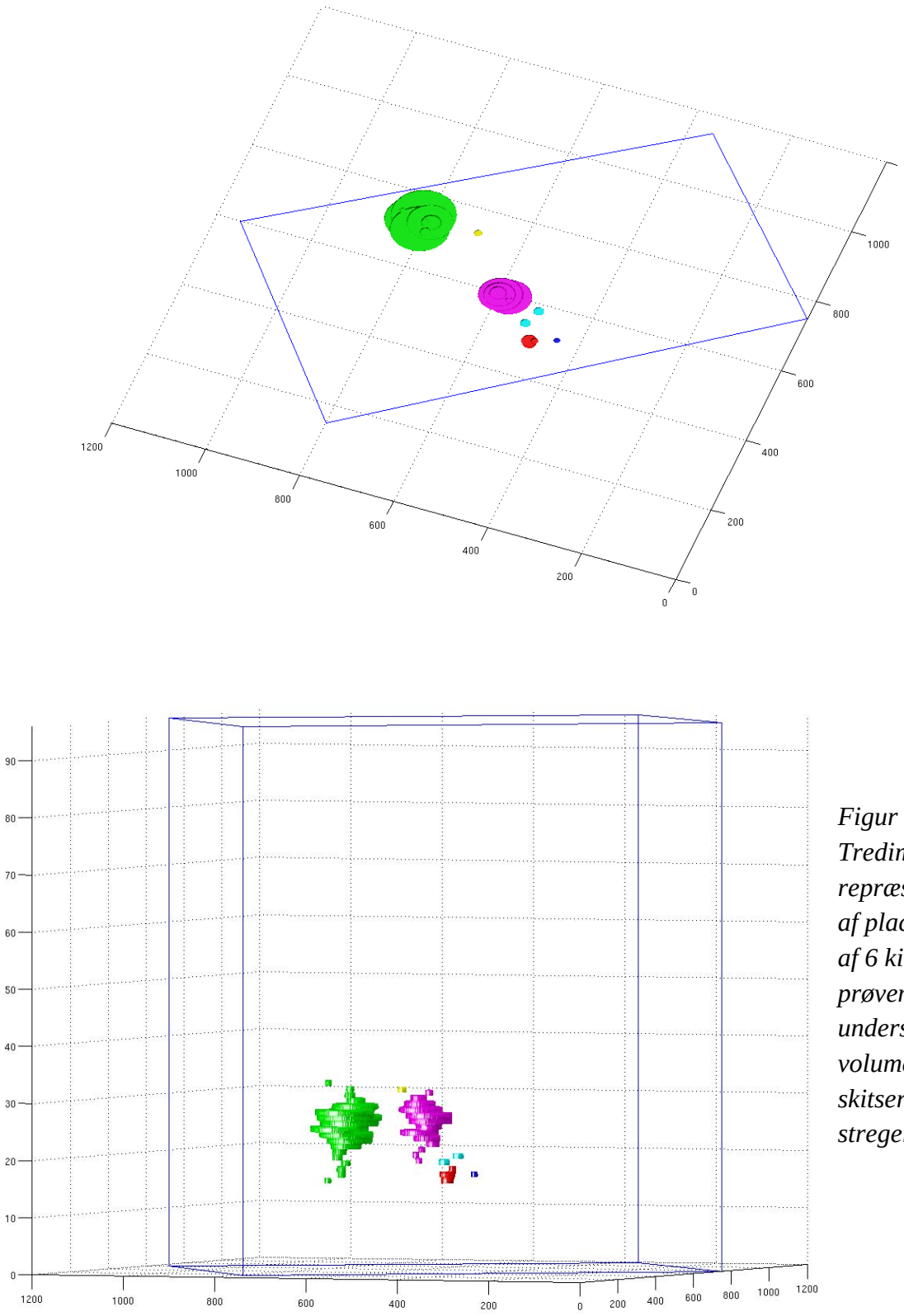

Figur 5. Tredimensionel repræsentation af placeringen af 6 kim i prøven. Det undersøgte volumen er skitseret med streger.

4. Yderligere opgaver

Ud fra dataene taget med den nærmeste detektor kan også den deformerede del af prøven samt kimenes form kortlægges. Sammenligning af kimenes orientering med orienteringen af de forældrekorn, der er nærmest vil give mulighed for sammenligning med resultaterne fra EBSP. Orienteringsforholdet mellem kim og forældre er vigtigt for forståelsen af mekanismerne bag dannelsen af kim med nye orienteringer og dermed en samlet forståelse af rekrystallisationen og de endelige orienteringer.

5. Konklusioner

Resultaterne der blev præsenteret her, bekræfter korn- og trippelgrænser som foretrukne kimdannelses-steder. En prøve blev karakteriseret med EBSP før og efter opvarmning til begyndelsen af rekrystallisationen, og adskillige kim var dannet. Af de to, der blev undersøgt nøjere, var et af dem vokset frem ved SIBM, og havde derfor samme krystallografiske orientering som et forældrekorn, hvor det andet havde en orientering, der var forskelligt fra de tre mulige forældrekorn. Der var dog muligvis et lille volumen (<10µm) til stede med orienteringen allerede i den deformerede tilstand. Tilstedeværelsen af et lille volumen med orienteringen af et givent kim inden opvarmningen vil aldrig fuldt ud kunne udelukkes med en overfladem etode som EBSP.

Derfor blev et nyt eksperiment udført med 3DXRD, hvor en prøve kunne karakteriseres før og efter opvarmning i tre dimensioner for at undersøge, om der kunne dukke kim op med helt nye orienteringer. Seks kim med sådanne nye krystallografiske orienteringer forskellige fra den deformerede tilstand blev fundet og deres positioner og volumener vist på et 3D-plot. Det ses, at flere af kimene dannes i samme område af prøven, hvilket tyder på, at det er særligt fordelagtigt for kim med nye orienteringer at vokse frem ved bestemte korn- eller trippelgrænser.

Sammenligningen af de nye kim med forældrekornenes orientering er et utrolig vigtigt redskab til opbygningen af nye og bedre modeller for kimdannelse. Hvor tidligere modeller har været nødsaget til at lave antagelser omkring kimenes orientering vil denne type lokale målinger være med til at øge forståelsen for, hvilke orienteringer, kimene dannes med, og hvor i prøven de dannes. Kimenes orientering og placering er med til at bestemme den endelige mikrostruktur af materialet, da de ved yderligere varmebehandling vil vokse og udfylde hele prøven med deres orientering, og dermed bestemmer de materialets endelige makroskopiske egenskaber.

Tak

Forfatterne vil gerne takke Grundforskningsfonden for støtten til grundforskningscenteret: Metalstrukturer i fire dimensioner, hvorunder dette arbejde er udført.

Referencer

1. Doherty, R.D., Hughes, D.A., Humphreys, F.J., Jonas, J.J., Juul Jensen, D., Kassner, M.E., King, W.E., McNelley, T.R., McQueen, H.J. and Rollett, A.D. (1997). Current

issues in recrystallization: a review. Mater. Sci. Eng. A 238, 219-274.
2. Duggan, B. (1996). Term suggested at international conference on textures of materials, ICOTOM 11.
3. Humphreys, F.J., Ardakani, M.G. (March 1994). The deformation of particle-containing aluminium single crystals. Acta Metall. Mater. 42, 749-761.
4. Beck, P.A., and Sperry, P.R. (1950), Strain Induced Grain Boundary Migration in High Purity Aluminum. J. Appl. Phys. 21, 150.
5. Humphreys, F.J. and M. Hatherley, Recrystallization and related annealing phenomena. Pergamon, 1. edition ed., 1995.
6. Larsen, A.W., Poulsen, H.F., Margulies, L., Gundlach, C., Xing, Q.F., Huang, X.X. and Jensen, D.J. (2005) Nucleation of recrystallization observed in situ in the bulk of a deformed metal. Scripta Mater. 53, 553-557.
7. Sabin, T.J., Winther, G. and Juul Jensen, D. (2003). Orientation relationships between recrystallization nuclei at triple junctions and deformed structures. Acta Mater. 51, 3999-4011.
8. Wu, G.L., Juul Jensen, D. (2007). Orientations of recrystallization nuclei developed in columnar-grained Ni at triple junctions and a high-angle grain boundary. Acta Mater. 55, 4955-4964.
9. Vandermeer, R.A. & Gordon, P. (1959). Edge-Nucleated, Growth Controlled Recrystallization In Aluminum. Trans. Amer. Inst. Mining And Metallurgical Engineers 215, 577-588
10. Fu, X., Poulsen, H.F., Schmidt, S., Nielsen, S.F., Lauridsen, E. M., and Juul Jensen, D. (2003). Non-destructive mapping of grains in three dimensions. Scripta Mater. 49, 1093-1096.
11. Rodek, L., Poulsen, H.F., Knudsen, E. and Herman, G.T. (2007). A stochastic algorithm for reconstruction of grain maps of moderately deformed specimens based on X-ray diffraction. J. Appl. Cryst. 40, 313-321.

A4 Analysis of orientation relations between deformed grains and recrystallization nuclei

S.S. West, G. Winther and D. Juul Jensen, Submitted to: Metallurgical and Materials Transactions A (Physical Metallurgy and Materials Science), (2009).

Analysis of orientation relations between deformed grains and recrystallization nuclei

S. S. West, G. Winther and D. Juul Jensen
Center for Fundamental Research: Metal Structures in Four Dimensions, Materials Research Division, Risø National Laboratory for Sustainable Energy, Technical University of Denmark, PO box 49, DK-4000 Roskilde, Denmark

Abstract

Nucleation in 30% rolled high purity aluminum samples was investigated by the electron backscattering pattern method before and after annealing. A total of 29 nuclei including 2 twins were observed and about 1/3 of these had orientations not detected in the deformed state. Possible orientation relations between these nuclei and the deformed state were by 20-55° rotation around <111>, <112>, <100> or <110> axes. These axes were compared to the active slip systems and the crystallographic features of the deformation induced dislocation boundaries. Good agreement was found between the <111> rotation axes and the normal to slip planes with which dislocation boundaries align. The exact nucleation mechanism has not been established, but the observed orientation relations allow prediction of which grains are likely to form <111> rotated nuclei, although these may not all do so.

I. Introduction

When a deformed metal is annealed, recrystallization typically takes place. During this process, nuclei which are small and almost strain-free perfect crystals develop locally in the deformed structure and grow to become grains, driven by the stored energy in the deformed material. When all the deformed material has been consumed by strain-free grains, recrystallization is complete.

Typical sites for nucleation of recrystallization are; i) grain boundaries, ii) triple junctions and corners, iii) second phase particles and iv) shear and transition bands [1, 2], as all these sites are prone to locally build up a higher stored energy during deformation. Although these sites are well accepted as likely nucleation sites, it is still not known which of them will give nucleation or where upon them it will occur. Understanding the mechanisms of nucleation is vitally important for making realistic models of recrystallization.

As there are generally relatively few nuclei, the study of nucleation has been compared with the search for a “needle in a haystack”. The search is further complicated by the fact that usually, the whole three-dimensional structure cannot be observed, but only the surface plane of polish can be studied. Thus when a nucleation event takes place in the bulk of the material, the nucleus consumes the deformed material, making it impossible to quantify what was there before at the nucleation site. This has been referred to as the problem of “lost evidence” [3].

The crystallographic orientation of the nuclei cannot be fully predicted either. Accepted nucleation theories propose that the orientations of the nuclei must already be present in the deformed state before annealing. The nuclei could form by mechanisms such as strain-induced boundary migration (SIBM) [4], subgrain coarsening [5] or subgrain coalescence [6]. SIBM takes place at high angle grain boundaries, where the bulging of the boundary creates a small strain-free region capable of

growing into the neighboring grain. Subgrain coarsening and coalescence involve the merging of multiple subgrains of similar orientations either by rotation (subgrain coalescence) or by the migration of the low angle grain boundary (subgrain coarsening).

Indeed, nucleation of grains with orientations within the spread of the deformed matrix is commonly seen (see e.g. [7]). However, several studies have shown that nuclei of new orientations also appear [8, 9, 10, 11, 12, 13]. Some modeling work has shown that small volumes may rotate during annealing to create new orientations [14], although this mechanism only seems to be applicable to nanoscale structures. Inoko suggested that nuclei are rotated around a <111> axis corresponding to the cross slip plane normal common to two or more active systems. It has further been proposed that very small portions of the lattice may rotate about <112> axes in active slip planes [15]. In the work by Driver et al. [12] on single crystals, they found that the observed rotations were always around a <111> axis normal to active slip planes. Sabin et al. [9] also found good agreement with <111> axes normal to highly active slip planes and further found a correlation with the occurrence of deformation induced dislocation boundaries aligned with such slip planes. Recently, Paul and Driver [11] observed nuclei in bicrystals related to the deformed crystals by rotation around several low index axes, including but not limited to <111>.

The aim of the present study is to investigate nucleation with a focus on orientation relationships between the individual nuclei, slip systems and crystallographic planes of the deformation induced dislocation boundaries. The first part of the paper presents the quantitative analysis of the experimental data to identify possible orientation relations. In the second part of the paper these orientation relations expressed in terms of rotation axes and angles are investigated in relation to slip systems and dislocation boundaries. In this analysis it is assumed that the slip systems can be predicted by either the Taylor model or from the Schmid factors. To connect to the dislocation boundaries we rely on newly established relations which allow prediction of the crystallographic alignment of dislocation boundaries based on the slip systems [16, 17].

Weakly-deformed pure aluminum polycrystals was chosen for this study to be able to compare the results to those of Sabin et al [9]. By contrast to this previous study, great care has been taken to prepare a well-annealed starting structure. The aim was to achieve grain boundaries which have minimized their energy by forming triple junctions close to 120° [18]. The experimental investigation was done by electron backscattering pattern (EBSP) analysis of a series of samples both in the deformed state and after annealing. Exactly the same sample areas were characterized before and after annealing allowing a direct investigation of orientation relationships between the structures seen before nucleation and the nuclei.

II. Materials and experimental methods

The starting material for this investigation was 99.996 % pure aluminum with grain sizes of 100-1000 µm with an average grain size of approximately 500 µm. The grain boundaries were almost straight and 74% of the triple junction angles were between 90° and 150°. This material was deformed 30 % by cold rolling in six rolling steps with *l/h* approximately 1.7, which is chosen to obtain a high homogeneity of deformation through the thickness of the sample [19]. Petroleum was used for lubrication to minimize the friction during the deformation.

From the deformed material several samples were cut and the ND-TD-surface was first mechanically polished and then electropolished. Two different microscopes were used for characterization; a JEOL JSM 840 SEM and a Zeiss Supra 35 FEGSEM. The samples were examined by EBSP with step sizes of 2-10 μm before and after annealing. This step size is rather coarse, and the risk of overlooking small features is present. Nevertheless, in order to cover a large area, it was deemed that a large step size was necessary. Also, we wished to cover the entire area of the sample and not just triple junction areas to be able to make a complete description of nucleation sites both at triple junctions and away from them. Previous studies have been done with a smaller step size [9], and as will be shown, the results obtained here for triple junction nucleation are not qualitatively different from what was seen using a finer resolution.

The annealing was carried out in a furnace where the sample was in thermal contact with a copper rod at a known temperature while inside a tube with a protective argon atmosphere to prevent oxidation of the surface. This allowed the exact same areas of the samples to be examined before and after annealing. The annealing times were between 10 and 15 minutes and the temperature between 315°C and 320°C.

The EBSP maps were created by scanning over the surface of the samples to obtain the orientation at each point. The orientation was found from a fit to the Kikuchi lines of the diffraction pattern. The best fitted orientations were assigned in each point, where the points (pixels) had sizes of 2×2 μm to 10×10 μm. Due to imperfections of the surface preparation or the depth of focus of the microscope, some pixels may be wrongly indexed. These will usually be characterized by a low number of correctly fitted Kikuchi lines. Thus points with less than five matching Kikuchi lines were disregarded in the analysis if their orientation was not within 10° of any of the 4 neighboring points, i.e. they were surrounded by high-angle boundaries. These points are shown as white pixels in figures 1 and 2.

III. Nucleus/parent relations

A. Orientation relationships

In 7 samples, a total of 29 nuclei were found and analyzed quantitatively with respect to the orientations present in the deformed matrix before annealing. The samples were named A-G. In the tables, A01, for example, represents the first nucleus in sample A.

Orientation relationships in the form of a rotation around a low index axis (<100>, <110>, <111> or <112>) were investigated by comparing the orientation of the nucleus to all orientations in the EBSP map before annealing in an area covering the nucleus as observed after annealing plus all points within a rim of about 20 μm outside the boundaries of the nucleus. For each point in this area the crystallographic misorientation to the nucleus was calculated. Nuclei which lie within 10° of a point in the deformed map were considered to be of an orientation already present in the deformed state, i.e. not a new orientation. For the remaining nuclei, the misorientation axis for each point in the deformed map was compared to the ideal low index axes <111>, <112>, <100> and <110>. If the calculated misorientation axis was within an arbitrarily selected 10° of one of these low index axes, this low index axis was taken as a possible rotation axis involved in the nucleation. In many cases several possible axes were identified.

Based on the above analysis the nuclei fall into three types:

I. Nuclei whose orientations have a misorientation of less than 10° to a point in one of the parent grains. The misorientation is defined as the smallest possible rotation about any axis than will bring the lattices to coincide. This group consists of 14 nuclei. These nuclei are considered to have the same orientation as the parent grain. (A further 5 nuclei were found with orientations that were present in the deformed state but only in one or a few pixels. These nuclei have been left out of Table I and for the rest of the analysis.)

II. Nuclei with orientations not present in the deformed state, i.e. with a misorientation of more than 10° to the closest orientation observed in the deformed state. The 8 nuclei that fall into this group have an average minimum misorientation to the deformed state of 29°. These show a variety of relations to the pre-annealing orientations, as listed in Table I. Some of the nuclei are adjacent and have an internal 60°/<111> relationship. These are likely to be examples of recrystallization twinning. As it is impossible to tell which nucleus came first and which is the result of subsequent twinning, all 8 nuclei are included in the analysis of orientation relations between nuclei and the deformed state in Table I. Table I shows that all four low index axes included in the analysis are found to be possible for at least one nucleus in the data set. The corresponding misorientation angles range from 20° to 55° with an average of 29°.

III. Nuclei with a first order twin relationship to one of the parent grains. As the mechanism of twinning is well known, we will not study these 2 nuclei any further.

B. Nucleation sites

Of the 22 nuclei of Type I and II, 14 appeared at triple junctions, 5 at grain boundaries and 3 in grain interiors. However all of the 3 nuclei in grain interiors had a boundary with another nucleus that touched a grain boundary or a triple junction. Due to the three-dimensional nature of the grain boundaries, there could easily be original grain boundaries or triple junctions running close to the surface at a shallow angle from which the nuclei may have originated. Approximately 20 % of all triple junctions gave nucleation within the annealing time.

Figures 1 and 2 show typical examples of EBSP maps of triple junctions before and after annealing, where nucleation has taken place. Figure 1 is an example of SIBM, where a nucleus has grown from a grain boundary close to the triple junction. The nucleus has an orientation within the mosaic spread of one of the deformed grains and has grown into the other grain at the boundary. It thus falls into Type I above. The nucleus is not a perfect crystal, but retains some internal misorientations, as can be seen by the low-angle boundaries within the nucleus. Figure 2 shows a triple junction where multiple nuclei have appeared. Nuclei D06 and D07 are Type II, while nucleus D05 is Type I. One of the nuclei (D07) consists of only two pixels and thus has an area intersecting the sample surface of 20 μm^2. Most other nuclei seen in the samples have grown quite large within the annealing time, and some have grown so large that it is not reasonable to discuss the point of nucleation. The nucleus D07 has a twin relation to the neighboring nucleus D06. This means that these two nuclei have a common <111> pole as seen in figure 3. D06 also has a different <111> pole in common with one of the deformed parent grains, namely grain 1.

IV. Relation to slip systems and dislocation boundaries

Although the mechanism behind formation of nuclei of new orientations is not known it seems likely that reordering of the deformation induced dislocation structure plays a role. Previous studies have found that nuclei rotated around a <111> axis develop in grains with high slip activity on the slip plane to which the <111> axis is normal [12] and this has been correlated with the occurrence of dislocation boundaries aligned with this active {111} plane [9]. This does, however, not explain

the reports about other rotation axes, such as <211> and <100> [11]. In order to investigate the orientation relations in more detail, the possible rotation axes between parent and nucleus determined in Table I are compared to the dislocation boundaries in the following.

The dislocation structure in weakly rolled aluminum typically consists of extended planar boundaries (also referred to as geometrically necessary boundaries or GNBs) as illustrated in figure 4. In between these almost straight boundaries, short randomly oriented cell boundaries and some loose dislocations are found. The crystallographic plane of the extended planar boundaries has been demonstrated to depend on the grain orientation [16]. This grain orientation dependence has been traced to an underlying dependence on the slip systems and predictive relations between slip systems and dislocation boundary planes have been established [17]. As the experimental EBSP maps do not have sufficient resolution to reveal dislocation boundaries, these relations will be employed to predict the crystallographic planes of the dislocation boundaries based on slip system predictions using both the Taylor model and Schmid factors.

While many slip system combinations are possible, leading to a wide range of dislocation boundary planes (see [17] for more details), two situations are most relevant to the current case of weakly rolled aluminum:

1. If a single system dominates in a grain, the GNB aligns closely with the active {111} slip plane but the exact GNB plane deviates a few degrees from the exact {111} by rotation around the <112> axis perpendicular to the active slip direction. If two systems are equally active in the slip plane the deviation is by rotation around the <110> axis, which is the sum of the two <112> axes perpendicular to the active slip directions. In the following, this <112> or <110> axis is referred to as the deviation axis.
2. GNBs align with {110} or {100} planes when two systems with the same slip direction are equally activated. The signs of the slip systems determine whether the GNBs align with {110} or {100}. If the two systems are not equally activated the boundaries lie closer to the more active slip plane, and boundaries on for example {112} planes can be formed.

In rolled aluminum two sets of GNBs aligned with different planes sometimes coexist [16].

For the parent grain orientations in Table I, the dominant slip systems and thus the expected crystallographic orientations of the dislocation boundaries was first predicted. In most cases the Taylor model and Schmid factor analysis resulted in the same slip systems, adding confidence to the identified slip systems. Using the relations between slip systems and crystallographic GNB planes, it was determined whether the slip systems could give rise to a GNB plane normal or a deviation axis (see (1) above) agreeing with the observed rotation between the nucleus and deformed state. For clarity only the rotation axes where agreement was found between the predicted GNB plane normal or deviation axis and the observed axis are included in Table II. Where no agreement was found, a "-" is noted in the table. The table shows that the observed variants of the <111> rotation axes between nuclei and deformed state are in perfect agreement with the crystallographic alignment of the GNBs in all cases except two which are discussed below. In one case there is an additional agreement with the <112> deviation axis.

The two cases for which no agreement was found involve two observations of adjacent twin-related nuclei. In both cases, one of these nuclei is predicted to have a {111} aligned GNB while the other one is not (see Table II). An example of this is seen in figure 2, where nuclei D06 and D07 are twin

related. Although it is impossible to verify, this suggests the initial formation of a <111> rotated nucleus and a subsequent twinning to generate the second nucleus.

V. Discussion

Nucleation of recrystallization is a rare event, and large volumes need to be examined in order to find the nuclei. The experiments on which this study is based allow for direct comparison of the microstructure before and after nucleation by examining the same areas of the samples before and after annealing.

A. Nucleation sites

As was expected from previous work [9, 20], nucleation occurred primarily at triple junctions. A substantial fraction (38 %) were, however, found outside triple junction regions, i.e. near grain boundaries or in grain interiors. As only the surface was investigated here it can of course not be ruled out that these nuclei originate from a triple junction below the surface.

About 20% of all the triple junctions had nuclei present after the annealing. For comparison, Vandermeer and Gordon [20] found nucleation at only 6% of triple junctions and Sabin et al. [9] found nucleation at more than half of their triple junctions. The three studies including this one all used aluminum rolled to 30-40% reduction, but differed in triple junction geometry. This difference follows the observed nucleation frequency with the lowest frequency in the material of Vandermeer and Gordon, which has the most well-annealed triple junctions, and the highest frequency in the material of Sabin et al., which had the most irregular triple junctions. This suggests a strong influence of the triple junction geometry.

B. Nucleation types

In agreement with other studies [9, 10, 11], the nuclei could be divided into two main types not counting twins. The first group, type I, had orientations within the spread of the parent grain orientation caused by the deformation, which in the present case of coarse EBSP maps was interpreted as orientations within 10° of the orientations measured by EBSP. Liu et al. [21] found that a 30% deformed aluminum polycrystal had an average misorientation across GNBs of about 5° and an average misorientation of about 1° across cell boundaries, so the criterion of 10° was chosen to allow for realistic local misorientations in the deformed state. The parent oriented nuclei are typically examples of SIBM. Almost two thirds of the nuclei were of this type. This fraction is somewhat larger than that seen in [9], where the samples had been deformed to a larger reduction (40%). This is in good agreement with [4], which states that SIBM is a more important nucleation mechanism for smaller strains. Also in agreement with [9], these nuclei have the largest internal orientation spread, as seen in figures 1 & 2.

The second group of nuclei, type II, covers those that have quite high misorientation angles to all points within the parent grains. The critical embryo size, i.e. the smallest possible volume needed to initiate growth, is generally considered to be of the order of 1 μm^3 [1]. The step size in the present study is 2-10 μm. However, previous studies with a smaller step size of 1 μm [9] have shown similar results. Even with a very small step size (<<1 μm), a volume with the nucleus orientation could have been present below the surface, as the EBSP method only probes the top ~10 nm of the sample [22]. So with this method it is never possible to conclusively say that the new orientations were not already present in the deformed state, but as discussed in detail in [9], the deformation structures in this type of samples are not likely to give rise to local variations in orientation of such

magnitude as observed between the nuclei of new orientations and the parent grains (29° on average).

The analysis of the orientation relations between nucleus and parent found that at least one, and in 7 out of 8 cases more than one, low index rotation axes were possible between the nuclei and parent grains, including those that have been reported before for bicrystals [11]. Following the lines of a previous study [9], the rotation axes were correlated with crystallographic alignment of the deformation induced dislocation boundaries. The previous study only focused on the occurrence of {111} aligned boundaries but here we also considered other possibilities based on recent progress in the characterization and understanding of such boundaries [16, 17]. The present result shows that the <111> axes coincided with the crystallographic alignment of the boundaries when also considering the symmetric variant of the axes. This of course does not rule out the existence of other rotation axes in other samples, for example with grains of other orientations.

It should be mentioned that we also analyzed for the correlation with a <111> axis normal to a slip plane which is the cross slip plane common to two or more active systems, as found in other studies [8]. However, no such correlation was found.

A similar analysis of slip systems and GNB planes was carried out for the cases where the nuclei had orientations already present in the deformed matrix. Only half of the parent orientations were found to have slip systems leading to GNBs aligned with {111}. Analysis of the grains connected in triple junctions where nucleation was not observed (two cases) also showed that only half of the grains were expected to have GNBs aligned with {111}. Although circumstantial, these findings indicate that {111} aligned GNBs promote nucleation by <111> rotations but their mere presence is not sufficient to induce nucleation. It further indicates that {111} aligned GNBs are not so frequent that one can always find such a feature to fit the observed nucleus/deformed parent relations, in particular when also considering the variant of the {111}.

C. Dislocation boundaries and nucleation

The correspondence between the predicted slip systems, dislocation boundary planes and the observed nuclei orientations may appear surprising as the deformation mode and therefore also the slip systems near triple junctions are expected to be influenced by the presence of the triple junction. Such effects are indeed often observed in the form of a higher stored energy and somewhat different morphology of the dislocation structure near triple junctions compared to the findings in the grain interior [23, 24]. Due to the regularity of the well-annealed triple junctions, such morphological disturbances may be less significant although the energy stored close to junctions may still be higher than elsewhere. Although far from conclusive, the present data may also indicate that <111> rotated nuclei do not necessarily form in the immediate vicinity of the triple junction but some distance away.

While the <111> rotated nuclei appear to be strongly related to <111> features of the deformed state, the exact nature of these features cannot be pinpointed. The identified <111> axes correspond to the plane with which the GNBs align. However, these GNBs often have twist character [21], meaning that the variant of the <111> GNB plane normal coincides with the axis of the crystallographic misorientation across the GNB. As these GNBs further occur when one or two slip systems in the {111} plane are highly active, it is further possible that it is not the GNB itself but

rather the high concentration of dislocations – whether incorporated in the GNBs or not – with Burgers vectors lying in the {111} plane that are important.

IV. Conclusions

Nucleation in 30% rolled pure aluminum polycrystals was investigated by EBSP before and after annealing.

1. About two thirds of the nuclei had an orientation within the orientation spread of the parent grains while about one third had new orientations not observed in the deformed state.
2. The orientation relationship in the form of a rotation axis and angle between nucleus with new orientation and deformed parent grains was analyzed, finding 30-50° rotation around <111> as a possibility for all nuclei. Also <112>, <100> and <110> were potential rotation axes for some of the nuclei.
3. Analysis of the possible orientation relations in terms of the expected slip systems and further with the expected characteristics of the deformation induced dislocation boundaries revealed good agreement between the specific variant of the <111> rotation axes and the normal to highly active slip planes, with which dislocation boundaries align. The other possible rotation axes could not be attributed to crystallographic features in the deformation induced dislocation structure.
4. It is suggested than grains with {111} slip plane aligned GNBs are likely to produce nuclei with new orientations which are rotated about the variant of the <111> axis normal to this slip plane.

Acknowledgements

The authors gratefully acknowledge the Danish National Research Foundation for supporting the Center for Fundamental Research: Metal Structures in Four Dimensions, within which this work was performed.

References

[1] F. J. Humphreys and M. Hatherley: *Recrystallization and related annealing phenomena*, 1st ed., Elsevier Ltd., Oxford, U.K., 1995.

[2] H Paul: *Mater. Chem. Phys.*, 2003, vol 81.(2-3), pp. 531–534,.

[3] B. Duggan: Hong Kong, Term suggested at international conference on textures of materials, Icotom 11, 1996.

[4] P.A. Beck and P.R. Sperry: *J. Appl. Phys.*, 1950, vol. 21(2), pp.150–152.

[5] J. C. M. Li: *J. Appl. Phys.*, 1962, vol. 33(10), pp. 2958.

[6] J. W. Cahn: *Proc. Phys. Soc. A*, 1950, vol. 63, pp.323–336.

[7] R. D. Doherty, D. A. Hughes, F. J. Humphreys, J. J. Jonas, D. Juul Jensen, M. E. Kassner, W. E. King, T. R. McNelley, H. J. McQueen, and A. D. Rollett: *Mat. Sci. Eng. A-Struct.*, 1997, vol. 238(2), pp. 219–274.

[8] K. Kashihara, M. Tagami, T. Okada, and F. Inoko: *Mat. Sci. Eng. A-Struct.*, 2000, vol. 291(1-2), pp. 207–217.

[9] T. J. Sabin, G. Winther, and D. Juul Jensen: *Acta Mater.*, 2003, vol. 51(14), pp. 3999–4011.

[10] G. L. Wu and D. Juul Jensen: *Acta Mater.*, 2007, vol. 55(15), pp. 4955–4964.

[11] H. Paul and J. Driver: *Microchim. Acta*, 2006, vol. 155(1-2), pp. 235–242.

[12] J. H. Driver, H. Paul, Glez J.-C., and Maurice C: *Proc. 21st Risø Symp.*, Roskilde, DK, pp. 35–48, 2000.

[13] S.R. Skjervold and N. Ryum: *Acta Mater.*, 1996, vol. 44, pp. 3407–3419.

[14] M. Upmanyu, D. J. Srolovitz, A. E. Lobkovsky, J. A. Warren, and W. C. Carter: *Acta Mater.*, 2006, vol. 54(7), pp. 1707–1719.

[15] B. Chalmers, editor: *Progress in Metal Physics*. Pergamon Press, Oxford, U.K., 1950, p. 170.

[16] X. Huang and G. Winther: *Phil. Mag.*, 2007, vol. 87(33), pp. 5189–5214.

[17] G. Winther and X. Huang: *Phil. Mag.*, 2007, vol. 87(33), pp. 5215–5235.

[18] G. Gottstein and L.S. Shvindlerman: *Grain Boundary Migration in Metals: Thermodynamics, Kinetics, Applications*. CRC Press, Boca Raton, FL, 1999.

[19] O. V. Mishin, B. Bay, and D. Juul Jensen: *Met. Trans. A*, 2000, vol. 31(6), pp.1653–1662.

[20] R. A. Vandermeer and P. Gordon: *Trans. AIME.*, 1959, vol. 215(4), pp. 577–588.

[21] Q. Liu, D. Juul Jensen, and N. Hansen: *Acta Mater.*, 1998, vol. 46(16), pp. 5819–5838.

[22] D. J. Dingley and V. Randle: *J. Mat. Sci.*, 1992, vol. 27(17), pp. 4545–4566.

[23] C.Y.J. Barlow, B. Bay, and N. Hansen: *Phil. Mag. A*, 1985, vol. 51:253–275.

[24] V. Randle, N. Hansen, and D. Juul Jensen: *Phil. Mag. A*, 1996, vol. 73:265–282.

Tables

Table I. Possible misorientation axes between nuclei of new orientations and the orientation at the point in the deformed matrix with the best fit. All axes with a deviation of less than 10° are listed.

Nucleus	Misorientation axis to deformed state	Misorientation angle	Orientation in deformed state (φ_1 Φ φ_2)	Nucleation site
B01	[1 1 -1]	36°	27° 111° 329°	Grain interior
B02	[1 2 -1] [1 1 -1]	44° 46°	26° 113° 327° 30° 113° 335°	Grain interior
C05	[1 -1 2] [1 -1 1] [1 -1 0]	31° 29° 45°	334° 85° 25° 330° 87° 18° 30° 106° 328°	Grain boundary
C06	[1 1 -1] [1 2 -1] [1 1 -2]	43° 44° 46°	335° 93° 33° 337° 77° 33° 330° 91° 23°	Grain boundary
C07	[1 -1 1] [2 -1 1]	50° 46°	30° 102° 340° 31° 105° 331°	Grain interior
D02	[1 0 0] [-2 1 1] [-1 1 1]	23° 41° 44°	28° 74° 21° 11° 89° 7° 335° 60° 345°	Triple junction
D06	[-1 0 1] [1 1 2] [1 -1 1]	20° 52° 47°	320° 46° 4° 16° 93° 13° 9° 108° 353°	Triple junction
D07	[0 1 0] [1 1 -2] [-1 0 1] [1 1 -1]	27° 34° 55° 27°	22° 83° 18° 13° 105° 353° 317° 48° 3° 13° 104° 4°	Triple junction

Table II. GNB planes as predicted from the expected slip systems for parent grains where agreement was found between the GNB plane normal and the rotation axis of nucleation. Only in one case agreement was found with the deviation axis, and for clarity the deviation axis is only listed in this case. Note that in all cases the agreement also includes the symmetric variant of the axes and planes. The nuclei marked with asterisks in sample C and D are first order twin related to each other. A "-" is used to show that no agreement could be found.

Nucleus	Misorientation axis and angle to deformed state (from Table 1)	Prediction from Schmid factors	Prediction from the Taylor model
B01	[1 1 -1] / 36°	GNBs aligned with **(11-1)** and (1-11)	-
B02	[1 1 -1] / 46° [1 2 -1] / 44°	GNBs aligned with **(11-1)**; Deviation axis: **[1 2 -1]**	-
C05*	-	-	-
C06*	[1 1 -1] / 43°	GNBs aligned with **(11-1)**	GNBs aligned with **(11-1)** and (1-11)
C07	[1 -1 1] / 50°	GNBs aligned with **(1-11)**	GNBs aligned with **(1-11)** and (11-1)
D02	[-1 1 1] / 44°	GNBs aligned with **(-111)**	GNBs aligned with **(-111)** and (131)
D06*	[1 -1 1] / 47°	GNBs aligned with **(1-11)** and (-111)	GNBs aligned with **(1-11)** and (-111)
D07*	-	-	-

Figures

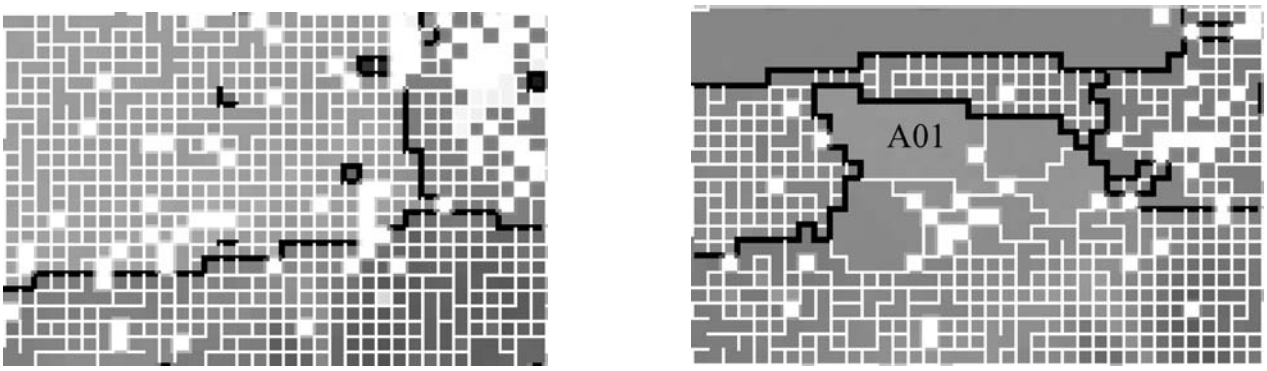

a) b)

Figure 1:
EBSP maps of a triple junction in sample A; a) before annealing and b) after annealing. White lines correspond to misorientations >1° but <10° and black lines correspond to misorientations >10°. White pixels are badly indexed points, which have been disregarded. The pixel size is 10 µm. A nucleus (A01) has grown by SIBM with an orientation similar to that of the grain in the lower part of the image. Another nucleus has appeared in the upper part of the image but extends outside the area examined, so the origin of this nucleus is unknown.

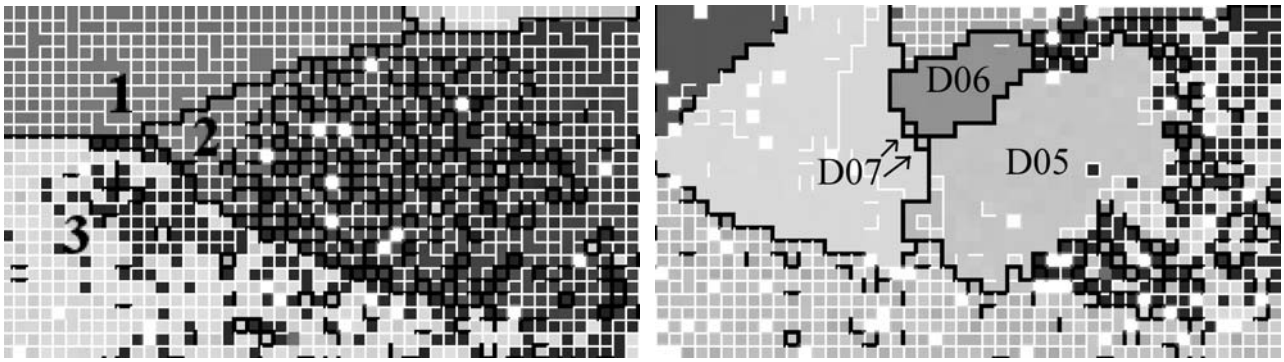

a) b)

Figure 2:
EBSP maps of a triple junction in sample D; a) before annealing and b) after annealing. White lines correspond to misorientations >1° and black lines correspond to misorientations >10°. White pixels are badly indexed points, which have been disregarded. The pixel size is 10 µm. Several nuclei have grown. Only the nuclei marked D05, D06 and D07 are considered, as the others extend outside the examined area and could therefore originate from elsewhere.

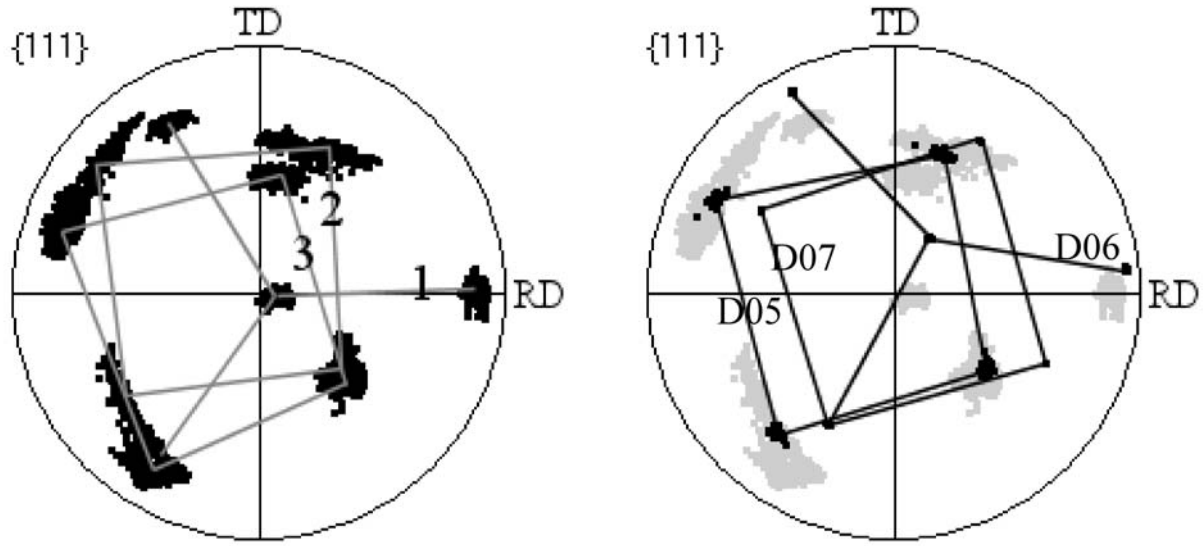

a) b)

Figure 3:

a): The orientations present at the triple junction in figure 2 before annealing. The area of the EBSP map that has been included in the pole figure corresponds to the area of the nuclei seen after annealing plus a rim of about 20 µm. The poles of the three grains are marked with connecting lines. The numbers correspond to the grains marked in figure 2 a).

b): The orientations of three nuclei overlaid on the orientations from a). One nucleus D05 has a parent orientation and a relatively large internal mosaicity. There is an internal twin relationship between D06 and D07.

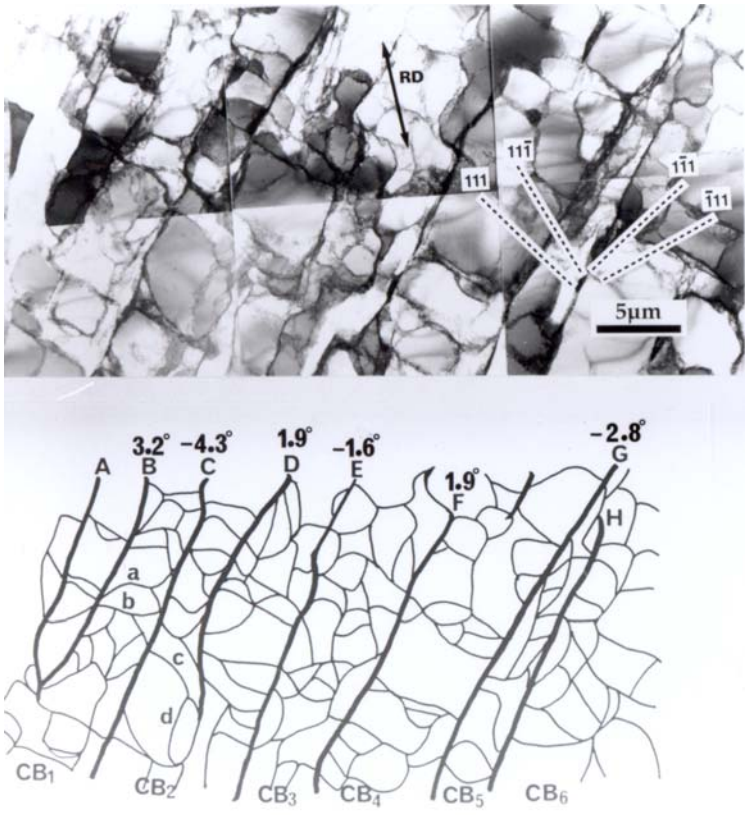

Figure 4:
Transmission electron micrograph of a typical deformation-induced dislocation structure in aluminium deformed to low strains (10%). The dislocations assemble in extended planar boundaries (GNBs) as well as cell boundaries. In the sketch below, the GNBs are marked A-H. From [21].

A5 Direct non-destructive observation of bulk nucleation in 30% deformed aluminum

S.S. West, S. Schmidt, H.O. Sørensen, G. Winther, H. F. Poulsen, L. Margulies, C. Gundlach and D. Juul Jensen, submitted to Scripta Materialia (2009).

Direct non-destructive observation of bulk nucleation in 30% deformed aluminum

S. S. West[1], S. Schmidt[1], H. O. Sørensen[1], G. Winther[1], H. F. Poulsen[1], L. Margulies[1], C. Gundlach[2] and D. Juul Jensen[1]

1: Center for Fundamental Research: Metal Structures in Four Dimensions, Risø DTU, Building 228, Frederiksborgvej 399, DK-4000 Roskilde, Denmark
2: Euroean Synchrotron Radiation Facility, 6 Rue Jules Horowitz, BP 220, F-38043 Grenoble, France

Abstract

A 30% deformed aluminum sample was mapped non-destructively using Three-Dimensional X-ray Diffraction (3DXRD) before and after annealing to nucleation of recrystallization. Nuclei appeared in the bulk of the sample. Their positions and volumes were determined, and the crystallographic orientations were compared with the orientations of the deformed grains. It was found that nuclei with new orientations can form and their orientations have been related to the dislocation structure in the deformed grains.

Keywords: nucleation of recrystallization, X-ray diffraction (XRD), 3D reconstruction.

During recrystallization of deformed metals, new almost dislocation free nuclei form and grow in the deformed microstructure. Whereas many experiments have focused on characterization of growth during recrystallization (see e.g. [1]) far less is known about the nucleation due to experimental limitations. Nucleation is a local process which is likely to take place at some sites in the deformed microstructure with a somewhat higher stored energy than the surrounding material. Well known sites of nucleation are triple junctions [2], grain boundaries [3] and large second phase particles [4]. But even in these cases it is not all the triple junctions, grain boundaries or second phase particles at which nuclei are formed. Post mortem studies of partly annealed samples (e.g. [5, 6]) cannot give information about why for example nucleation occurred at one particular triple junction and not at another. From the post mortem studies it is unknown what was there at the nucleation sites before the nuclei formed. This has been referred to as the problem of “lost evidence” [7]. In-situ surface studies of nucleation are possible and have been done [8, 9]. However, here the problem is that the observed nuclei may not all form at the observed surface but may originate from elements in the deformed microstructure below the surface which were not characterized.

There is thus a need for in-situ 3D investigations of nucleation. The so-called 3-dimensional X-ray diffraction (3DXRD) method offers this possibility [10, 11]. To our knowledge only one successful in-situ study of nucleation of recrystallization in the bulk has been reported in literature [12]. In that study, three nuclei were identified, where two of them were twin related to the deformed grain in which they formed and one had an orientation which was neither present in the deformed parent grains nor first order twin related to any of them. The aim of the present work is to use 3DXRD to study nucleation and to take advantage of the improvements of the 3DXRD methods which have been realized since that study was performed.

A sample was prepared from 30% cold rolled 99.996% pure aluminum which initially had an average grain size of 500 μm and almost straight grain boundaries. In a sample of this type, nucleation is expected to occur mainly at triple junctions and grain boundaries [2, 9]. The sample cross section was 1000 μm × 600 μm, where the largest faces were mechanically polished and the smaller faces were spark cut. The whole sample was finally electrochemically polished. The furnace for annealing was mounted directly in the X-ray beam at the beamline ID11 at the ESRF synchrotron facility. The furnace was placed on an ω-rotation stage with the rotation axis perpendicular to the beam. The diffracted X-rays were collected on a Frelon 2k×2k CCD camera with a pixel size of 50 μm, placed 17 cm from the sample.

The X-ray beam was focused vertically to a FWHM height of 7 μm and slit horizontally to a width of 1500 μm. This means that the beam was wide enough to illuminate the entire cross section of the sample at any ω-rotation angle.

A total gauge volume of 1000×600×700 μm^3 was mapped layer by layer. Each layer was probed by taking 360 images, rotating the sample in two separate ω ranges of [-22.5°; 22.5°] and [67.5°; 112.5°] in 0.25° steps. This ensured that a sufficient number of diffraction spots were recorded to make an accurate determination of crystallographic orientations and positions. Before annealing the deformed sample was mapped in 97 consecutive layers 7 μm apart in the *z*-direction. Then the sample was annealed for 2 minutes at 320° C initiating nucleation. After the annealing, the same gauge volume was mapped again to enable a direct comparison of the microstructure before and after nucleation of recrystallization. Each map required data collection for ~54 hours. In the present experiment, the setup allowed detection of all volume elements larger than 1 μm in equivalent spherical diameter.

Figure 1 shows examples of the recorded CCD images in the deformed and annealed conditions. The diffraction spots from the deformed sample are broad and widely spread both in η and ω (see figure 1 a). These broad spots are also seen together with some sharp (limited in size to the point spread function of the detector) spots from the annealed sample (see figure 1 b). The sharp spots are from the nuclei.

If nuclei develop with orientations similar to the deformed grains, the sharp nuclei spots will “drown” in the broad spots from the deformed grains and thus not be recorded. Nuclei with new orientations will, however, show up by clear sharp spots away from the broad spots. This means that the experiment is ideal for detecting any nuclei which may develop with new orientations whereas nuclei with parent orientations, e.g. formed by SIBM [3] will not be recorded.

From the diffraction spots of the nuclei, their orientations and positions can be found [13]. 50 nuclei of new orientations were observed, but most of them were situated at the surfaces. These were discarded in the present analysis as they could originate from e.g. surface scratches, and the focus of this study was bulk nucleation. All nuclei within 30 μm of the surfaces or extending outside the gauge volume were thus removed from the data set, leaving 6 nuclei of new orientations. As the entire volume around the nucleation sites was mapped before and after annealing, these orientations can definitively be said to be new.

The volumes of the nuclei were found from the intensities of the diffraction spots in four diffraction rings [14] using the reference intensity of a gold foil of random texture [15]. As the beam was focused narrowly in the *z* direction, the volume found in this way corresponds to the volume of the

7 μm slice of a given grain which is illuminated by the beam during the imaging. Figure 2 shows a map of the volumes of the six nuclei that were found in the bulk. It is seen that some of the nuclei have grown quite large during the annealing, while others are still small. Two of the nuclei were seen only in one layer.

While the 3DXRD microscope has previously been used for three dimensional mapping of undeformed structures on several occasions (e.g. [16]), mapping of deformed materials has so far only been shown feasible with simulated data [17]. However, the software presented in [16] has now been developed to a point where also moderately deformed samples may be mapped with a good accuracy. The *x*,*y*,*z* positions of all the nuclei can thus be correlated to the deformed microstructure.

The 3DXRD maps were supplemented by EBSP surface scans. The maps and scans show that about 10 deformed grains were present in the gauge volume mapped.

Figure 3 shows two maps from different layers before and after annealing. The orientations and boundary positions mapped by 3DXRD show an excellent match with the values at the surfaces obtained by EBSP, both before and after annealing. Only selected layers are reconstructed in the present study, as these were deemed sufficient for the analysis required. In the deformed sample, layer 45, which is close to the middle of the gauge volume, was selected for reconstruction. This layer contains the three deformed grains, marked A, C and D, considered to be possible parents to the nuclei of new orientations because of their vicinity to the nuclei positions. Layer 17, which was chosen for the reconstruction after annealing contains diffraction spots from three of the six nuclei of interest and also contains deformed grains A and C. One of these nuclei has already grown quite large and is centered in another layer. The other two nuclei are however quite small, one is present only in this layer, while the other is present in three layers with this being the middle one.

Although diffraction spots from grain "D" were present in layer 17 before annealing, the grain was very small in this layer and had been at least partially consumed by both surface and bulk nuclei in the annealing process. As a result, grain "D" was not observed in the 3DXRD map of layer 17 after annealing.

The orientations of the 6 nuclei were determined not to have a twin relationship to any of the deformed grains or neighboring surface nuclei. Following the procedure applied in previous studies of nucleation as observed on the sample surface by EBSP [8, 18] the orientation relationship between nuclei and the three possible parent grains was investigated in more detail. In those studies nuclei were found to be rotated away from the parent grain around a <111> axis corresponding to the normal of the extended planar dislocation boundaries expected to be induced by the deformation. Neither the EBSP nor the 3DXRD maps of the present study have sufficient resolution to reveal the dislocation boundaries. By analogy with the previous studies, established relations [19, 20] between slip systems and dislocation boundary planes were therefore used to predict the boundary planes based on the expected slip systems.

The result of the dislocation boundary prediction is presented in Table 1. The orientation difference between grains A and C is relatively small and for both grains the Taylor model as well as a Schmid factor analysis leads to prediction of active slip systems on only two slip planes, namely (111) and (1-11), which according to [19,20] gives rise to boundaries aligned with these two slip planes. For grain D both the Taylor model and the Schmid factors predict activity on 8 slip systems on all 4

{111} planes. The high number of active systems as well as the existence of 4 equivalent Taylor solutions make it difficult to predict the GNB planes in this grain as there are several possibilities. However, three systems consistently show up in the equivalent solutions to the Taylor model. Two of these have the same slip direction and should give rise to boundaries aligned with (010) while the third system would give a boundary aligned with (1-11). It could, however, not be ruled out that boundaries aligned with the three other {111} planes might also be present.

For rolling deformation it has been found that boundaries on {111} have a dominant twist character while other boundaries have more tilt character (Qing 1998). Consequently, the misorientation axis across the boundaries on a {111} plane is expected to lie close to the <111> slip plane normal while the axis for the boundaries on (010) are expected to be perpendicular to [010], as also stated in Table 1.

Note that orientations measured on the two surfaces with EBSP and the orientations obtained by 3DXRD were roughly the same, indicating that these orientations represent the entire grains well. Analysis of the orientation relations between nuclei and the deformed grains is based on the combined set of measured orientations.

The misorientation axes between the ensemble of orientations for grains A, C, and D and the 6 nuclei were calculated. For grains A and C none of the axes were within 10° of the axes associated with the dislocation boundaries in Table 1. For grain D, 4 of the 6 nuclei were rotated from an orientation present in the deformed state around an axis within 1° of [100], which is perpendicular to the expected [010] boundary plane normal and a potential misorientation axis of a tilt boundary on this plane. In addition [-101], which is also perpendicular to [010], was identified as a possible rotation axis for 3 of these nuclei with an axis within 2°-4°. For the two remaining nuclei (2 and 3) two <111> axes were identified as possible rotation axes. As mentioned, dislocation boundaries on {111} planes as well as with <111> misorientation axes were also found possible from the slip system/boundary characteristics analysis and are listed in Table 1.

The analysis suggests that all nuclei originated from grain D. By analogy with the previous studies, possible correlations between the nucleation and the deformation induced dislocation boundaries were identified. The previous studies could not distinguish between the effect of the boundary plane and the misorientation axis across it as only <111> rotated nuclei related to {111} twist boundaries were found. The present finding of 4 nuclei rotated around a well-defined [100] axis, which is a possible misorientation axis of the expected (010) tilt boundary means that the effect must be attributed to the misorientation, although the exact mechanism remains unresolved.

In conclusion, this study has achieved the following:

- The 3DXRD setup was optimized to allow 1) 3D mapping of deformed microstructures at least up to 30% deformation and 2) direct in-situ observation of bulk nuclei of new orientations.
- In pure aluminum cold rolled 30%, 6 nuclei with new orientations were found within a gauge volume of 1000×600×700 μm^3, all near or at grain boundaries or triple junctions. These 6 nuclei all have orientations different from any orientations within volume elements larger than 1 µm in the deformed parent grains.
- Analysis of the orientation relations between the nuclei and the three potential parent grains shows that the nuclei most likely originate from one of the deformed grains and that the

rotation between the nuclei and the parent grain is related to the misorientation axis across deformation induced dislocation boundaries in this grain.

References:

[1] S.-J.L. Kang, M.Y. Huh, N.M. Hwang, H. Homma, K. Ushioda, Y. Ikuhara, (Eds.), Proc. ReX-GG III, Mater. Sci. Forum 558-559 (2007).
[2] R. A. Vandermeer, P. Gordon, AIME Transactions 215(4) (1959) 577.
[3] P.A. Beck, P.R. Sperry, J. Appl. Phys. 21(2) (1950) 150.
[4] F. J. Humphreys, Proc. 1st Risø Symp. (1980) 35.
[5] S.R. Skjervold, N. Ryum, Acta Mater. 44 (1996) 3407.
[6] J. H. Driver, H. Paul, Glez J.-C., Maurice C., Proc. 21st Risø Symp. (2000) 35.
[7] B. Duggan. Term suggested at international conference on textures of materials, ICOTOM 11 (1996).
[8] T. J. Sabin, G. Winther, D. Juul Jensen, Acta Mater. 51(14) (2003) 3999.
[9] S. S. West, S. Schmidt, D. Juul Jensen, Proc. 29th Risø Symp. (2008) 383.
[10] H. F. Poulsen, S. Garbe, T. Lorentzen, D. Juul Jensen, F. W. Poulsen, N. H. Andersen, T. Frello, R. Feidenhansl, H. Graafsma, J. Synch. Rad. 4 (1997) 147.
[11] H.F. Poulsen, Three-Dimensional X-Ray Diffraction Microscopy: Mapping Polycrystals and their Dynamics. Springer, New York, 2004.
[12] A. W. Larsen, H. F. Poulsen, L. Margulies, C. Gundlach, Q. F. Xing, X. X. Huang, D. Juul Jensen, Scripta Mater. 53(5) (2005) 553.
[13] S. Schmidt. http://fable.wiki.sourceforge.net/grainspotter, 2009.
[14] H. O. Sørensen. http://fable.wiki.sourceforge.net/fabric, 2009.
[15] E. M. Lauridsen, D. Juul Jensen, H. F. Poulsen, U. Lienert. Scripta Mater. 43(6) (2000) 561.
[16] S. Schmidt, U.L. Olsen, H.F. Poulsen, H.O. Sørensen, E.M. Lauridsen, L. Margulies, C. Maurice, D. Juul Jensen, Scripta Mater. 59 (2008) 491.
[17] L. Rodek, H. F. Poulsen, E. Knudsen, G. T. Herman, J. Appl. Cryst. 40(2) (2007) 313.
[18] S.S. West, G. Winther, D Juul Jensen, Submitted 2009.
[19] X. Huang, G. Winther, Phil. Mag., 87(33) (2007) 5189.
[20] G. Winther, X. Huang, Phil. Mag. 87(33) (2007) 5215.

Table 1:The three deformed grains considered to be possible parents to the nuclei. The planes on which GNBs are likely to form are listed along with the possible axes of misorientation associated with them.

Grain	(φ_1,Φ,φ_2)	GNB planes	Possible rotation axes
A	(193,35,88)	(111), (1-11)	[111], [1-11]
C	(174,24,84)	(111), (1-11)	[111], [1-11]
D	(65,41,23)	(111), (11-1), (1-11), (-111), (010)	[111], [11-1],[1-11],[11-1], Axes $\perp$ [010]

Table 2: The 6 nuclei with new orientations found in the bulk. L_z and L_{xy} are the length in *z* and the equivalent diameter in the *xy* plane respectively. The misorientation axes and angles are to the point in grain "D" with the best fit of the rotation axis.

Nucleus	(φ_1,Φ,φ_2)	Layers (L_z)	L_{xy}	Mis. axes	Mis. angle
1	(42,18,50)	16-18 (21µm)	13 µm	[100], [-101]	31°, 36°
2	(80,45,18)	20-30 (77µm)	56 µm	[111]	18°
3	(44,40,44)	17 (≥7µm)	6 µm	[11-1]	16°
4	(48,24,42)	19-20 (14µm)	10 µm	[100], [-101]	20°, 20°
5	(50,27,37)	22-30 (63µm)	41 µm	[100], [-101]	8°, 11°
6	(18,17,62)	31 (≥7µm)	7 µm	[100]	29°

Figures

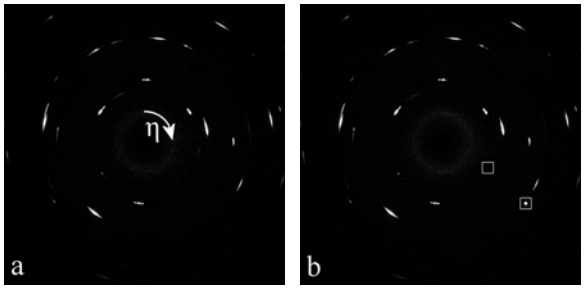

Figure 1: CCD images before and after annealing. Diffraction spots from two nuclei (one very small and one large) are marked with squares

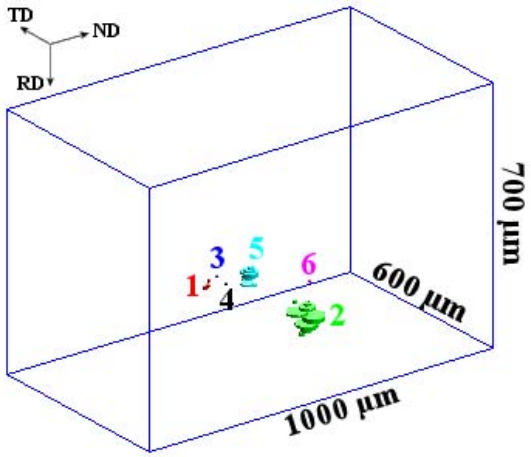

Figure 2: The 6 bulk nuclei with new orientations plotted as a disk of equivalent volume in each layer of the mapping. This does therefore not directly show the exact shapes of the nuclei but represents their volumes and positions in *x,y,z*.

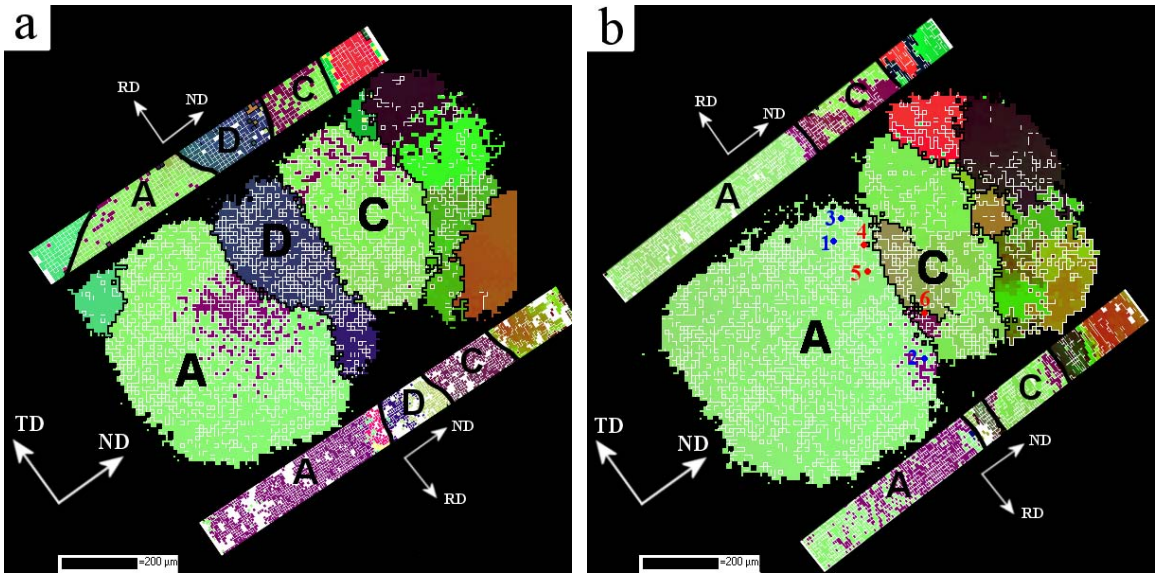

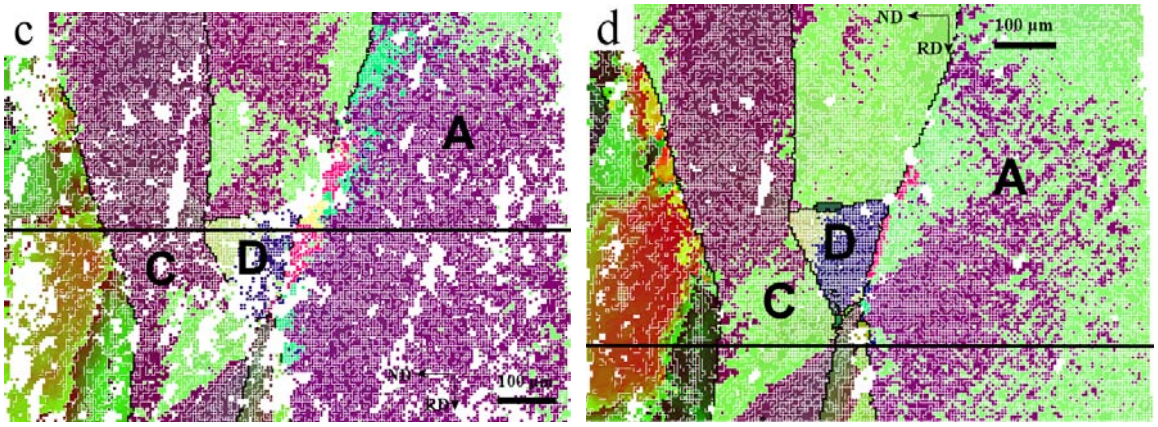

Figure 3:
a,b: Map of the microstructure in layer 45 before (a) and layer 17 after (b) annealing from 3DXRD diffraction data. Areas of EBSP maps from the two surfaces have been placed on each side for comparison. The positions of the 6 bulk nuclei have been marked by numbers in the map after annealing; nuclei 1, 2 and 3 are marked in blue because they are present in this layer, .
c,d: EBSP maps of one surface of the gauge volume before and after annealing. The locations of the 3DXRD maps in a) and b) are marked by lines.

Risø DTU is the National Laboratory for Sustainable Energy. Our research focuses on development of energy technologies and systems with minimal effect on climate, and contributes to innovation, education and policy. Risø has large experimental facilities and interdisciplinary research environments, and includes the national centre for nuclear technologies.

Risø DTU
National Laboratory for Sustainable Energy
Technical University of Denmark

Frederiksborgvej 399
PO Box 49
DK-4000 Roskilde
Denmark
Phone +45 4677 4677
Fax +45 4677 5688

www.risoe.dtu.dk